Electrical preparation of spin-polarized electrons in semiconductor quantum dots

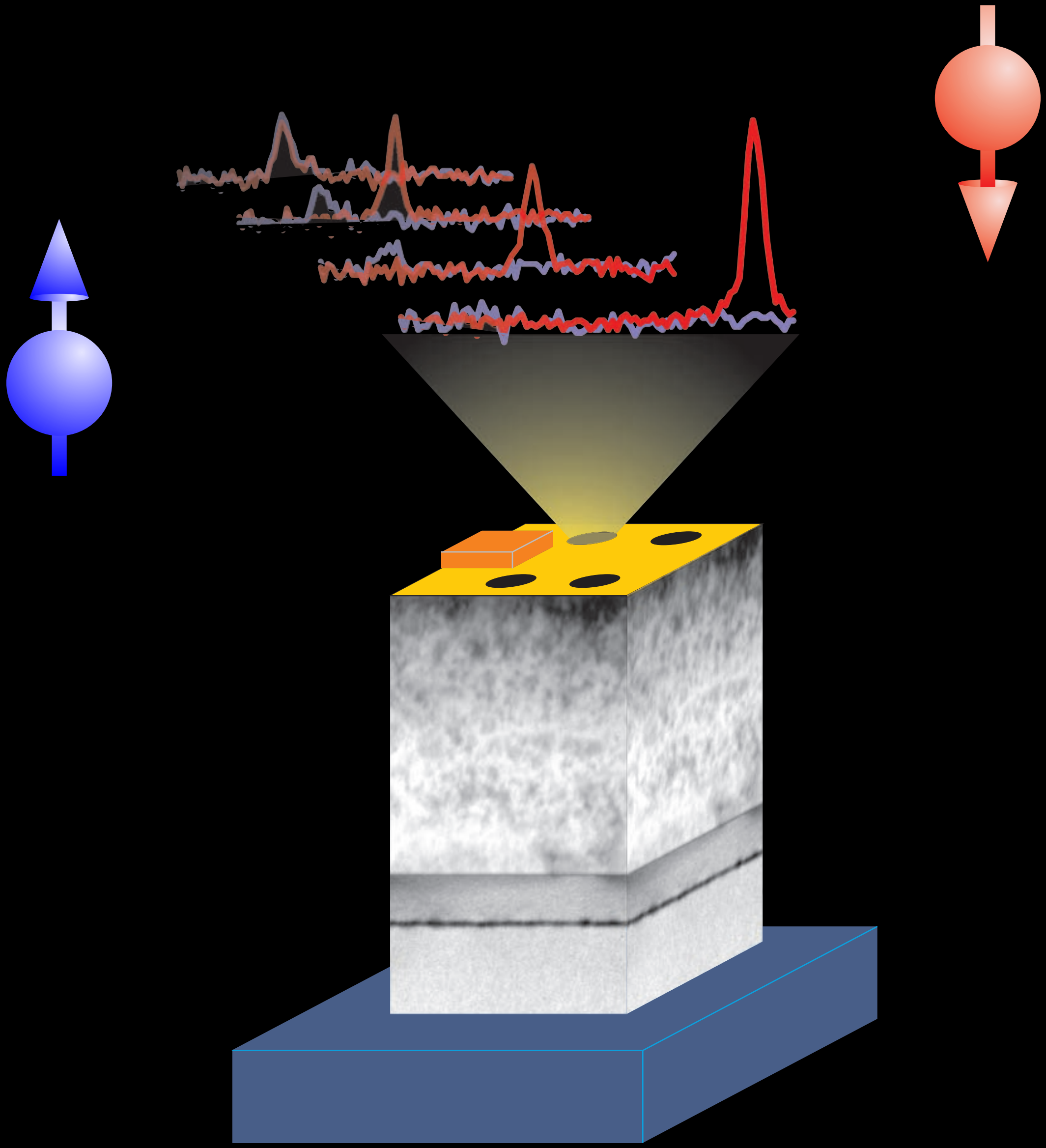

Wolfgang Löffler

Institut für
Angewandte Physik

Universität Karlsruhe (TH)
Forschungsuniversität • gegründet 1825

2008

Electrical preparation of spin-polarized electrons in semiconductor quantum dots

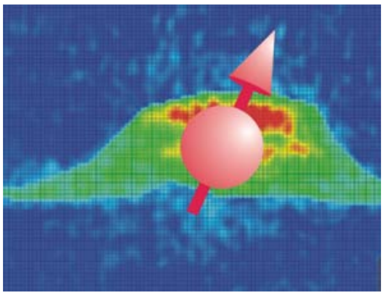

Zur Erlangung des akademischen Grades eines
DOKTORS DER NATURWISSENSCHAFTEN
von der Fakultät für Physik
der Universität Karlsruhe (TH)

genehmigte

DISSERTATION

von

Dipl.-Phys. Wolfgang Löffler
aus Ludwigshafen am Rhein

Tag der mündlichen Prüfung : 08.02.2008
Referent : Prof. Dr. H. Kalt
Korreferent : Prof. Dr. C. F. Klingshirn

Prüfungskommission:

Prof. Dr. K. Busch
Prof. Dr. H. Kalt
Prof. Dr. C. Klingshirn
Prof. Dr. J. Blümer
Prof. Dr. G. Schön
Prof. Dr. W. Wulfhekel

Cover image: Scheme of the spin-injection light-emitting diode and emission spectrum. TEM image by D. Litvinov.

Title image: High-resolution transmission electron micrograph with chemical analysis (CELFA) of a single InAs quantum dot by D. Litvinov.

Universität Karlsruhe
Institut für Angewandte Physik
Wolfgang-Gaede-Str. 1
D-76131 Karlsruhe

http://www.aph.uni-karlsruhe.de
wolfgang.loeffler@physik.uni-karlsruhe.de

This work was supported by the DFG Research Center for Functional Nanostructures (CFN) at the Universität Karlsruhe (project A2).

CFN DFG
Universität Karlsruhe (TH)
Forschungsuniversität • gegründet 1825
KIT
Karlsruhe Institute of Technology

Contents

Chapter 1

Motivation and background

In state-of-the-art integrated circuits and storage units (flash memory, dynamic random-access memory) quantum mechanical effects mark the physical limit for further size reduction: Be it tunneling of electrons through the oxide layer in metal-oxide-semiconductor field-effect transistors or unloading of storage cells in flash memory. MOSFET industry is therefore looking for new insulating materials with a higher permittivity κ while preserving the high capacitance of the transistor. For next-generation transistors like the fin-FET, feature size gets so small that quantum tunneling sets the ultimate limit for further miniaturization. Since Nov, 2007 45 nm processes with hafnium-based dielectrics are used in mass production [1].

On the other hand, the possibility to fabricate nanostructures where the characteristic size is near the de Broglie wavelength of electrons opens up a new dimension: The structures can be tailored to show specific quantum mechanical effects. A prominent example is the self-assembled quantum dot, a 5 to 100 nm in diameter, and more or less lens-shaped inclusion of a semiconductor single crystal in a host material of wider band gap. The electron wavelength being for example about 160 nm in $\mathrm{In}_{0.6}\mathrm{Ga}_{0.4}\mathrm{As}$ (at 5 K), size quantization happens and discrete energy levels form, similar to the atomic ones. An electron localized in such a dot is then completely isolated from the environment and shows free (quantum-mechanical) evolution in time.

The idea to use well-understood and well-isolated quantum-mechanical systems for information processing (qubits) exists since the 1980s [1]. These systems being available now the completely new field of quantum information processing with semiconductor nanostructures is unclosed. Lloyd demonstrated [2] that a quantum computer could simulate nearly all quantum-mechanical systems. With only 50-100 interconnected qubits useful quantum simulation can be performed being impossible

---

[1] See the international roadmap for semiconductors, `http://www.itrs.net`

with classical systems! [2]

The idea and its realization

The driving idea is simple: A quantum-mechanical two-level system with the basis states $|0\rangle$ and $|1\rangle$ can take any state in the Hilbert space spanned by the two basis vectors. If this system is now prepared in a superposition of the two basis states and we apply an (unitary) operator to it, the result does contain information about both basis states. This evolution of superposition is the strength unique to quantum information processing. In contrast to classical computation where the information unit, the bit, can be read and copied at any time, quantum mechanics forbids such things: There is the no-cloning theorem (which was found out surprisingly late [3]) and spying at the qubit destroys its coherences. The latter has to be taken very seriously: A single microwave photon can destroy the coherences of a ^{85}Rb atom passing a double slit [4]!

This should emphasize that we need a system that is isolated from the environment. Vacuum is a possibility (ion traps, atom traps, optical lattices are implementations therein) but we do only need to isolate the specific degree of freedom, which accounts for the qubit: In our case, the electron spin. An electron stored in a InAs/GaAs quantum dot can be considered as such a system: The coherence times are long enough, a lower bound is the order of microseconds[3]. This is impressive as the electron is spread out over $10^3 \dots 10^4$ atoms and each of them carries a spin larger than the electron's spin (see Chap. 3).

Semiconductor materials are not only advantageous because of the well-controlled fabrication techniques: The special band structure makes coupling to the light field possible via interband transitions. Thereby also spin information can be transported (coherently) and coupling of distant qubits may be possible [7].

Self-assembled quantum dots. Self-assembled quantum dots are often mistaken with electrostatic quantum dots: In the latter, a two-dimensional electron gas is additionally confined in the two remaining dimensions by application of electrical gates. In these systems, electron-hole transitions are impossible and the confinement is much weaker. Nevertheless, both fields are closely related and can benefit from

---

[2] Factorization of prime numbers requires around 500 qubits to outperform classical computers.

[3] The needed time depends on the time it takes to conduct operations with them. Latest estimations for single operations lie within the range of picoseconds up to nanoseconds. See Greilich et al. [5] for coherence and Kroutvar et al. [6] for relaxation.

each other.

In a scheme for realistic quantum computation, the two-level system (qubit) must be prepared in its initial state first. Using single-qubit operations, every desired state can be prepared subsequently. The computation is then done via single-qubit and multi-qubit operations. Finally, the state is read-out (which destroys the coherences). All these steps look very promising for semiconductor quantum dots: Initialization is possible by electrical methods (this work) as well as optically, single-qubit operations are realized, multi-qubit gate operations are possible in theory and subject to active research. Read- ut could be done by triggering optical transitions in the dot (like in this work) or by other methods with single-dot resolution.

Other group's achievements in that field

The idea to investigate what happens if electrons are injected from a spin-polarized source (in this case a ferromagnet) into a semiconductor came up by Aronov and Pikus [8] in 1976. The realization had to wait until proper semiconductor technologies became standard: Oestreich et al. [9] demonstrated spin injection of excitons from a diluted magnetic semiconductor into bulk material in 1999. Shortly afterwards, Fiederling et al. [10] and Ohno et al. [11] demonstrated the same in a p-i-n diode structure. These experiments were targeted more to the spintronic direction where the ultimate goal is a spin field effect transistor [12] and not spin-state preparation with near-unity fidelity for quantum information processing, like here.

The next step, the injection into quantum dots was demostrated in 2002 by Gosh et al. [13] and Chye et al. [14]. They used a ferromagnetic GaMnAs spin-aligner with relatively modest spin injection efficiency. The first injection into a single self-assembled quantum dot was shown in 2004 via optical injection by Seufert et al. [15]. To the best of our knowledge, we were the first to show preparation of spin states (five in parallel) with near-unity fidelity [16] in an electrical device.

Optical methods. Using all-optical methods, the creation (or polarization) of a single spin-polarized electron is not straightforward: Resonant interband excitation leads to the generation of an electron-hole pair that is subject to fast decoherence. To prepare a single spin-polarized electron by optical means the dot must be δ-doped with exactly one single electron. Using a narrow-line laser the unwanted spin-state is depleted via trion excitation (Atatüre et al. [17]).

Electrical spin-state preparation

The all-electrical preparation of spin states has huge advantages: It is easy to combine with current semiconductor technology and the need for laser systems is reduced. However, the spin cannot be controlled directly, the use of magnetic fields is needed. We show this via a two-stage process: The polarization of the electron spin and the subsequent injection into a single quantum dot are separated. Thereby we do also avoid disturbance of the spin in the quantum dot. That is possible in a p-i-n light-emitting diode structure[4] where the electrons first pass the spin-aligner material before injection into the dots.

In such a device we have achieved near-unity spin polarization of a single electron in an InAs/GaAs quantum dot using the semi-magnetic spin-aligner ZnMnSe. The process is very reliable and we went a little further, we demonstrate in this work the preparation of spin-polarized electrons in several InAs/GaAs quantum dots in parallel. The electrons are polarized in a common ZnMnSe layer and stored in InAs/GaAs quantum dots. Synchronous preparation of highly spin-polarized electrons was not possible before.

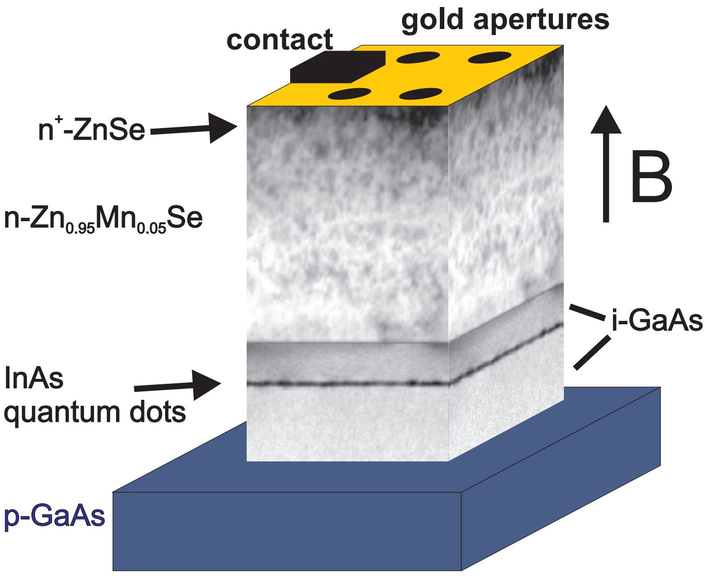

---

[4] We use the term spin-LED throughout in this work.

Outline

In the Chap. 2 we outline the various possibilities to polarize electron spins. An extensive investigation of the spin dynamics in the spin-aligner ZnMnSe follows. Several issues that we think prevented good operation of the devices of other groups are presented. We present an analytic solution to the electron spin-polarization in ZnMnSe, which is in good agreement with experimental data.

A central point in our work is the storage of spin-polarized electrons in InAs quantum dots. In Chap. 3, we first try to learn about the electronic states in these quantum dots. Careful modeling of the fabricated dots for numerical $\boldsymbol{k} \cdot \boldsymbol{p}$ calculations is needed to get good correspondence of theory and experiment. We then can evidence that the electronic structure in the dot is well understood by comparison with experimental data. In the section "advanced topics on quantum dot properties" we will discuss further relevant topics about electrons in quantum dots (optical selection rules, many-carrier effects and spin relaxation and decoherence) and present a short overview of the implementation of a qubit with the electron spin. Chapters 2 and 3 contain experimental results which are partially obtained using the complete device, the spin-LED.

After discussing these building blocks and its implications we address the entire device in Chap. 4. We study the interplay of doping, quantum-dot morphology and (quasi-) Fermi levels in the device. In addition, the relevant mechanisms for electron transport and their energetic relaxation are investigated. After optimization we finally demonstrate the high-fidelity preparation of a single spin-polarized electron in a single quantum dot, as well as the extension to the initialization of a quantum-dot micro-ensemble.

Chapter 2

Polarizing electron spins for injection into quantum dots

First, we summarize approaches to polarize the electron. We focus on mechanisms, which can be used in an electrical device, where the carriers (in our case electrons) are polarized. Our goal is to store the spin-polarized electrons in InAs quantum dots, which in turn are grown on GaAs; therefore, the spin aligner must be compatible with GaAs, too. An important point for epitaxial growth is that not only the crystal structures must match but also the lattice mismatch should be negligible.

The material of (our) choice is ZnMnSe, a diluted magnetic semiconductor (DMS) that is compatible with GaAs for epitaxial growth. We will investigate it in detail in the last section of this chapter.

We will not discuss a complementary approach to generate a spin population, which works optically: Absorption of a circularly polarized photon can lead to the generation of a fully spin-polarized electron-hole pair. This mechanism is called optical orientation [18]. In zincblende semiconductors, the degeneracy of the light- and heavy-hole band results in a maximum of 50% electron spin polarization. It is also impossible to optically excite a single electron without creating somewhere a (correlated) hole. Electron-hole exchange interaction could lead to additional spin relaxation and dephasing mechanisms. Therefore, we focus in this work on the polarization of single electrons without generation of holes.

As pointed out in the introduction, the spin cooling of a conduction-band electron is an alternative all-optical approach.

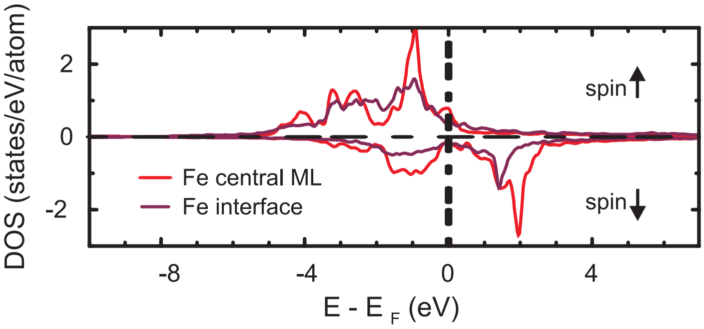

Figure 2.1: Spin-resolved density of states for Fe from [22]. The calculation results show the density of states of a monolayer (ML) inside of the bcc crystal (red) and of one at the surface. The latter counts also for very thin layers of Fe.

2.1 Spintronics: Polarizing electron spins

The rationale for this and for many experiments is the perspective for spin-based electronics (see e.g. [19, 20, 21]). The building block could be a spin field-effect transistor [12] where the resistivity is switched by rotating the spin between two spin polarizers instead of charge movement. If it is possible to do computation only with spin currents without involving charge currents, dissipation can be reduced.

Starting point is always the generation of spin-polarized electrons. We will present the most common techniques in the following.

2.1.1 Ferromagnetic metals

The most obvious approach is to take a ferromagnetic metal with a high Curie temperature. If the thickness is large enough spontaneous magnetization occurs and even without an applied external magnetic field, electrons can be polarized.

In Fig. 2.1 (red curve) the electronic density of states for electrons in [001] bcc Fe polarized parallel and anti-parallel to the magnetization are shown. Near the Fermi edge, states for both polarizations are available which lead to decreased electron spin polarization. The calculations have been made for monolayers of Fe, too. Such thin layers are more important for spintronic applications as always interfaces are involved. There we observe an even lower difference in the density of states than in the bulk case.

One expects spin-polarized current because the conductivity is different for spin-up and spin-down electrons in the ferromagnet, which results from the different density of states.

Nevertheless, Fe layers have been used successfully for spintronics and spin-injection

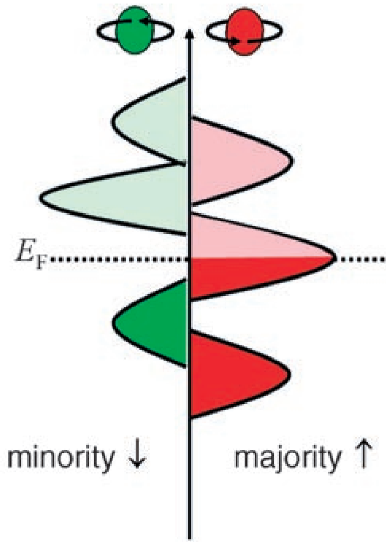

Figure 2.2: Density of states for both spin polarizations in a ferromagnetic half-metal. (From [29]) For the minority carriers, the material is semiconducting while for the majority carriers it is a metal.

devices [23, 24, 25]. None of them work in a straightforward structure, tunnel barriers have to be introduced to overcome the conductivity mismatch at the ferromagnet–semiconductor interface [26].

2.1.2 Ferromagnetic semiconductors

Another option is to use a ferromagnetic semiconductor like GaMnAs. In GaMnAs, manganese ions are not incorporated isoelectrically and lead to p-type doping. Below the Curie temperature T_C, spontaneous magnetization develops and holes get spin polarized. This has been shown successfully in a spin-injection LED by Y. Ohno et al. [11]. Spin polarization degree was rather low (1%) which can also be attributed to fast hole-spin relaxation in the InGaAs quantum well.

Most ferromagnetic semiconductors [27] show low Curie temperatures and not many are n-conducting. Recently, above-room temperature ferromagnetism has been observed in the n-conducting InMnAs [28], which could open up new possibilities.

2.1.3 Heusler alloys

Heusler investigated [30] materials of special crystallographic phases which show an interesting property: Sometimes new materials were obtained by combining nonmagnetic elements which exhibit strong ferromagnetism. The crystal structure

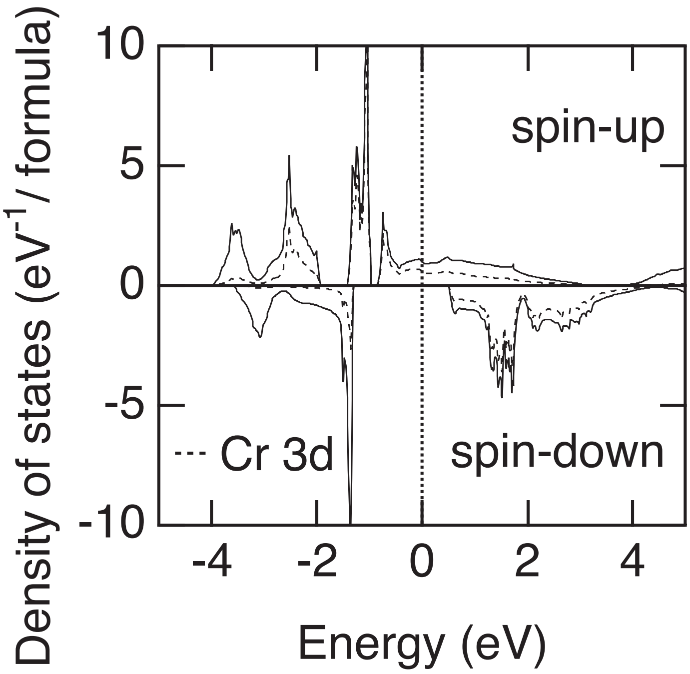

Figure 2.3: Density of states for both spin polarizations in the novel zincblende half-metal CrAs. (From [31]) Near the Fermi edge (dotted line), there are no states for spin-down carriers while there are for spin-up carriers. The first are in a semiconducting phase, the latter in metallic phase.

is complex: four fcc lattices are interleaved. The density of states is metallic for one spin polarization and semiconducting for the other. Therefore, these materials are also called half-metals. As shown in Fig. 2.2, the density of states (DOS) for minority carriers is equal to zero at the Fermi energy, this being the semiconducting part. The majority spin DOS there has metallic character.

There are plenty of materials with half-metallic character, which are topic of current research, especially for spintronic applications. For a review see Felser et al. [29].

A scheme of the DOS of a half-metallic Heusler alloy is shown in Fig. 2.2. We can see clearly the semiconducting character of spin-down electrons and the metallic character of spin-up electrons. Comparing a realistic DOS plot in Fig. 2.3, we can easily recognize the energy gap at the fermi energy for the minority spin phase. For this material, the Curie temperature is higher than 400 K. It can be deposited via molecular beam epitaxy on GaAs substrate, making it very promising for spintronic applications.

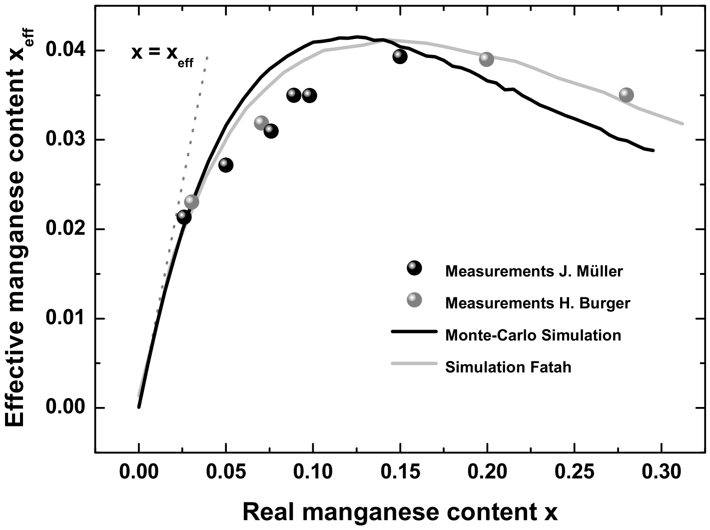

Figure 2.4: Effective manganese concentration. Only at very low Manganese content all manganese atoms contribute to the Zeeman splitting (ideal case shown by $x = x_{eff}$ line). At higher content, antiferromagnetic coupling compensates the magnetic moments. The simulation of Fatah et al. is taken from Ref. [34].

2.2 The diluted magnetic semiconductor $Zn_{1-x}Mn_xSe$

Diluted magnetic semiconductors [32] are semiconductor alloys where magnetic atoms replace some of the host atoms, mostly the cations. In case of ZnMnSe, some zinc atoms are replaced by manganese atoms (or Mn^{++} in the crystal). A particular feature of this material is that this replacement does not introduce doping in the semiconductor because manganese is isoelectric to zinc. Zinc has the electron configuration $[Ar]3d^{10}4s^2$ and manganese $[Ar]3d^5 4s^2$. According to Hund's rule, the spins of the five 3d electrons in manganese are aligned in parallel. Adding an additional electron to the $3d^5$ shell requires a huge amount of energy and therefore this half-filled shell has similar properties to the filled $3d^{10}$ shell of zinc.

Zinc has no resulting spin and all electrons are paired. In contrast, manganese has a large spin of 5/2, which results in the strong paramagnetic nature of the material. However, two manganese atoms at adjacent lattice positions will align their spin antiparallel due to dipole interaction. This antiferromagnetic coupling reduces the number of paramagnetic manganese atoms. This is allowed for by introducing the effective manganese concentration x_{eff}. A Monte-Carlo simulation[1] developed in the context of this work shows good correspondence with experiments done in Karlsruhe (see Fig. 2.4).

---

[1] Details are given in Ref. [33].

2.2.1 Polarization of manganese magnetic moments in a magnetic field

Instead of assuming that we can describe the averaged manganese spin with a modified Brillouin function (which in the end turned out to be right), we try to give here an exact derivation:

First, we neglect Mn–Mn interactions, which is justified only in the dilute limit ($x_{Mn} \lesssim 0.01$). In this case we can describe the magnetization M with a perfect Brillouin paramagnet:

$$\begin{aligned} M &= N\,\mu B_J \left(\frac{\mu\,B}{k_B T}\right) \\ &= -x\,N_0\,g_{Mn}\,\mu_B\,J\,B_J\left(\frac{g_{Mn}\,\mu_B\,J\,B}{k_B\,T}\right) \end{aligned} \tag{2.1}$$

μ is the magnetic moment, g_{Mn} the g-factor for manganese, and B_J is the Brillouin function for angular momentum J. The number of Mn atoms N is substituted with the manganese concentration x times the number of Mn atoms per unit volume N_0.

The obvious approach to increase the magnetization is to increase the manganese fraction x. Now, more often two manganese atoms occupy neighboring sites in the crystal lattice. We cannot assume anymore that the manganese atoms do not interact. The exchange interaction of the Mn atoms manifests itself in an anti-ferromagnetic coupling. This reduces effectively the number of manganese atoms, which participate in the paramagnetic interaction. We introduce x_{eff} as the effective concentration of manganese. The relation to the chemical manganese fraction is shown in Fig. 2.4.

Even if we have considered this antiferromagnetic coupling, the remaining unpaired manganese atoms can interact (antiferromagnetically). This can be taken into account by substituting the real lattice temperature with a phenomenological effective temperature T_{eff} [35]:

$$T \rightarrow T_{eff} = T + T_0 \quad \text{with} \quad T_0 > 0 \tag{2.2}$$

This finally leads to the following Brillouin function that describes the magnetization in the sample:

$$M = -x_{eff}\,N_0\,g_{Mn}\,\mu_B\,S\,B_J\left(\frac{g_{Mn}\,\mu_B\,J\,B}{k_B\,T_{eff}}\right) \tag{2.3}$$

2.2.2 Effect on (conduction) electrons

Nonmagnetic semiconductors in an external dc magnetic field show the formation of Landau levels and further spin-splitting of these levels. Here we want to discuss only the effect of the Mn^{++} on the band structure. Furthermore, we are in particular interested in the effects on electrons in the conduction band. The interaction is called "sp–d" exchange interaction because the s-type and p-type wave functions of electrons and holes, respectively, interact with the d-type wave function of the Mn^{++}ions. The interaction strength is given by J^{sp-d} and dependent on the distance between the conduction band electron (at position $\boldsymbol{r}$) and the Mn^{++}-ion (at $\boldsymbol{R_i}$).
The interaction can be described with a Heisenberg-type Hamiltonian for a spin $\boldsymbol{s}_i$ at position $\boldsymbol{R}_i$ ($\boldsymbol{\sigma}$ are the Pauli spin matrices):

$$H_{ex} = \sum_{\boldsymbol{R_i}} J^{sp-d}(\boldsymbol{r} - \boldsymbol{R_i})\, \boldsymbol{S_i} \cdot \boldsymbol{\sigma} \tag{2.4}$$

As the electron's wave function is strongly delocalized, we can use a molecular-field approximation where we replace the sum over the individual Mn^{++}ions by the thermal average $\langle \boldsymbol{S} \rangle$. We further assume that the magnetic field is along the z axis. Then, we can relate $\langle \boldsymbol{S_z} \rangle$ to the magnetization Eq. 2.3.
Furthermore, we retrieve a lattice-periodic Hamiltonian from Eq. 2.4 if we change the sum over the Mn^{++}ions to a sum over all cations and compensate by adding the fraction of manganese ions as a factor in front:

$$H_{ex} = x\,\sigma_z\,\langle S_z \rangle \sum_{\boldsymbol{R}} J^{sp-d}(\boldsymbol{r} - \boldsymbol{R}) \tag{2.5}$$

Then we can use the same wave functions we would use to solve the non-magnetic Hamiltonian [32] because the lattice periodicity is restored in Eq. 2.5. We calculate the energy shift in the bands from the eigenvalues of the Hamiltonian [32]:

$$\begin{aligned} E_{CB} &= x\,N_0\alpha\langle S_z\rangle m_j \\ E_{VB} &= x\,N_0\beta\langle S_z\rangle m_j \end{aligned} \tag{2.6}$$

α is the conduction-band exchange integral of the Bloch functions and m_j is the angular momentum eigenvalue. For the valence band, the same holds for β. Values can be determined by comparing spin-flip-Raman data with the magnetization of the sample (for ZnMnSe, [36]):

$$\begin{aligned} N_0\alpha &= 243 \pm 10\,\mathrm{meV} \\ N_0\beta &= -1220 \pm 100\,\mathrm{meV} \end{aligned} \tag{2.7}$$

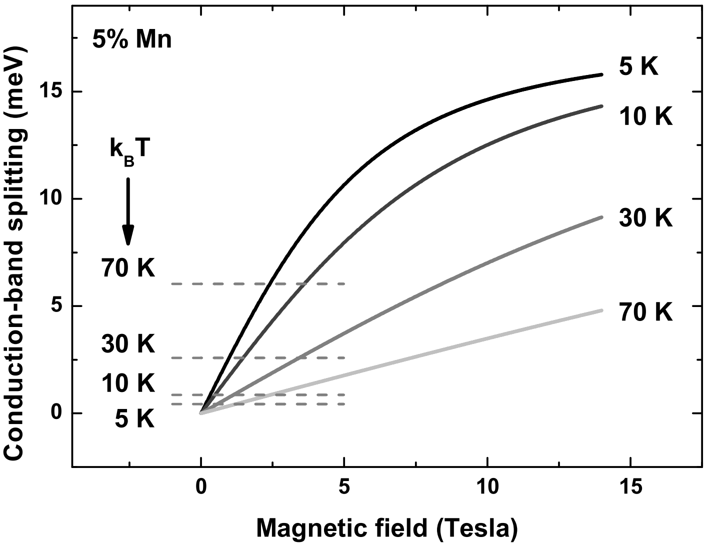

Figure 2.5: Spin-splitting of the conduction band versus external magnetic field, calculated for different temperatures. To obtain high splitting, low temperatures are needed. For comparison, thermal energy is indicated for some temperatures.

The information about the thermal spin distribution $\langle S_z \rangle$ is now obtained from the well-known magnetization formula (Eq. 2.1):

$$\langle S_z \rangle = S \cdot M/(N\,\mu) \tag{2.8}$$

Finally, we get the energy shift of the conduction band states

$$\Delta E_{cb} = x_{eff} N_0 \alpha S_{Mn} B_S \left(\frac{g_{Mn} \mu_B S\, B}{k_B T_{eff}} \right) \tag{2.9}$$

Figure 2.5 shows the splitting of the spin-up and spin-down conduction band states while an external field is applied.

2.2.3 Doping and occupation numbers in ZnMnSe

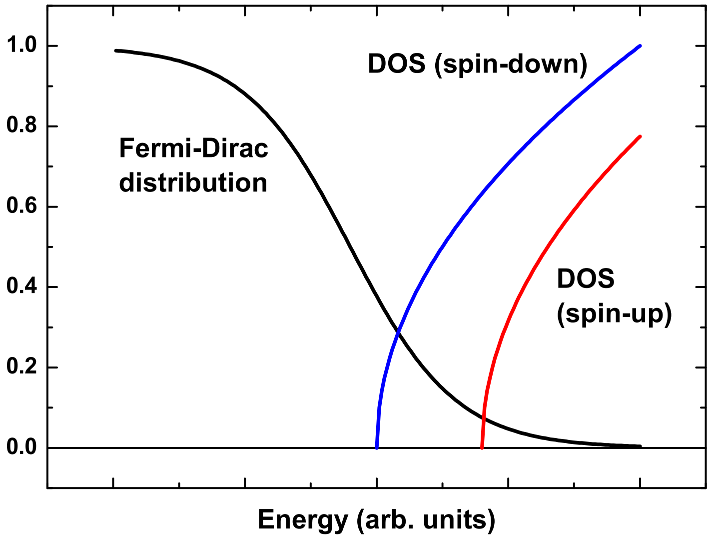

Figure 2.6: The Fermi function and the spin-resolved density of states. The polarization degree is strongly dependent on the Fermi energy!

To achieve electrical transport in the DMS layer a certain amount of donor atoms has to be incorporated. The reason why this plays a major role for spin polarization is shown in Fig. 2.6: High temperatures and/or a high-lying fermi level always lead to occupation of the high-energy spin subband. In ZnSe based semiconductor, the material of choice is chlorine, which has ionization energy of 26 meV in ZnSe [37]. This value is only valid for low concentrations where the Cl ions do not interact. Here, some overlap of the wave functions leads to the creation of a donor band and the activation energy is lowered. In Ref. [38] a value of 18 meV has been observed. We are interested in the occupation of the two spin sub-bands and therefore need to know the Fermi energy. In the absence of acceptors, the charge carrier concentration in the conduction band is given by the concentration of the ionized donors.

$$n = n_d^+ \tag{2.10}$$

First, we neglect the two spin subbands.

We can easily calculate the electron density:

$$n = \int_{E_{cb}}^{E=\infty} 2 \cdot D_{cb}(E) f(E) dE \tag{2.11}$$

E_{cb} is the energy of the lower edge of the conduction band, $D_{cb}(E)$ is the density of states and $f(E)$ is the fermi function. For the case of non-degenerate doping $(E - E_F) \gg k_B T$ holds. Then, the Fermi function can be approximated by the Boltzmann function:

$$f(E) = \left[1 + exp\left(\frac{E - E_F}{k_B T}\right)\right]^{-1} \approx exp\left(-\frac{E - E_F}{k_B T}\right) \tag{2.12}$$

Using the donator density n_d and Eq. 2.10 we obtain:

$$\Rightarrow N_{eff} \cdot \exp\left(-\frac{E_{\mathrm{g}} - E_{\mathrm{F}}}{k_B T}\right) = n_d \cdot \frac{1}{\exp\left(-\frac{E_g - E_{\mathrm{d}} - E_{\mathrm{F}}}{k_B T}\right) + 1} \tag{2.13}$$

The solution to this equation leads to the actual fermi energy.

We discuss now the occupation of the conduction bands in ZnMnSe when an external magnetic field is applied. There, we have to take the giant zeeman splitting into account. The conduction-band splitting is of the order of a few milli electron-volts (see Fig. 2.5). First, the Fermi energy E_{F} is determined as shown above. It is assumed that the band gap is determined by the lowest transition between the Zeeman-split bands. The Fermi energy has to be calculated for each set of simulation parameters (magnetic field, temperature, ZnMnSe parameters). Then, the distribution of electrons in the two bands spin-up and spin-down can be calculated numerically. Also based on $n = \int D(E) f(E) dE$ we get:

$$n_{\downarrow} = \int_{E_{\mathrm{g}} - E_{\mathrm{z}}}^{E_{\mathrm{g}} + 0.2\,\mathrm{eV}} \frac{1}{4\pi^2} \cdot \left(\frac{2m_{\mathrm{e}}}{\hbar^2}\right)^{3/2} \cdot \frac{(E - (E_{\mathrm{g}} - E_{\mathrm{z}}))^{1/2}}{\exp\left(\frac{E - E_{\mathrm{F}}}{k_{\mathrm{B}} T}\right) + 1} \cdot dE \tag{2.14}$$

$$n_{\uparrow} = \int_{E_{\mathrm{g}} + E_{\mathrm{z}}}^{E_{\mathrm{g}} + 0.2\,\mathrm{eV}} \frac{1}{4\pi^2} \cdot \left(\frac{2m_{\mathrm{e}}}{\hbar^2}\right)^{3/2} \cdot \frac{(E - (E_{\mathrm{g}} + E_{\mathrm{z}}))^{1/2}}{\exp\left(\frac{E - E_{\mathrm{F}}}{k_{\mathrm{B}} T}\right) + 1} \cdot dE \tag{2.15}$$

E_{z} is the Zeeman splitting of the spin states. It is dependent of the parameters of the spin-aligner: The effective manganese concentration and the effective temperature. We calculate then the degree of electron spin polarization P with the usual equation

$$P = \frac{n_{\downarrow} - n_{\uparrow}}{n_{\downarrow} + n_{\uparrow}} \tag{2.16}$$

Fig. 2.7a compares the result of our calculation with experimental data. The electron spin polarization has experimentally been determined by observing the highest quantum-dot ensemble polarization in a spin-LED device. The observed spin polarization does never reach unity which will be explained later in the single quantum-dot experiments. However, the polarization is diminished by a constant factor and that justifies the use of the high-energy quantum-dot emission polarization as a measure for the electron polarization efficiency of the spin aligner. Having this in mind, experiment and theory in Fig. 2.7 agree very well! The samples of this series are shown in Table 2.1.

Sample	Nominal donor concentration	Hall n (RT)
SL2E18	$2 \cdot 10^{18}$ cm^{-3}	$\sim 2 \cdot 10^{18}$ cm^{-3}
SL1E18	$1 \cdot 10^{18}$ cm^{-3}	$\sim 8 \cdot 10^{17}$ cm^{-3}
SL2E17	$2 \cdot 10^{17}$ cm^{-3}	~ 0 cm^{-3}
SL0E0	0 cm^{-3}	~ 0 cm^{-3}

Table 2.1: Samples of the doping series. The doping concentration is calibrated with a series of Hall-samples. The thickness of its ZnMnSe layer was 1 µm only, thus determination of the carrier concentration is difficult for low doping densities.

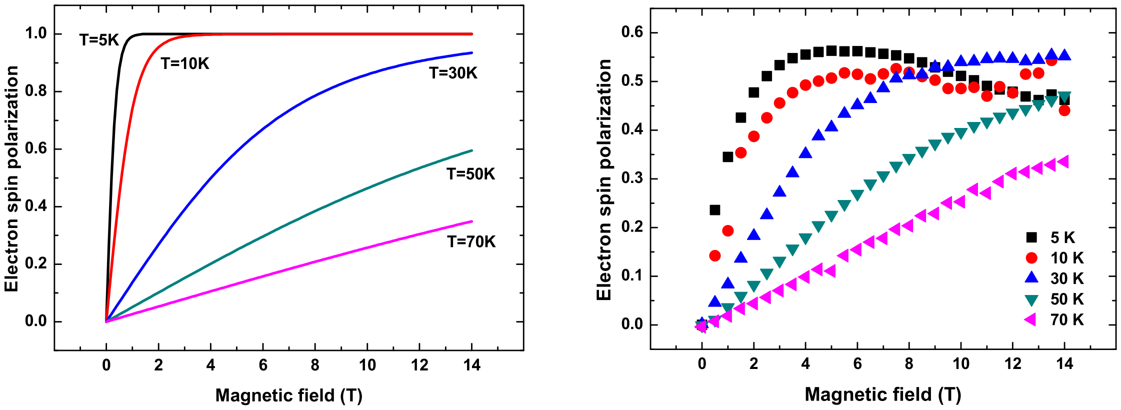

(a) Simulated electron spin polarization

(b) Experimental results

Figure 2.7: Comparison of the simulation and the experimental results (sample SL2E17) for a non-degenerate doped spin aligner. The dependency on temperature is strong but for low temperatures we reach unity spin polarization at low magnetic fields. Experiment and theory agree qualitatively very well.

Degenerate doping.

Now we consider higher doping concentration where the donor concentration is of the order of the effective density of states (see Eq. 2.13). Then, the Fermi level is very close to or even in the conduction band. The Fermi exclusion principle leads to occupation of higher states. Easily, states in the minority spin subband are occupied even at low temperature and electron spin polarization is reduced. In contrast to the non-degenerate case, the temperature dependency of electron concentration in the conduction band is reduced. The only quantity strongly depending on the temperature is the magnetization of the manganese ions in ZnMnSe.

We find the point where we enter the degenerate regime by comparing the donor

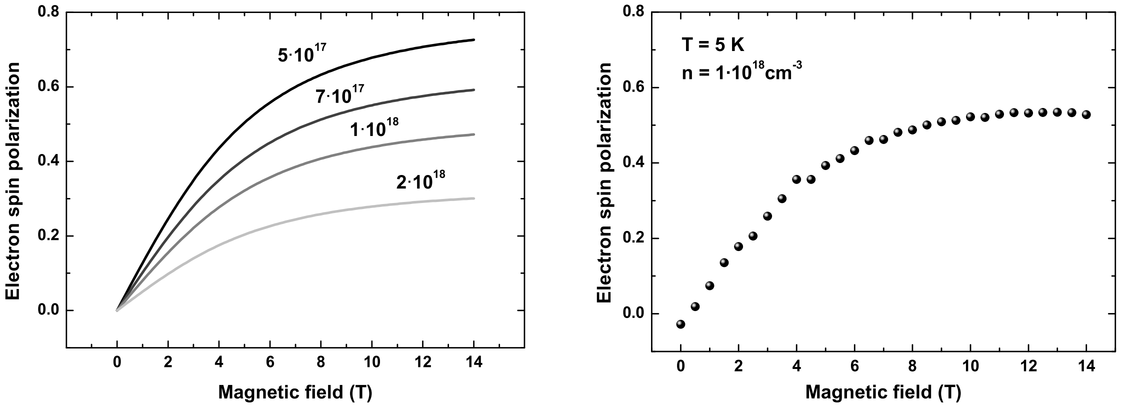

(a) Simulated electron spin polarization (b) Experimental results

Figure 2.8: Comparison of the simulation (doping concentration given in cm^{-3}) and the experimental results (sample SL1E18) for a degenerate doped spin aligner. Theory and experiment agree very well. The performance of the spin aligner is obvisously poor, unity spin polarization can never be achieved.

concentration with the effective density of states from Eq. 2.13. The most important change for the theory is that the approximation

$$E_g - E_F \ll k_B T$$

cannot be used anymore. Therefore, the Fermi function cannot be approximated by the Boltzmann distribution anymore. The main point concerning spin polarization is shown in Fig. 2.8. The resulting spin polarization does not reach unity, even from the theoretical point of view (Fig. 2.8a). That is clear if we remember the distribution of the electrons in the Zeeman-split conduction bands in Fig. 2.6. Here experiment and theory agree also quantitatively quite well. The reason is that the loss of spin polarization in our samples is caused by randomization of the spin, not by a preferred relaxation into a certain spin state. Accordingly, for lower initial spin polarization the effect of this randomization is lower than for the case of high initial spin polarization in the non-degenerate case in Fig. 2.7.

Band structure.

What is the influence of doping on the spatial band structure? Fig. 2.9a shows calculations for two doping concentrations. In the low-doping limit, the Fermi level is well separated from the conduction band in ZnMnSe. In contrast, for the degenerate case, it is close to (or in) the band. From Fig. 2.9a we can expect that the doping

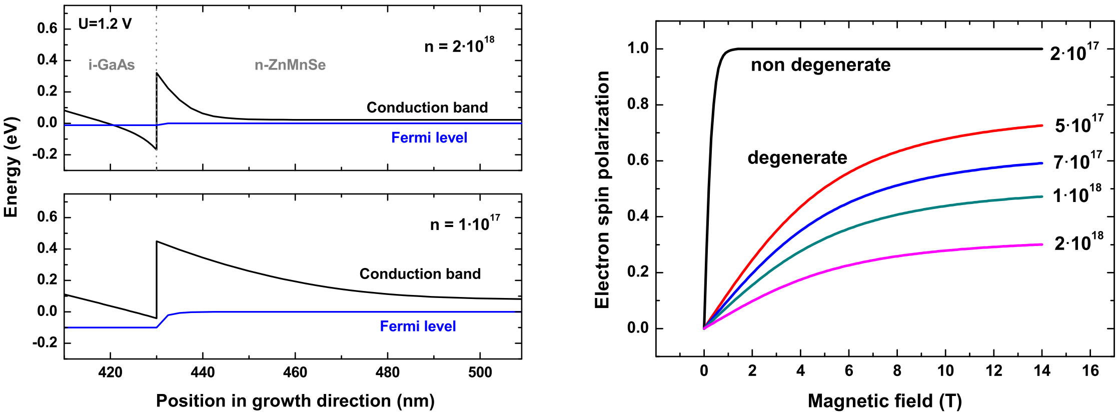

(a) The fermi level in real space simulated for $U = 1.2V$.

(b) Comparison of theoretical spin polarization for the two cases.

Figure 2.9: Left: Comparison of degenerate and non-degenerate doping in real space. We come back to it's influence later. Right: Comparison of spin polarization for degenerate and non-degenerate doping concentration taken from our simulation experiments. The polarization is strikingly different, thus we need to be sure to stay in the low-doping range.

concentration in ZnMnSe has more general impact on the operation of the device. We come back to this in the chapter about the spin-LED.

These findings do not only concern investigations where electrons will be stored in quantum dots, but also in spin transport experiments with electrons. There, the optimum between low resistivity (high doping) and ease of spin-alignment (low doping) has to be found. If low temperatures and high magnetic fields are applicable, one has only to care about not leaving the non-degenerate regime.

2.2.4 Spin relaxation in the DMS

In the previous paragraph we have shown the very promising properties of the diluted magnetic semiconductor ZnMnSe. Here, unpolarized electrons enter the conduction band in the n-doped region. During the short transport through the spin-aligner layer all spins must have relaxed into the lower-lying spin subband to be as effective as possible. Which spin relaxation mechanisms are important? Can we enhance one of them to reduce the needed layer thickness?

The DMS ZnMnSe grown on GaAs shows complex physics which makes theoretical calculations of spin relaxation complicated: Depending on growth conditions strain is introduced and because strain can relax by formation of stacking faults, it is not homogeneous in a sample. Additionally, spin relaxation via the strong sp–d interaction has to be taken into account. Theoretical investigations like in Ref. [39] resulted in a complicated dependency of relaxation time on sample conditions. Later experiments show that electron and hole spin relaxation seems to be very efficient, around 10 ps for electrons and some 100 fs for holes in time-resolved modulation spectroscopy [40]. Time-resolved magneto-optical Kerr effect measurements resulted in $0.1 \ldots 1$ ps for electrons as well as for holes [41]. As most experiments show an increase of spin-flip rate with manganese-ion concentration, the dominant mechanism seems to be magnetic exchange interaction of the conduction-band electron with the magnetic ions. For excitons, these interactions have only recently been investigated [42, 43].

In an electrical device, electrons get polarized while passing through the ZnMnSe layer. We conducted series of Hall measurements for determination of the carrier concentration and electron mobility μ. The results (shown in Table A.1) depend as expected on the carrier concentration. We take as an average value

$$\mu = 200\,\frac{\mathrm{cm}^2}{\mathrm{Vs}}$$

From band-structure calculations (shown later, see Fig. 2.9) we deduce an electric field $\boldsymbol{E}$ in the spin aligner of 6×10^{-7} V/nm. That leads to a drift velocity in growth direction $\hat{\boldsymbol{z}}$ of

$$\boldsymbol{v_d} = \mu \boldsymbol{E} = -18\,\mathrm{m/s} \cdot \hat{\boldsymbol{z}}$$

We prepared two samples with spin-aligner thicknesses of 250 nm and 750 nm, respectively. Growing even thicker spin-aligners is not advisable because growth conditions will change during extended periods. The electron transit time can be estimated to be 13.3 ns and 41 ns for the thin and thick layer, respectively.

Electron spin polarization as a function of the magnetic field is shown in Fig. 2.10. Obviously, the polarization of the 250 nm sample is reduced. Because other sample parameters can influence the polarization, too, we do not exactly know if the polarization of the 750 nm sample at high fields (0.41) is limited by the spin-aligner thickness or other causes. Results presented later in this work suggest that 750 nm spin aligner is sufficient for near-unity polarization.

To get an impression how long the effective spin relaxation time is we fitted the experimental data with a model for spin relaxation. The best-fit result is shown as the line in Fig. 2.10. It was received with the following parameters (P_{max} is the maximum polarization and τ the spin relaxation time):

$$P(t) = P_{max}\left(1 - e^{t/\tau}\right) \quad \text{with} \quad P_{max} = 0.43\,, \quad \tau = 10\,\mathrm{ns}$$

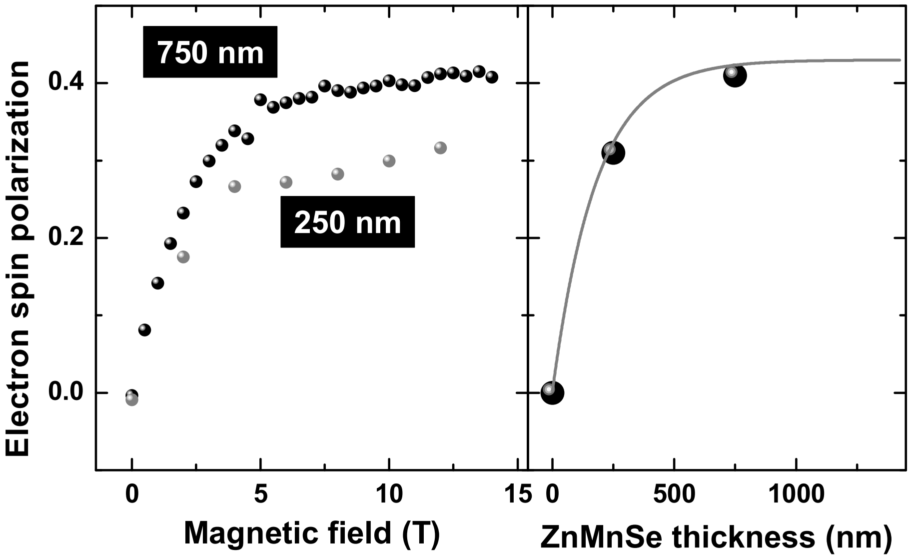

Figure 2.10: Left: Averaged electron spin polarization for the 250 nm and 750 nm sample (SL250 and SL750, respectively). Right: Maximum polarization as a function of thickness. The line is a fit as explained in the text.

Unfortunately, we do not have enough data to state definitely that this is the electron spin relaxation time in ZnMnSe. In literature there is very few information about electron spin relaxation in DMSs: Based on spin-flip-Raman scattering data, Lentze et al. [44] deduced an electron relaxation time of 5.5 ps. Time-resolved Kerr rotation on n-doped quantum-well samples resulted in 1 . . . 10 ps relaxation time [41]. This fast relaxation is well explained within the picture of s-d electron scattering from Bastard et al. [45].

The very long spin relaxation rate in the nanosecond range suggests that the spin relaxation is strongly influenced by other sample parameters. For example, scattering at defects in the crystal. That leads us to the next section where lattice mismatch is investigated briefly.

2.2.5 Epitaxy of the spin aligner

Growth of semiconductor heterostructures by molecular beam epitaxy is only possible in a well-defined and reproducible way if the following conditions are met:

The growth temperatures must be compatible: Growing ZnMnSe on GaAs is possible since growth of GaAs happens above 550 °C and ZnMnSe below 400 °C.

The opposite approach, growing GaAs-based structures on a ZnSe substrate is impossible due to desorption of the substrate at GaAs-growth temperature.

The crystal system must match: In our case, we want to deposit the spin aligner on GaAs, which crystallizes in the cubic system in zincblende structure. $\mathrm{Zn_{1-x}Mn_xSe}$ crystallizes in different ways depending on manganese concentration: in zincblende structure for $x = 0 \ldots 0.35$, wurtzite for $x = 0.35 \ldots 0.57$ and in a solid solution of wurtzite and rocksalt for $x > 0.57$.

The lattice constants should be similar: GaAs has an in-plane lattice constant of $a_0 = 5.65325\,\text{Å}$. The lattice constant of $\mathrm{Zn_{1-x}Mn_xSe}$ has also here been investigated in the context of this work [46]. Vegard's law is in good agreement with experimental data [47] and the lattice constant can be calculated with

$$a_{0,\mathrm{Zn_{1-x}Mn_xSe}} = \sqrt{2}\,(4.009 + 0.1645 \cdot x)\ \text{Å}$$

where x is the manganese concentration. Depending on the lattice mismatch, the epilayer grows fully strained on the substrate without dislocations or the epilayer relaxes via formation of dislocations to its intrinsic lattice constant. The thickness at which this happens is called critical thickness.

All samples presented here are grown fully relaxed above the critical thickness. The critical thickness is not well known, but for ZnSe on GaAs it is about 200 nm. The intrinsic lattice constant for a $\mathrm{Zn_{0.95}Mn_{0.05}Se}$ spin-aligner layer is $a_0 = 5.68121\,\text{Å}$. The lattice mismatch f on GaAs is

$$f = \frac{a_{substrate} - a_{epilayer}}{a_{epilayer}} = 0.5\%$$

In cross-section transmission-electron microscopy images dislocations can be seen, Fig. 2.11 and Fig. 2.12 show images for 5% and 13% manganese.

We preferred to introduce 13% manganese as this maximizes the effective g-factor (see Fig. 2.4. At higher Mn concentration a lower external magnetic field is needed to obtain the same spin polarization. However, the measured spin-polarization of $\mathrm{Zn_{0.87}Mn_{0.13}Se}$ is lower than in 5% samples, which can be explained by the high dislocation density seen in Fig. 2.12.

Therefore we investigated the incorporation of sulfur in ZnMnSe: Sulfur decreases the lattice constant of the quaternary material ZnMnSSe in comparison to ZnMnSe.

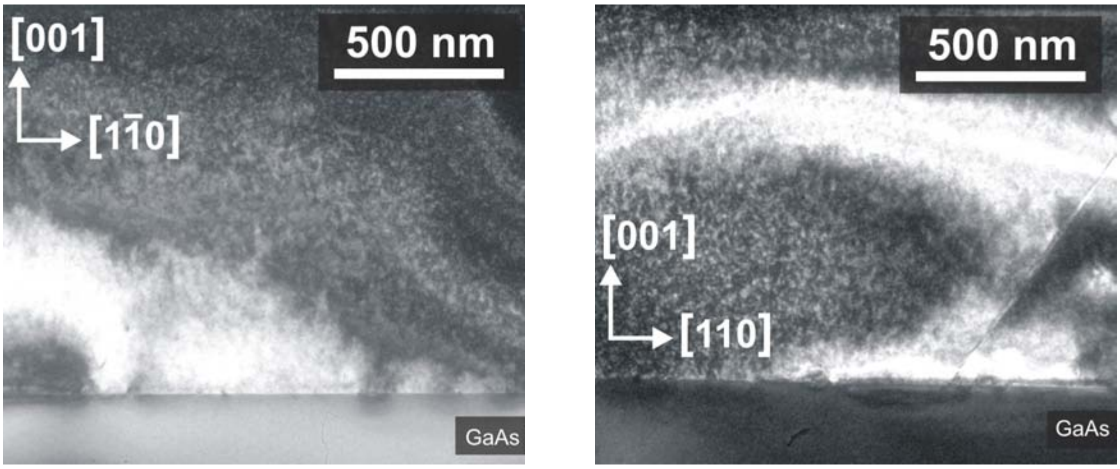

(a) [110] direction (b) [1$\bar{1}$0] direction

Figure 2.11: Cross-section TEM images in two different crystallographic directions for a 5% Mn spin aligner. The material is nearly dislocation-free; only one stacking fault can be seen on the right.

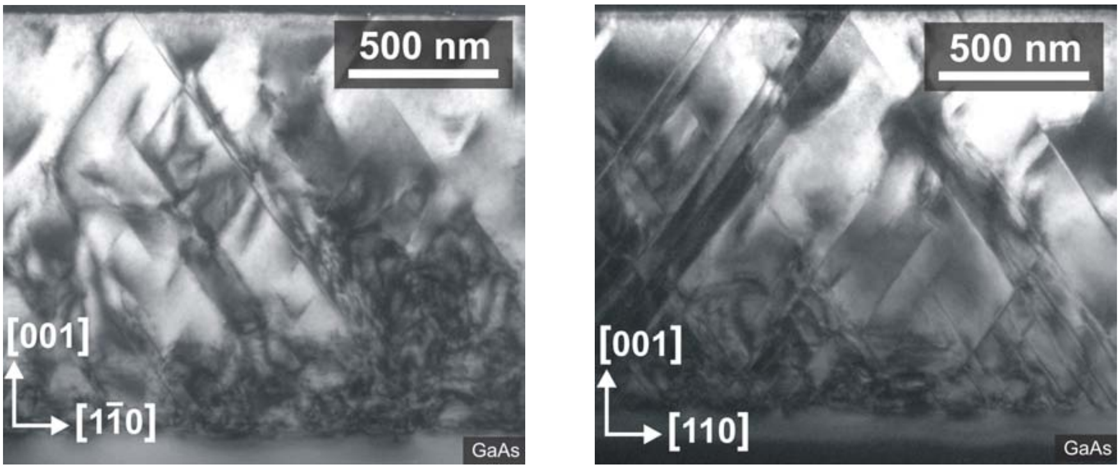

(a) [110] direction (b) [1$\bar{1}$0] direction

Figure 2.12: Same images for a spin aligner containing 13% manganese. The defect density is very high, especially near the III-V/II-VI interface.

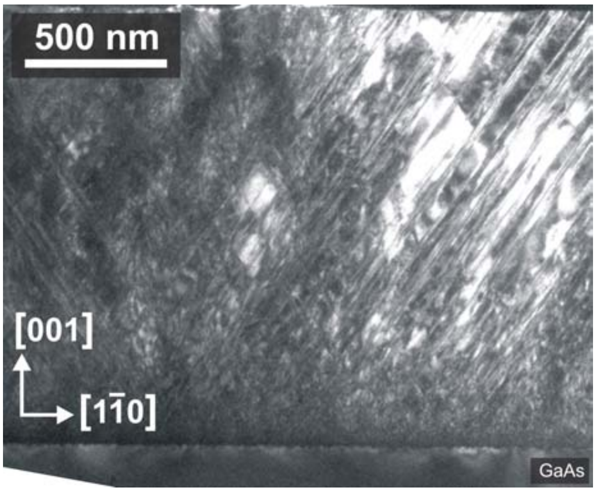

Figure 2.13: This $Zn_{0.87}Mn_{0.13}S_{0.17}Se_{0.83}$ layer is nominally lattice-matched to the GaAs substrate at high manganese concentration. The growth is not as clean as in the case without sulfur.

Thorough investigations of the new material ZnMnSSe (yet unpublished) show that the ideal composition should be $Zn_{0.87}Mn_{0.13}S_{0.17}Se_{0.83}$. It turned out that a huge problem is the crystal quality of sulfur-containing layers. This well-known fact is shown in transmission electron microscopy (TEM) images (see Fig. 2.13). However, after growth optimization we were able to obtain the same electron spin polarization as in $Zn_{0.95}Mn_{0.05}Se$.

2.3 Conclusions

Diluted magnetic semiconductors like ZnMnSe are ideal to achieve near-unity spin polarization for conduction-band electrons (and also for holes!). For quantum-information experiments, low temperature (inhibited dephasing due to phonons) and a magnetic field (to give the electron a quantization axis) are needed anyways. Therefore ZnMnSe as spin-aligner outperforms easily other possible alignment methods.

However, as we have shown in Sect. 2.2.3, this task is not straightforward and various constraints have to be taken into account. From our experiments, we can give the best parameters:

Mn concentration:	5%
Cl doping concentration:	$2 \times 10^{17}\,\mathrm{cm}^{-3}$
ZnMnSe thickness:	$\geq 750\,\mathrm{nm}$

Further results in this work give hints that this method can fully compete with optical initialization methods.

Chapter 3

Spin storage and read-out

The main part of a future quantum information processing system is the storage unit. The constraints to these are very stringent: Unwanted interaction between the qubits must be inhibited. In our case of the spin qubit possible interactions are JJ coupling, hyperfine interaction with angular momentum of the nuclei, and spin-orbit coupling.

On the other hand, we need to manipulate the states (selectively) to realize gates and read out the spin-state in the end. Semiconductor quantum dots fulfill these two requirements because the coupling to the electromagnetic field can be switched on or off by adding or removing an additional hole to/from the dot! In 2DEG (2-dimensional electron gas) quantum dots and in atom traps other parameters have to be adjusted to tune states into or out of resonance (magnetic field, gate voltage).

In our current devices however, the injection of holes to read-out the electron's spin is uncontrolled. Nevertheless, for the present investigation on feasibility of the quantum-dot system this controllability is not needed.

In Chap. 3.1, we will first describe the quantum-dot system we use and present basic characterization. These prerequisites allow for realistic numerical simulation of the electronic states in the dots (Chap. 3.2). Having that information we then can fully understand the electronic structure.

In Chap. 3.3 we address several advanced issues about quantum dots: The coupling to photons, their properties which make them suitable for qubits as well as electron spin relaxation and dephasing in a quantum dot.

3.1 Self-assembled InAs quantum dots

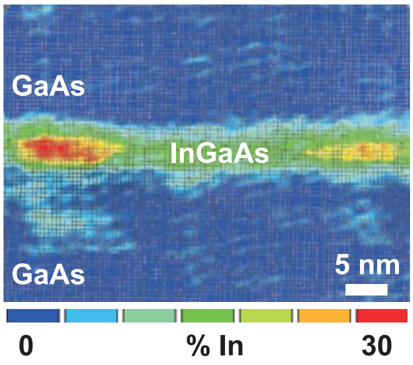

Figure 3.1: CELFA analysis of high-resolution TEM image of InAs quantum [1].

Without deeper insight, the producers of colored church windows in the gothic era already used quantum effects: Depending on the size of the embedded gold nanoparticles the plasmon resonance shifts and the absorption spectrum is changed, leading to beautiful colors. Faraday was the first to initiate the search for explanations in the 1850s and Mie provided the theory explaining this phenomenon in 1908 [48]. Also nanoscale semiconductor materials were used before effects were explained: In Victorian era cadmium sulfide and selenide was added to a glass melt and the first man-made nano-crystals were produced[2].

The first specific quantum structures were quantum wells, developed in the early 1970s. Because of their huge impact for all modern optoelectronic devices, Z.I. Alferov and H. Kroemer won the Nobel price in 2000.

The thermodynamical foundation for self-assembled formation of semiconductor quantum dots being known for 60 years [50], the realization took a while [51]. Similar growth has been observed presumably many times before but 3-dimensional island growth was considered detrimental for heterostructure growth (for a recent review, see e.g. [52]). Therefore, the electronic shell structure has been discovered in other systems first: For example, three-dimensional confinement for the electron wave function and therefore quantum effects has been seen in quantum-well pillars [53]. The lateral confinement was given by the sample boundary.

Certainly, a much more efficient way to produce large amounts of quantum dots is via self-assembly. The figure on the right shows a cross-section high-resolution transmission-electron microscopy (HR-TEM) image of two adjacent quantum dots. By analyzing a chemical sensitive e-beam diffraction spot, the indium content has been determined (Composition estimation by lattice fringe analysis (CELFA) [54]).

The confinement in all three spatial directions is given by the conduction- and valence-band discontinuity between the two materials, GaAs and $\mathrm{Ga_{1-x}In_xAs}$. In the latter material, electrons (and holes) have a smaller potential energy. Both carrier types are confined in the indium-rich regions. In Fig. 3.1 the quantum dot, where the indium concentration is at maximum, is embedded in a 2D layer of InGaAs.

---

[2] For a review, see [49]

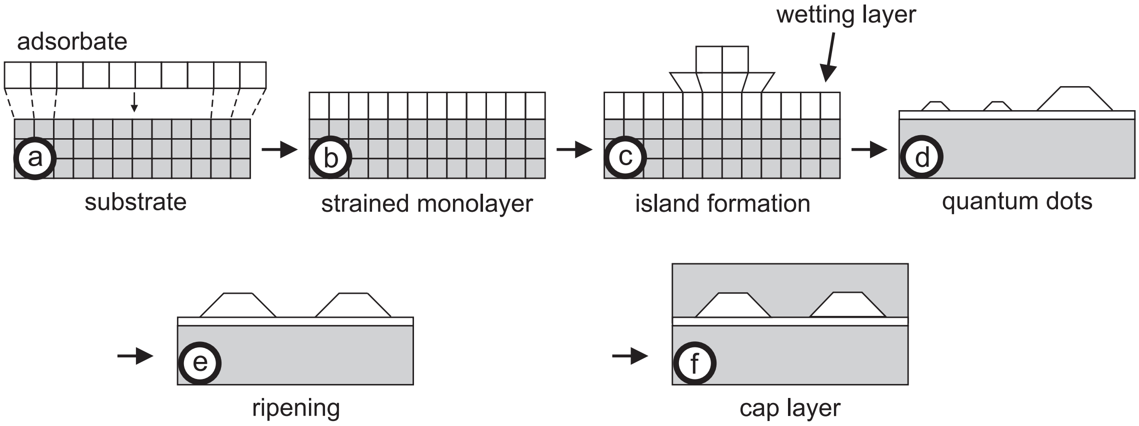

Figure 3.2: Growth of Stranski-Krastanow quantum dots. The in-plane lattice constant of the dot material is larger than in the matrix material. In figure (d), the scale is reduced. Typical self-assembled quantum dots show lateral diameters between 5 and 100 nm.

Preparation. The formation of quantum dots by MBE (molecular beam epitaxy) growth is outlined in Fig. 3.2. The first monolayers of the dot material (InAs) deposited on the matrix material (GaAs) adopts its lattice constant. That leads to a strained layer (a, b). After continued deposition of InAs, the adsorbate forms small islands these being thermodynamically (minimization of surface energy) more favorable (c). The point this happens is called the critical thickness. Upon further deposition (or during a growth interruption, too), indium atoms diffuse over the sample surface and preferentially larger islands will form (d). Strain can also get reduced by the formation of dislocations, which is unwanted here and can be avoided by careful adjustment of the growth conditions.

The dots at this stage can easily be investigated by atomic force microscopy (AFM) to find out the dimensions as well as the density (see Fig. 3.3). However, optical experiments are not possible due to the surface states, which would capture all carriers. The solution is to completely embed the dots in GaAs by following GaAs deposition. During this deposition (the cap layer, Fig 3.2 (f)), indium can diffuse and segregate even further, depending on sample temperature. That leads to the formation of a washed-out wetting layer and to dots in form of In-rich islands within an InGaAs quantum well in Fig. 3.1.

A typical photoluminescence spectrum of such a sample is shown in Fig. 3.4. The broad low-energy peak originates from the quantum dot ensemble. The broadening is solely due to the inhomogeneous size and indium content distribution of the dots (inhomogeneous broadening). The wetting layer peak corresponds to a quantum well

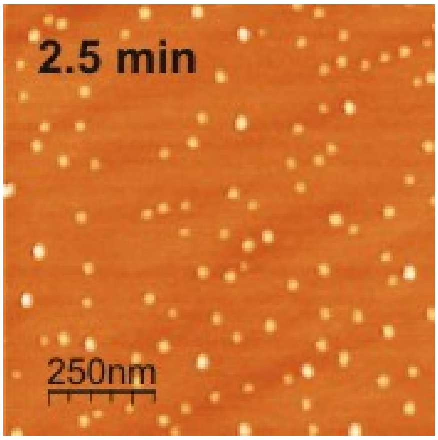

Figure 3.3: Atomic force microscope image of an uncapped quantum-dot sample. AFM investigations were done by D. Hu and D. Schaadt.

about the critical thickness wide. The higher-energy peaks originate from the matrix material GaAs. Most likely, even the free exciton is observable. That proves an important aspect of the growth of self-assembled quantum dots: three-dimensional confinement for charge carriers is produced while the ultra-clean crystal structure of the host material is retained.

By adjusting the MBE growth parameters, the emission energy of the quantum dots can be adjusted over a broad wavelength range. Basically three parameters determine it: The amount of InAs deposited, the magnitude of In diffusion on the sample (which in turn is determined by a combination of temperature and duration of the growth interruption after deposition) and a possible subsequent annealing of the capped sample. These parameters have been optimized in the current work (some growth results are given in [55]). Besides that, the tuning range can be expanded using other methods like changing the confinement by altering the composition of the barriers.

For our purposes, we tuned the growth to produce high-energy quantum dots, very small in volume with relatively high indium content (for example, see [55, 56]). There, the confinement energy compensates for the low band gap due to high indium concentration. The method of choice turned out to deposit an amount of InAs close to the critical thickness [55]. Then, small dots can be formed. In Chap. 3.3, the properties, which make the (small) dots suitable as storage for electron-spin qubits are discussed.

For spectroscopic investigations, the dot density is also of very high interest. A low densities makes them more easily separable in order to investigating single dots.

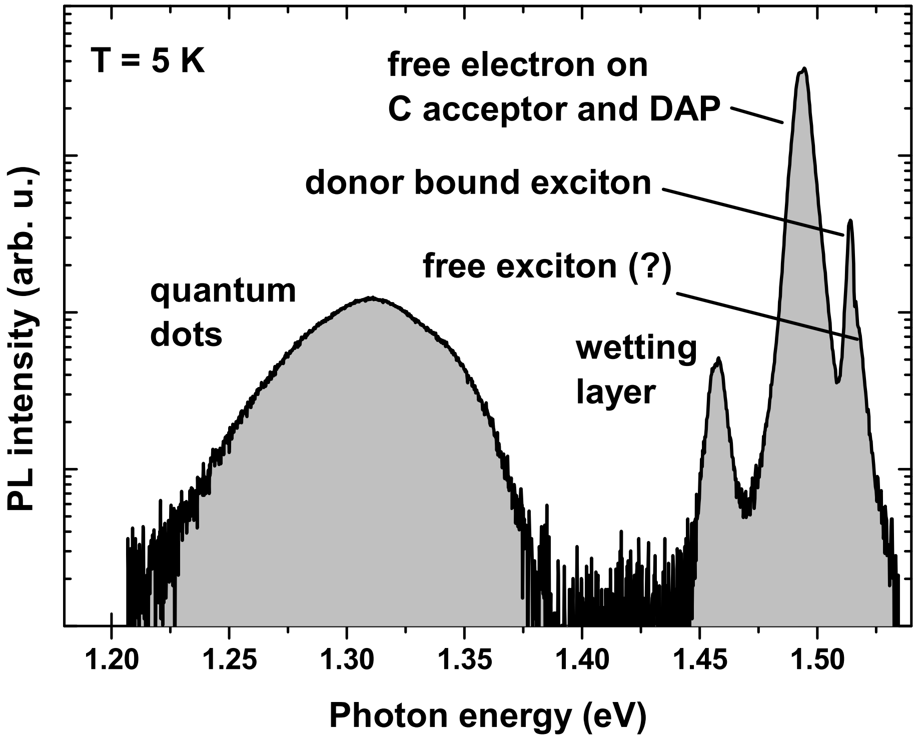

Figure 3.4: Photoluminescence of an InAs quantum-dot sample (A0300). Electron-hole pairs were excited by a He-Cd laser with the 2.8 eV line well above the band gap of GaAs. The peaks below 1.47 eV correspond to optical transitions in the indium-containing region; the higher ones to GaAs bulk material.

3.2 Electrons and excitons in InAs/GaAs quantum dots

As quantum dots are commonly referred to as artificial atoms, we outline the evolution from the isolated atom to the bulk semiconductor and back to the artificial atom, the quantum dot, in Fig. 3.5: The discrete energy structure of the single atom is lost if a great number of atoms are arranged in a periodic structure, the crystal (b). The well-known energy bands of a semiconductor evolve from interacting atomic levels. They are divided in occupied (valence) and unoccupied (conduction) bands separated by the band gap. Using a small inclusion of a semiconductor with a lower band gap than the surrounding material, the electron wave function is localized in the inclusion. Quantized electronic states with discrete energy levels form in this dot in the same manner as they do in the atomic potential (c).

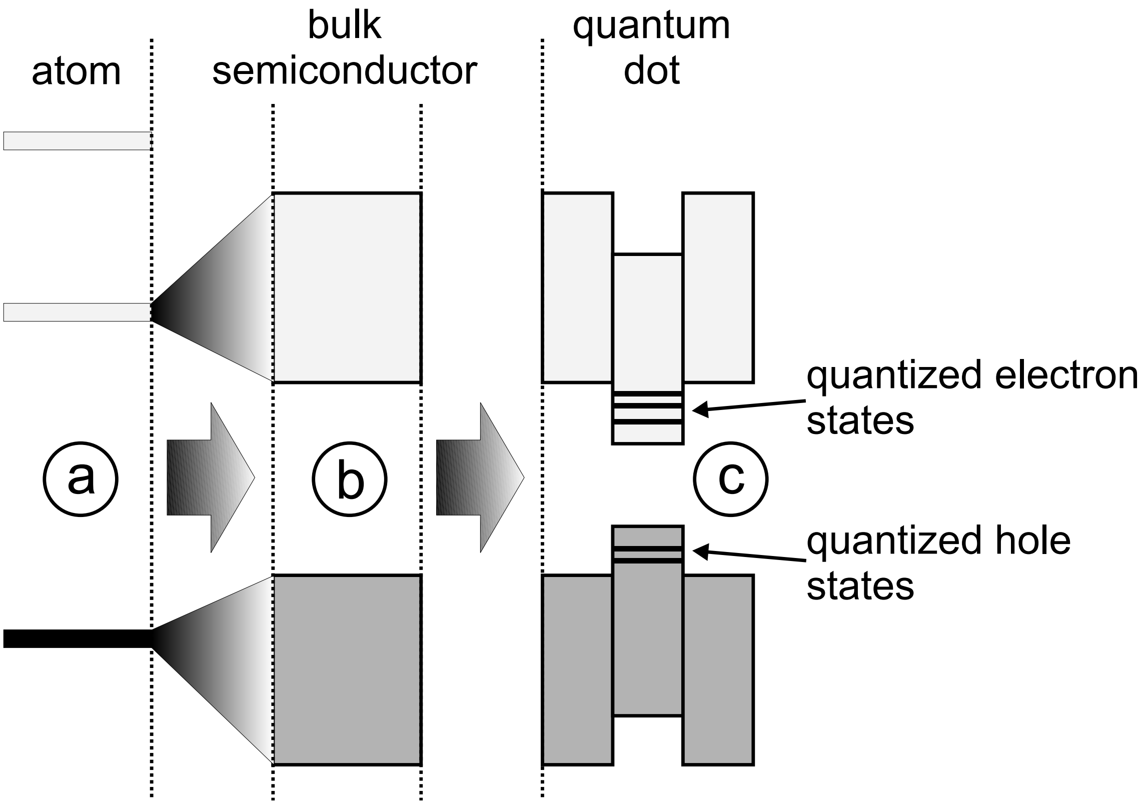

Figure 3.5: Starting from atomic orbitals (a), we put these closer together until electronic bands form due to interaction of the states (b). If one makes a three-dimensional heterostructure with an inclusion of lower-band-gap material, the quantum dot, discrete electronic states emerge (c).

Excitons in quantum dots. In semiconductor bulk material, an electron and a hole can form a bound electron-hole pair, the exciton. Similar to the atom, discrete energy levels emerge between the exciton ground state (band gap energy minus the binding or Rydberg energy) and the band edge. The excitonic Rydberg energy is much lower than in the hydrogen atom because the semiconductor material's dielectric response shields the electric field from the carriers and the effective masses of electron and hole are smaller in the dot than that of the free electron and proton.

In addition, an excitonic Bohr radius a_X can be defined. Its definition is similar to the hydrogen's Bohr radius, but the values are much larger. In fact, they are of the same order of magnitude as the de Broglie wavelength of the electron (order of nanometers). That means that two competing quantization mechanisms are present in a quantum dot: The Coulomb-confinement of the exciton and the band structure confinement. We have weak confinement in large dots where excitons move quasi-freely around and strong confinement in small dots where excitonic and quantum-dot states are

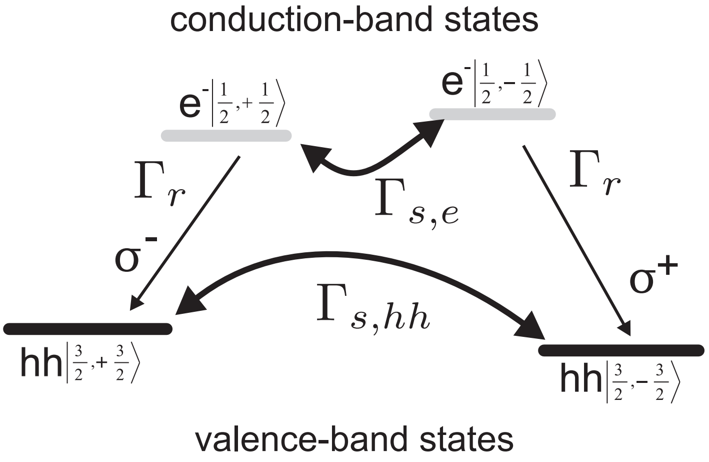

Figure 3.6: The optical selection rules in (small) InAs quantum dots in an external magnetic field.

indistinguishable. In the present work, we always deal with strongly confining dots: The excitonic Bohr radius in InAs is about 5 nm and the dot size is of the same order.

After (non) resonant excitation or electrical injection of an electron-hole pair in the dot, the electron and the hole recombine by emission of a photon after the half-life τ_{rad}. Due to the strong wave function overlap in the quantum dot, non-radiative recombination channels are suppressed. The valence-band heavy-hole – light-hole degeneracy is lifted (by quantization and strain), therefore strict optical selection rules determine the helicity of the emitted photon as shown in Fig. 3.6. This works as expected if electron and hole spin are compatible for an optical dipole transition. If not, we have to compare the spin-relaxation rates: The heavy-hole spin-relaxation rate $\Gamma_{s,hh}$ is usually faster than that of electrons $\Gamma_{s,e}$. Because the latter is much smaller than the radiative recombination rate Γ_r (i.e. the electron spin is frozen during the radiative lifetime of the electron-hole pair), the helicity of the photon is a direct measure for the electron spin. This is commonly assumed in InAs quantum dots (for example, see [57]). We will come back to this later in Chap. 3.3.1

3.2.1 Morphology of quantum dots

By adjustment of the MBE growth parameters quantum dots with different morphology can be obtained. Here we present the growth conditions and basic characterization of two types of quantum dots, which will be discussed later in the context of spin-injection LEDs.

For the so-called high-energy dots, indium was deposited at a very low indium flux (see Table 3.1). During that deposition, indium atoms can diffuse on the surface.

Even if the amount of indium is very close to the critical thickness, quantum dots form. In Fig. 3.7b, upper panel, cross-sectional TEM images are shown. We hardly see the accumulation of indium that leads to three-dimensional confinement of the carriers!

The chemical analysis with atomic resolution (Fig. 3.7, lower panels) is done by observing a chemically sensitive reflex in a transmission electron microscope. The intensity of that reflex is a direct measure of the indium concentration at that place (in high-resolution TEM a single pixel ("atom") originates from a column of atoms, about 20 nm in height). The method is therefore called "content estimation by lattice fringe analysis" [54].

This analysis gives us much more information about the shape of a quantum dot than plain HR-TEM images.

Table 3.1: Growth conditions for the quantum dots.

	Low-energy dots	**High-energy dots**
Growth temperature	500 °C	500 °C
As:In ratio	17:1	80:1
Monolayers deposited	2.25	1.85
Monolayers/s	0.09	0.0056
Growth interruption	30 s	10 s
Dot density	$2.5 \times 10^{11}\,\mathrm{cm}^{-2}$	$1.2 \times 10^{10}\,\mathrm{cm}^{-2}$

The nomenclature of high- and low-energy quantum dots becomes clear by comparing the luminescence spectra (Fig. 3.8): The low-energy quantum dots, which are grown at higher InAs growth rate (higher In/As pressure ratio) are more extended in vertical dimension and therefore their quantization energy is reduced. It is also clear that in both quantum-dot ensembles there are comparable dots because the luminescence spectra overlap. To learn more about the electronic structure we must investigate single quantum dots. To find out whether the HR-TEM images above are representative for the dots and if the information about indium distribution (from CELFA) is correct, we have to compare single-dot experimental results with numerical simulations. This is subject of the next sections.

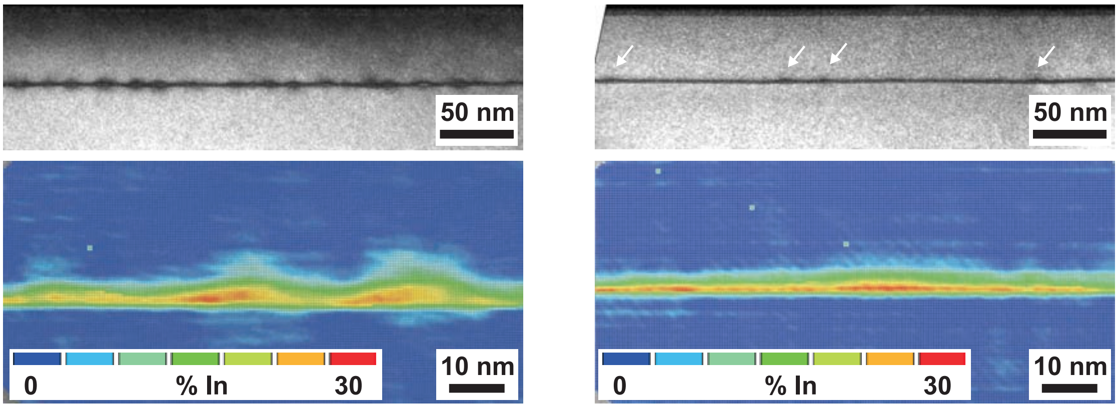

(a) Low-energy quantum dots (b) High-energy quantum dots

Figure 3.7: High-resolution transmission electron microscopy images of low- and high-energy quantum dots (sample QDLE and QDHE, respectively). The upper panel gives an overview of the dots while the lower panel shows the indium content by CELFA analysis.

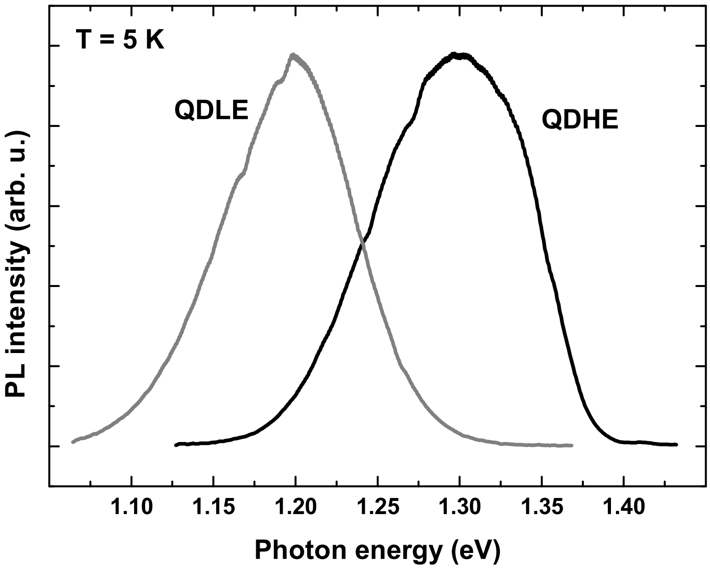

Figure 3.8: Photoluminescence spectrum of the low-energy (QDLE) and high-energy (QDHE) quantum dot samples. It is recorded under non-resonant excitation above the GaAs band gap.

3.2.2 Band structure and wave function calculations

The particular structure of the electronic states in the dots is also of high interest to understand possible spin relaxation channels and electron injection mechanisms. Therefore, we will compare numerical state calculations with experimental luminescence data. First, we need to model the spatial composition profile of a quantum-dot. We have analyzed many high-resolution TEM images as well as CELFA analysis data like in Fig. 3.7. Based on that information, we have modeled several quantum dots and one of them is presented in the following.

The simulation volume (width 80 nm × depth 80 nm × height 100 nm) contains the quantum dot and part of the surrounding wetting layer and GaAs as shown in Fig. 3.9b. The x coordinate is along [100], y along [010] and z is along [001] crystallographic axes.

The wetting layer is approximated by a non-constant, Gaussian-shaped indium content distribution χ like $\mathrm{In}_\chi\mathrm{Ga}_{1-\chi}\mathrm{As}$. It starts at $z = 45\,\mathrm{nm}$, reaches its maximum of 15% at $z = 50$ nm and goes down back to zero at $z = 55\,\mathrm{nm}$. The width is about 7 nm.

The quantum dot is vertically centered in the wetting layer. We approximated the dot as a semi-ellipsoid with a base diameter of 20 nm at $z = 47.5\,\mathrm{nm}$ and its tip at $z = 52.5\,\mathrm{nm}$, centered in the simulation volume. To model the complicated indium distribution in the dot, we again assumed a Gaussian profile with $\chi = 40\%$ in the dot center at $z = 50\,\mathrm{nm}$ and $\chi = 11\%$ at the border. The lateral width is 10 nm and the vertical height 2.5 nm. This particular dot shape is taken from CELFA (Fig. 3.1).

This model indium distribution is shown in Fig. 3.9. Fig. 3.9a shows a cut through the middle of the y-axis, at $y = 40\,\mathrm{nm}$. The inverted-V-shaped region is the wetting layer and the peak the actual dot. A 3D-view is shown in Fig. 3.9b: Isosurfaces of constant indium content show the boundaries of the dot.

Figure 3.10 shows a cross-section of the simulated quantum dot (Scale is the same as in Fig. 3.9b). We can compare that profile with the CELFA data from Fig. 3.7: The simulated dot is intermediate between the limits of low- and high-energy dots. The indium distribution is very similar to the real dots.

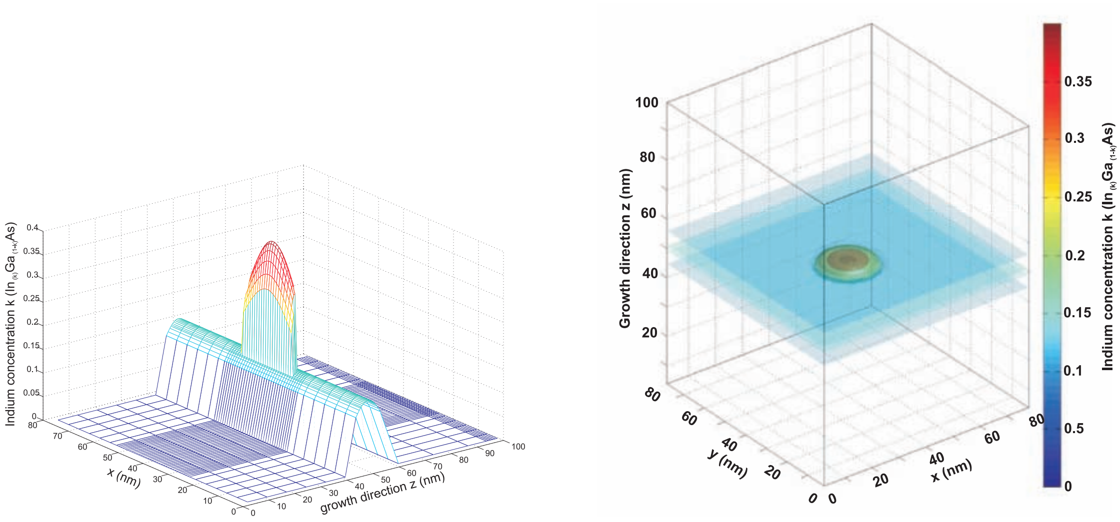

(a) 2D view of the profile

(b) 3D view of surfaces of constant indium content

Figure 3.9: The quantum dots indium distribution was modelled to match the CELFA data. The picture shows the simulation region, a realistic wetting layer is included.

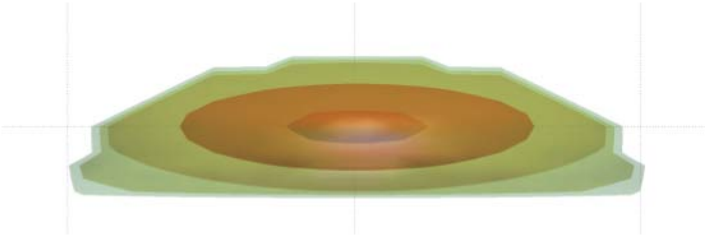

Figure 3.10: Cross-section view of the simulated quantum-dot. The outer diameter (with only 11% indium content) is 20 nm.

Numerical simulation of the band structure and wave functions

To establish the quantum-dot states we use an adapted version of the program nextnano3d [58] to solve the 8-band $\boldsymbol{k} \cdot \boldsymbol{p}$ Schrödinger-Poisson equation. For the calculations, some simplifications had to be assumed, see Chap. 3.2.4 for discussion. The algorithms we have used accounted for the following:

- Band offsets
- Deformation potentials
- Kohn-Sham equations for the electronic exchange correlations
- Minimization of the total elastic strain energy (global minimization)

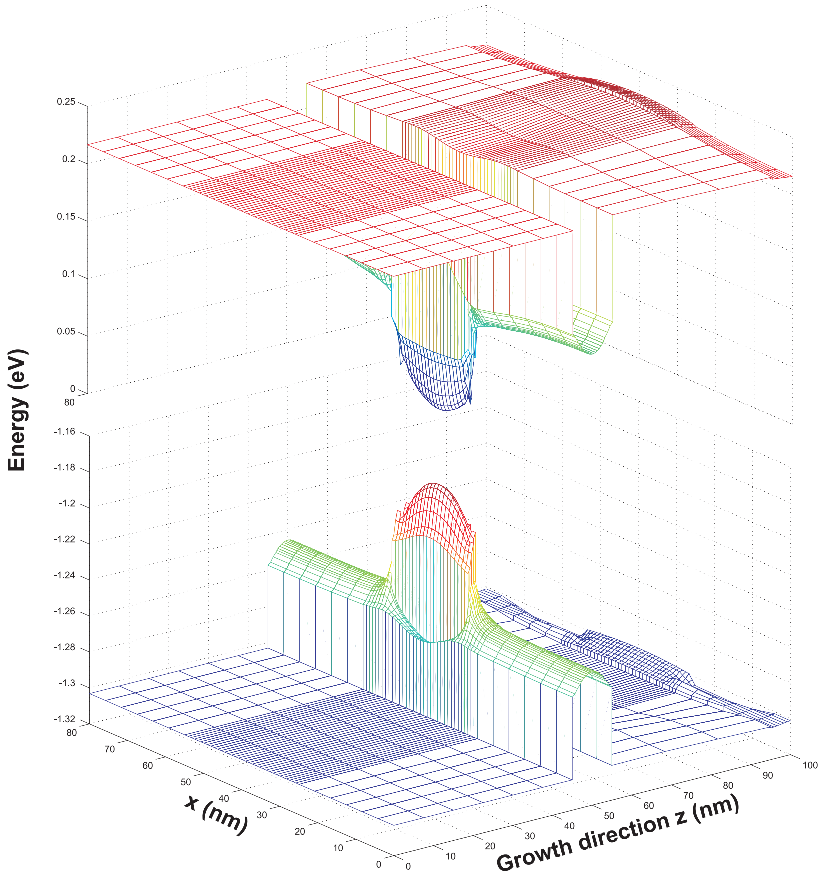

Figure 3.11: Band structure of the simulated quantum dot. The upper part shows the lowest conduction band, the lower part the highest valence band. Shown is a cut at the middle of the y-axis.

- Hartree potentials for the given impurity distribution
- Piezoelectric charges

The resulting spatial band structure is shown in Fig. 3.11. The non-uniformily spaced mesh where the calculations have been conducted is shown. As expected, the potential well is deeper in the conduction band than in the valence band. That leads to stronger confinement of conduction electrons than for holes in the valence band.

Electronic wave functions. The resulting wave functions for the calculated electron states are shown in Fig. 3.12. For each solution shown here there is an additional one for the opposite electron spin. In analogy to the hydrogen atom, we can characterize them:

- (a) is s-like
- (b) and (c) are p-like
- (d) is 2s like

The main difference of the electronic structure of these quantum dots and of a hydrogen atom (apart from the absolute energy values) becomes visible for higher states, starting with Fig. 3.12 (d): The quantum dot potential is far away from spherical symmetry as the confinement along the growth (z) axis is much stronger than in the plane. In these relatively small quantum dots, states with two antinodes in the growth direction are not localized in the dot anymore. This delocalization is also the boundary for the number of bound states in a dot: If the calculated wave function has a huge fraction in the wetting layer, it is not a quantum dot state anymore.

As we were only interested in the first couple of states, we stopped the calculation. Another point is that the accuracy decreases with increasing energy: For higher states, the wavelength gets shorter. To get accurate numerical results, about 10 grid-points per wavelength are needed. For higher states the capacities of the personal computers that were available are quickly exhausted.

Energy eigenvalues. The hole states have also been retrieved from the calculations. To show a full picture of the electronic structure in a quantum dot, the energy eigenvalues for the electrons and holes are shown in Fig. 3.13. Each state here is two-fold spin-degenerate which is omitted in the following. First, we also neglect the small splitting in the p-shell and d-shell. Then, we have a similar grouping of the states as in the hydrogen atom: The s-state is not degenerate and the p-state is 2-fold degenerate. In the hydrogen atom the p-state is 3-fold degenerate ($p_{x,y,z}$ orbitals) but in a quantum dot we have much stronger confinement in growth direction than in-plane. The dots are a quasi-2D system; therefore the p_z state is missing (or at higher energies as explained above). If we compare the splittings Δ_{s-p} and Δ_{p-d}, we find they are nearly equal. The same holds for the valence band states (at least for the lower states). Such an energy spectrum is expected for a particle in a quadratic potential like in a harmonic oscillator. Often the complicated potential in a quantum dot is approximated by a square-well potential in growth direction and a radially symmetric quadratic potential in the plane.

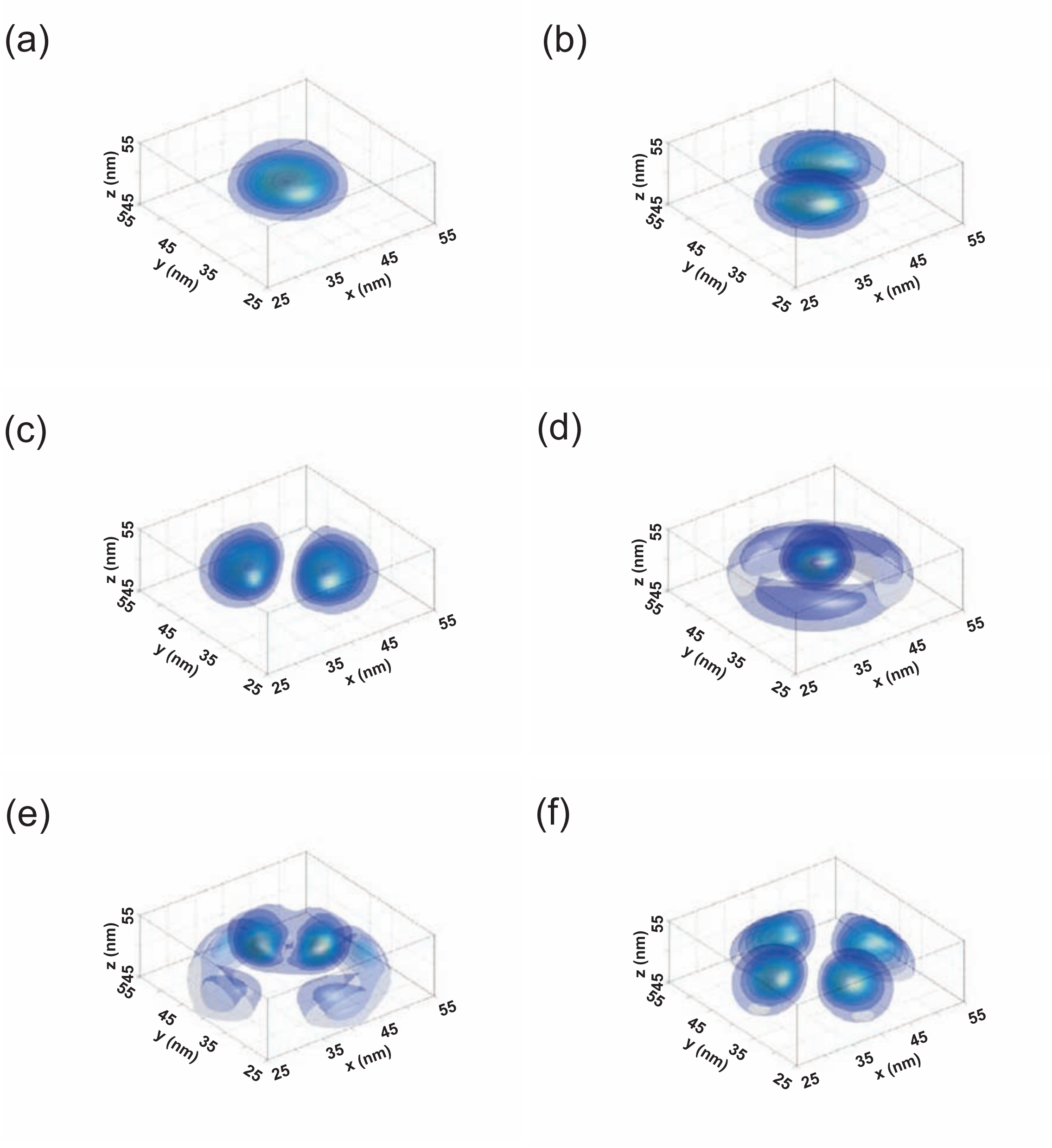

Figure 3.12: The first 6 (or including spin degeneracy 12) bound states for electrons in the simulated quantum dot. The nomenclature of the wave functions in comparison with the hydrogen-atom wave function is described in the main text.

How can the splitting of the p-states be explained? Our simulated quantum dot is perfectly symmetric in the plane. The discretization is good enough that no artifacts are introduced. Even then, there are many effects, which break the in-plane rotational symmetry: The zincblende crystal structure is inversion-asymmetric. Due to strain, the piezo-electric effect deforms the confinement potential [59]. This biaxial strain [60] is the only effect included in our calculations. This is consistent with the symmetry of the wave functions, nearly all states have a symmetry axis along [110] or [1-10] direction. However, there are other effects, which can increase or decrease the anisotropy.

The atomic sizes of In and Ga differ a little. That leads to the formation of a displacement field which directly contributes to the piezo-electric field [61]. Because the interface plane between the dot and the surroundings is not always a reflection plane (in reality never), a lowering of the symmetry is present. An extensive investigation for lens-shaped, pyramidal and annealed quantum dots appeared during preparation of this work in Ref. [62].

Optical transitions. We can now calculate the optical transitions in the dot: Obeying the conservation of angular momentum and parity of the wave functions, the indicated transitions in Fig. 3.13 should be observable in emission (as well as in absorption, Fermi's golden rule holds). However, the higher-energy transitions are very weak under few-carrier conditions. We have to increase the exciting lasers power to fill up the ground states to observe emission from the excited state. Figure 3.14 shows the measurement of a single quantum dot while the excitation power is increased. The peak at 1.3511 eV comes from the ground state and agrees very well with the calculated transition energy of 1.342 eV. The peak appearing at higher excitation power at 1.4021 eV is from p-shell recombination. For this quantum dot, the simulated s-shell – p-shell splitting of 51 meV (see Fig. 3.13) agrees perfectly with the measured value (51.5 meV)! We have to stress that this is a coincidence as should be clear from the broad inhomogeneous size distribution, for example in Fig. 3.15. The solution would be to investigate the same quantum dot in TEM as well as by luminescence which is very challenging.

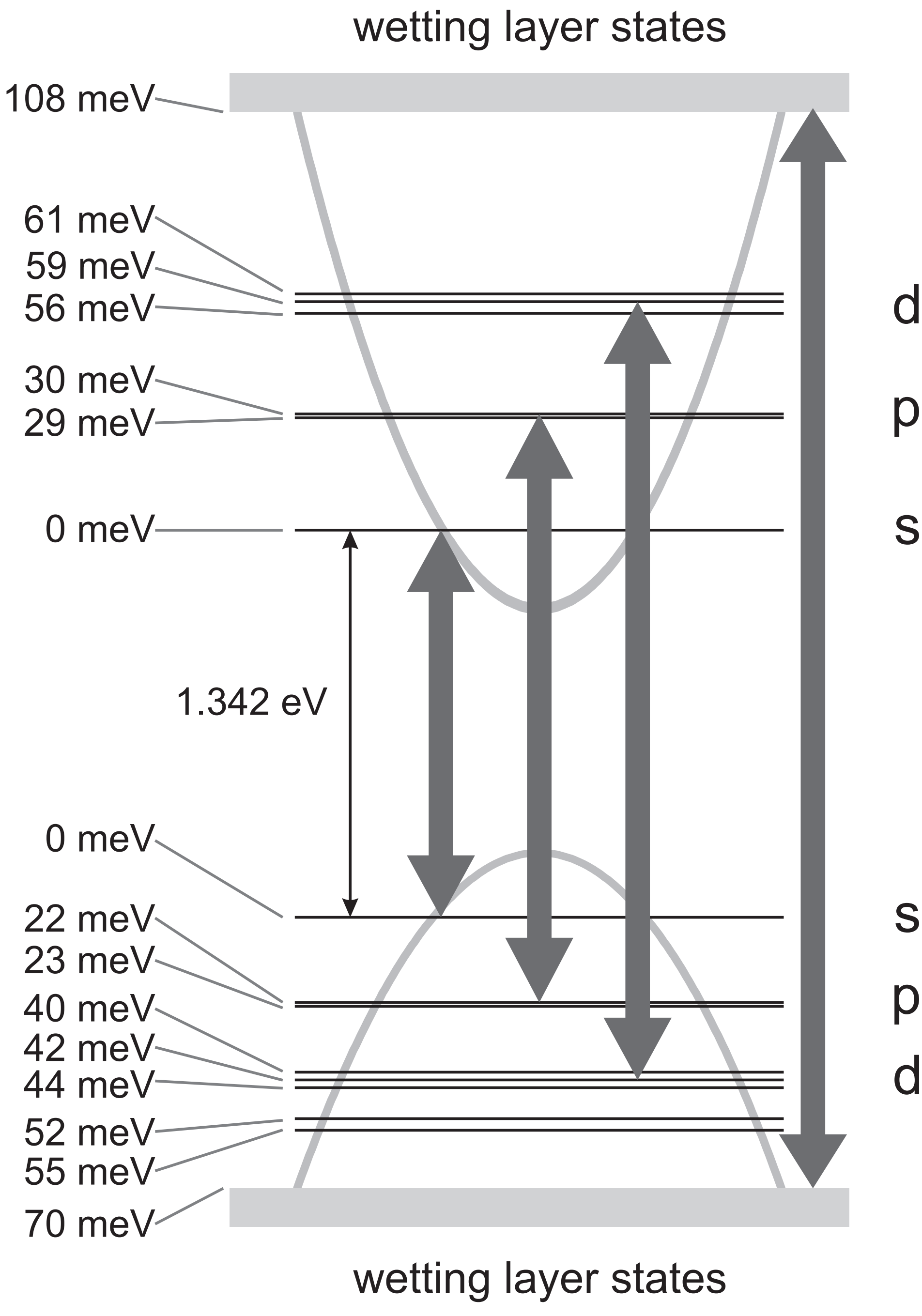

Figure 3.13: Energy eigenvalues for electrons and holes in the quantum dot as obtained from numerical calculations. The arrows indicate the classically-allowed optical transitions. The figure is drawn to scale except the distance of conduction band and valence band.

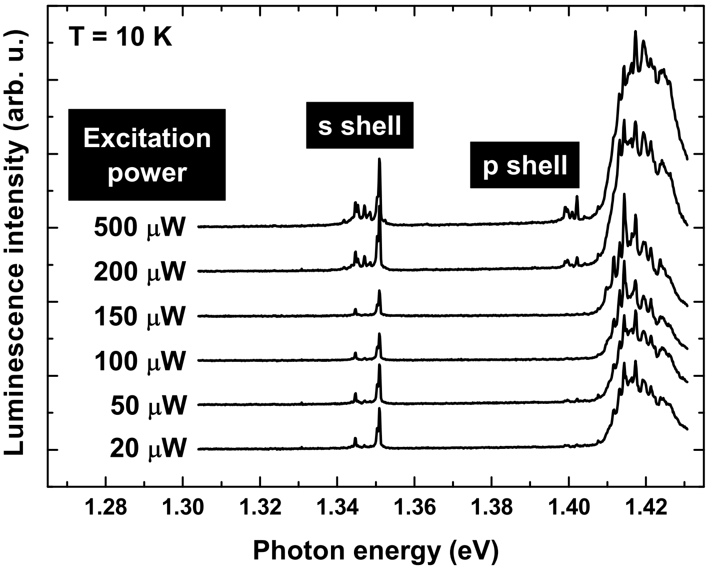

Figure 3.14: By increasing the excitation power, the ground state(s) are filled up and the excited state (p-shell) becomes visible. The peak around 1.42 eV arises from wetting-layer states recombination. The transitions of both shells consists of the exciton (strong peak) as well as from charged and multi-excitonic states.

3.2.3 Single-quantum dot luminescence

To get optical access to a single quantum dot several methods can be applied. The easiest way is to have a very low quantum-dot density so that the spatial resolution of the optical setup is sufficiently high to collect light only from few dots. However, growth parameters cannot be adjusted freely and therefore we have to deal here with sheet densities in the order of $10^{10}\,\mu\mathrm{m}^{-2}$. A photoluminescence spectrum is shown in Fig. 3.15. The quantum-dot emission is centered around 1.3 eV and the strong signal at 1.42 eV originates from recombination in the wetting layer. To access single dots, we can either reduce the quantum-dot area by etching mesas out of the sample (see [63]) or place nano apertures on top to detect only a few dots. The latter is much more favorable since at a high dot density, the mesa area must be very small. That makes further processing (electrical contacts) complicated.

A single gold aperture is shown in Fig. 3.16a. Defined by electron-beam lithography, via gold evaporation and a subsequent lift-off step nanoscale holes are produced in the gold layer on top of the sample. In a micro-photoluminescence setup with diffraction-limited resolution, such a hole can be found easily. In Fig. 3.16b the quantum-dot luminescence of a sample is shown taken through three apertures of different size. We have investigated several samples; for the sake of conciseness we only show results of one typical sample (SQD1). On the right-hand, high-energy side, the wetting layer emission is visible. It shows also discrete lines, which originate from thickness fluctuations. The nearly two-dimensional density of states of the wetting layer results in much higher integrated luminescence intensity. As we reduce the

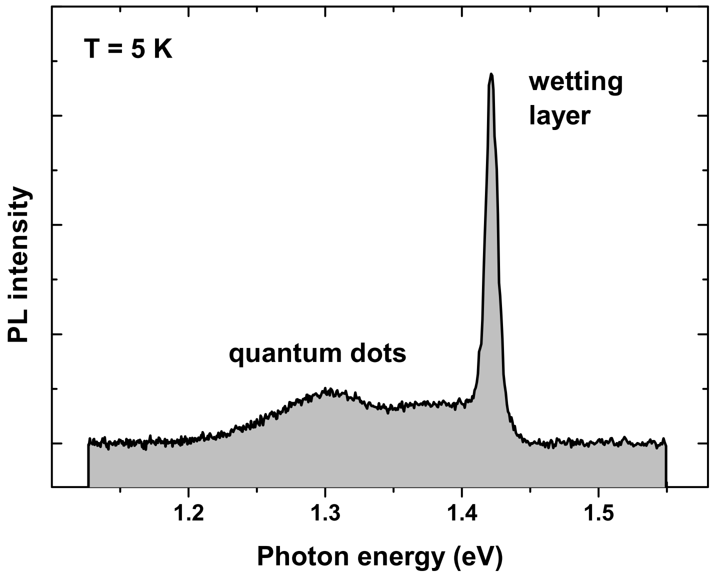

Figure 3.15: Photoluminescence spectrum of a typical quantum-dot sample. The emission of the wetting layer is much stronger than from the quantum dots.

aperture size, less single quantum-dot lines become visible.

In Photoluminescence experiments such a technique is needed to investigate the electronic states and later, the spin dynamics, in single self-assembled quantum dots. For future single dot devices, it will be more favorable to adjust the growth process in a way that single quantum dots will form only at the desired position. That can be done via pre-patterning of the substrate, for example (see Refs. [64, 65]).

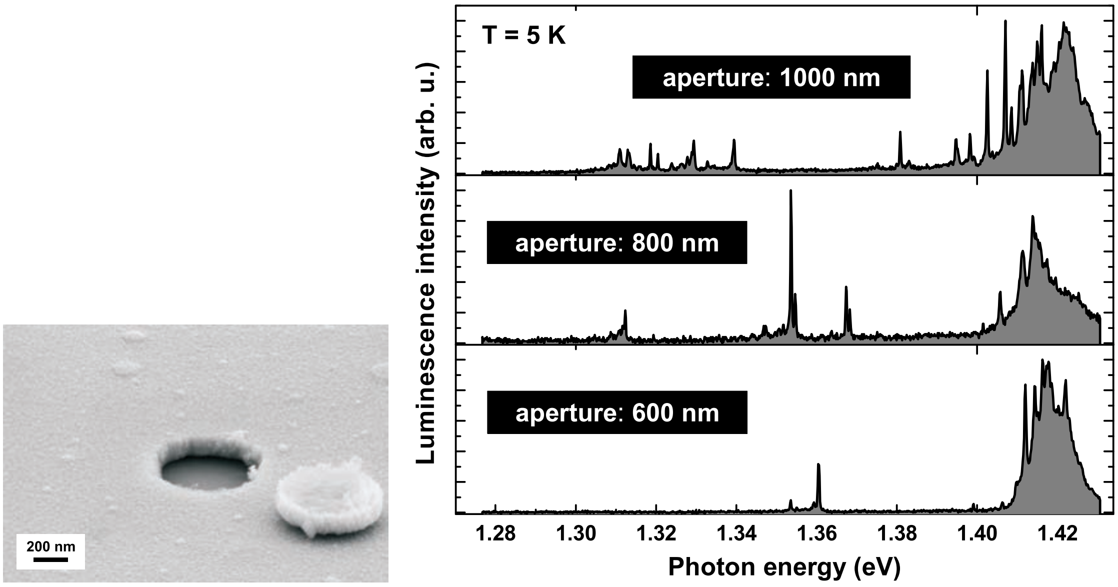

(a) Gold aperture for single-dot experiments

(b) Aperture-size dependent single dot emission

Figure 3.16: Gold apertures of different size are used to narrow the detection area of the luminescence. Using a small aperture, single quantum dots are accessible. In these all-optical photoluminescence experiments, excitation is done through the same aperture as detection.

3.2.4 Charged and multiple excitons in quantum dots

If we add another electron to an exciton in a quantum dot, we change the overall energy level structure due to Coulomb interaction. This fact has not been taken into account in the calculations in Chap. 3.2.2. In fact it is a non-trivial shift in the emission energy, see Ref. [66] for example. The addition of an electron to the X^0 state can result in a red shift or in a blue-shift, depending on the shape and potential depth of the quantum dot.

For the spin-injection LED, we must observe single-exciton states to avoid mechanisms like Pauli-blocking of the ground-state [67]. Here, we excited the quantum-dot sample optically above the GaAs band edge. The excited electron-hole pairs will relax into the wetting layer, then in the quantum dots where they finally recombine. We do also observe luminescence from recombination in the wetting layer if the excitation density is high enough. Then, not enough empty dots are available and due to Pauli blocking, the excess carriers must remain in the wetting layer. At even higher pump intensities GaAs luminescence shows up (not shown here).

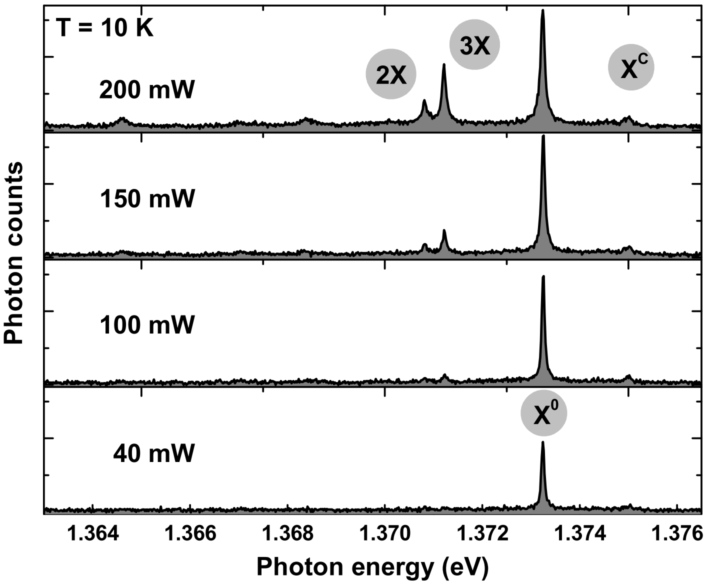

Figure 3.17: High-resolution power-dependent spectra of a single quantum-dot. Additional lines show up if the excitation power is increased.

Figure 3.14 gives an overview of the shell structure. Left to the X^0 emission line, at 1.3511 eV, additional transitions are visible. To investigate this further, experiments with higher (30 µeV) spectral resolution have been done. The power-dependent luminescence under such conditions is shown in Fig. 3.17.

The additional peaks are not visible at the smallest excitation intensities, which gives a hint that many-carrier-effects play a role: If more than one exciton is present in a single dot, the dielectric environment is modified. This means that the recombination of an electron and a hole creates a photon with slightly modified energy. The modification by additional carriers can shift the transition in both directions, as can be seen in Fig. 3.17: Two transitions (labeled 2X and 3X) are red-shifted with respect to the single excitonic transition and the $\mathrm{X^c}$ peak is blue shifted.

To identify which transitions we deal here with, we have conducted excitation-power dependent measurements. Based on a simple rate-equation model, we then can assign a particular transition to the observed peaks in Fig. 3.17.

Similar to Brunner et al. [68], we take a simple 3-level system: Excitons are created by laser excitation into the 2D wetting layer or the 3D bulk material like $N_2 = b\, P_{exc}$ (N_2 is the occupation probability of the wetting layer). They relax into the quantum-dot with a rate Γ where they recombine radiatively with the rate Γ_r. The occupation

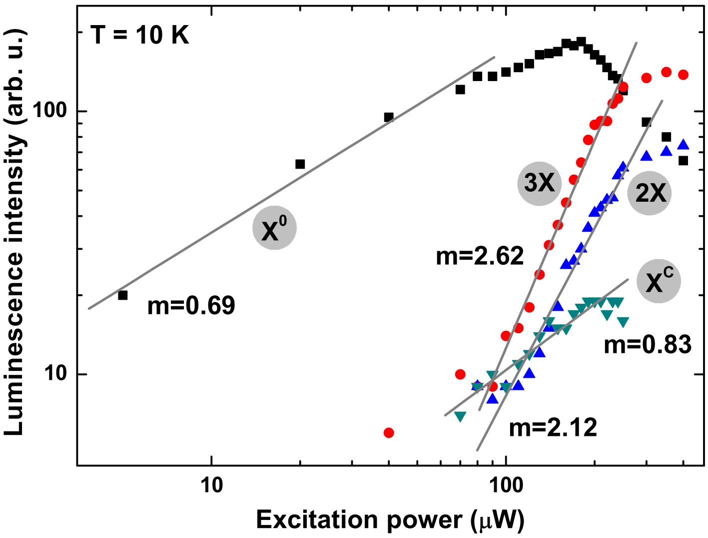

Figure 3.18: Power-dependent intensity of the various quantum-dot transitions of Fig. 3.17. By analyzing the slope and the starting point of each transition the corresponding electronic configuration was assigned.

probability of the quantum dot is N. The solution of that rate-equation model is:

$$\begin{aligned} N &= \frac{N_2\,\Gamma/\Gamma_r}{N_2\Gamma/\Gamma_r + 1} \\ I_X &= 2c\Gamma_r N(1-N) \\ I_{XX} &= 2c\Gamma_r N^2 \end{aligned}$$

I_X is the intensity of the exciton transition and I_{XX} that of the biexciton. b and c are integration constants. We can read off the slope m of the $I(P_{exc})$ function: It is linear or sub-linear for the single-exciton state and quadratic for the biexciton (see also [69, 70, 71]). The intensity of the transitions in Fig. 3.17 is evaluated and plotted in a double-logarithmic plot in Fig. 3.18. The straight lines show linear fits to the experimental data. We do not fit the full rate equation model to the data because we only want to find out if the transition is a single- or multi-excitonic one. Therefore, we have taken into account only the linear region. The saturation at high excitation power is well explained within the model. The other valuable information is the relative intensity where a transition starts to show up in the spectrum: The first transition showing luminescence is nearly exclusively the single exciton X^0 line.

The assignment of the transitions is not always clear. The slope of the X^0 peak (Fig. 3.18) is a little low for the single exciton but the peak shows up already at very low intensities. The peaks labeled 2X and 3X show similar behavior, a clear assignment is not possible. Both could originate from biexcitonic or higher-excitonic recombination. The rate-equation model suggests that the luminescence from multi-excitonic complexes is proportional to N^a where a is the number of electron-hole

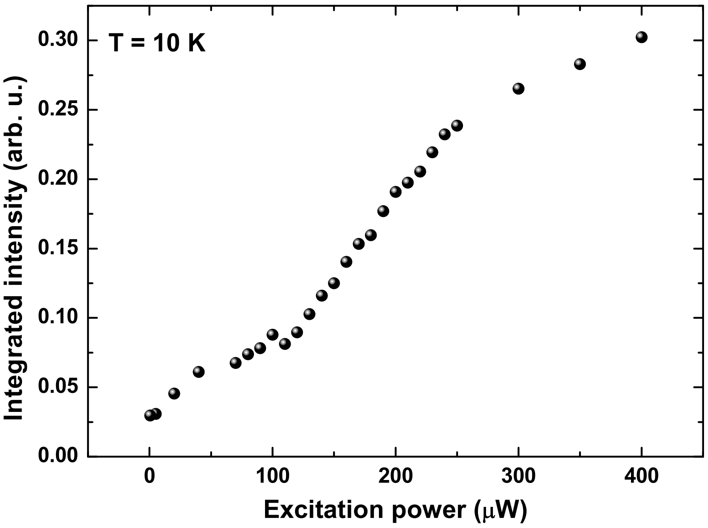

Figure 3.19: Spectrally integrated intensity for the power-dependent measurements. Not captured is the wetting layer emission.

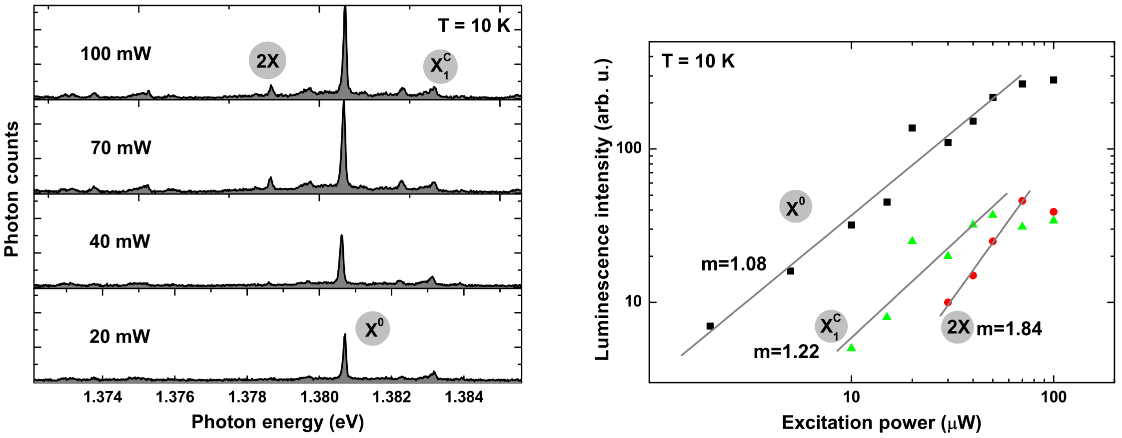

(a) Fine structure of another quantum dot

(b) Power-dependent intensity of quantum-dot transitions

Figure 3.20: Multi-carrier states in another quantum dot. In the left panel, the single-dot luminescence is shown; the peaks have already been assigned to transitions. Again, the foundation of this assignment is obtained from the power-dependent intensity behavior of the single peaks (right panel).

pairs in the dot. The X^c-peak shows a slope as expected for a charged exciton and shows up only at higher intensity. As these measurements were done in a micro-photoluminescence setup, the laser power could have altered by mechanical drifts. Therefore, Fig. 3.19 shows the over-all integrated luminescence intensity. As expected, it shows in good approximation a linear increase with excitation power.

Another example for dot charging is shown in Fig. 3.20. In this case, the biexciton could be identified more clearly than in the previous case: The peak from single-exciton recombination is that which is visible at lowest power and has a slope close to one. The biexciton (2X) intensity increases with the square of the number of carriers; charged excitons have a slope close to 1. The discrimination of charged exciton and biexciton recombination can be supported by the peak energy: Due to Coulomb interaction the addition of a single carrier to an exciton leads to elevated energy while the biexciton is lowered by the biexciton binding-energy with respect to the exciton transition energy.

3.3 Advanced topics on quantum dot properties

In the previous chapters, we have shown basic properties of the quantum dots side-by-side with optical characterization. Here we will address some more complex topics of high importance for quantum information processing with self-assembled semiconductor quantum dots. We omit here the investigation of energy relaxation processes of the carriers. This topic being linked tightly to the electron injection method we will discuss in the next chapter within the context of electrical spin injection.

3.3.1 Optical recombination and selection rules

Radiative recombination in a semiconductor means transition of an electron from the conduction band to an empty state in the valence band by emission of a photon. The transition rate $W_{i\rightarrow f}$ from initial state $|i\rangle$ to final state $|f\rangle$ must be calculated using Fermi's golden rule (see, e.g., [72]:

$$W_{i\rightarrow f} = \frac{2\pi}{\hbar}\langle f|H_I|i\rangle\rho_f$$

Where H_I is the interaction Hamiltonian and ρ_f is the density of states of the final state. We consider dipole interactions here, so H_I is given by:

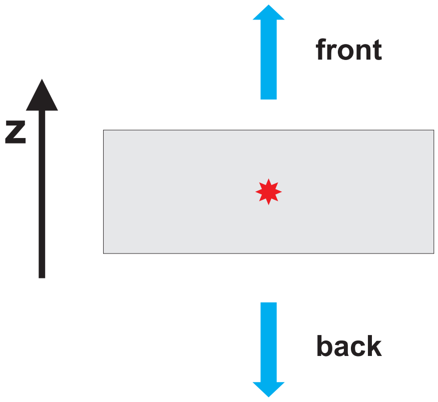

$$H_I = \boldsymbol{\mu}\cdot\boldsymbol{E} = \mu_x E_x + \mu_y E_y + \mu_z E_z$$

$\boldsymbol{\mu}$ is the dipole moment of the carriers and $\boldsymbol{E}$ is the electric field vector of the light field (which can be assumed to be constant over the dimensions of the quantum dot).

The electronic states can be described with Bloch functions. Their orbital shape is very similar to wave functions describing atomic orbitals [18]. The relevant states are shown here in the $|J, m_j\rangle$ notation; on the right is the orbital wave function:

$$\begin{aligned}
\left|\frac{1}{2}, -\frac{1}{2}\right\rangle_{CB} &= |s\downarrow\rangle \\
\left|\frac{1}{2}, +\frac{1}{2}\right\rangle_{CB} &= |s\uparrow\rangle \\
\left|\frac{3}{2}, -\frac{3}{2}\right\rangle_{VB} &= +\frac{1}{\sqrt{2}}\left(|p_x\downarrow\rangle - i|p_y\downarrow\rangle\right) \\
\left|\frac{3}{2}, +\frac{3}{2}\right\rangle_{VB} &= -\frac{1}{\sqrt{2}}\left(|p_x\uparrow\rangle + i|p_y\uparrow\rangle\right) \\
\left|\frac{3}{2}, -\frac{1}{2}\right\rangle_{VB} &= +\frac{1}{\sqrt{6}}\left(|p_x\uparrow\rangle - i|p_y\uparrow\rangle\right) + 2|p_z\downarrow\rangle \\
\left|\frac{3}{2}, +\frac{1}{2}\right\rangle_{VB} &= -\frac{1}{\sqrt{6}}\left(|p_x\downarrow\rangle + i|p_y\downarrow\rangle\right) - 2|p_z\uparrow\rangle
\end{aligned}$$

The first two are electronic conduction-band states, the next two heavy-hole valence band states and the last pair the $L = 0$ light-hole states. The split-off valence-band states with $L = 0$

$$\left|\frac{1}{2}, +\frac{1}{2}\right\rangle_{VB} \quad \text{and} \quad \left|\frac{1}{2}, -\frac{1}{2}\right\rangle_{VB}$$

are neglected here because the spin-orbit splitting of about 400 meV is much larger than the potential depth in the dot. This is only valid for quantum dot ground states as emphasized before. If states with finite orbital quantum number are taken into account, a new state classification scheme must be applied [73]. If L_{qd} is the angular momentum of the wave function of the confinement problem and J the shown-above angular momentum from the Bloch functions, the total angular momentum is

$$F = L_{qd} + J$$

If we restrict ourselves to the ground states, the allowed transitions can easily be obtained using the Wigner-Eckart theorem as known from atomic physics. The dipole moment $\boldsymbol{\mu}$ is expressed as a spherical tensor $\mu^1_{\pm 1}$ for the circularly polarized optical transitions. Then, $\Delta m = \pm 1$ follows directly. Due to symmetry, the only non-zero interband matrix elements are

$$\langle p_i|\mu_i|s\rangle \neq 0 \quad \text{with} \quad i = x, y, z$$

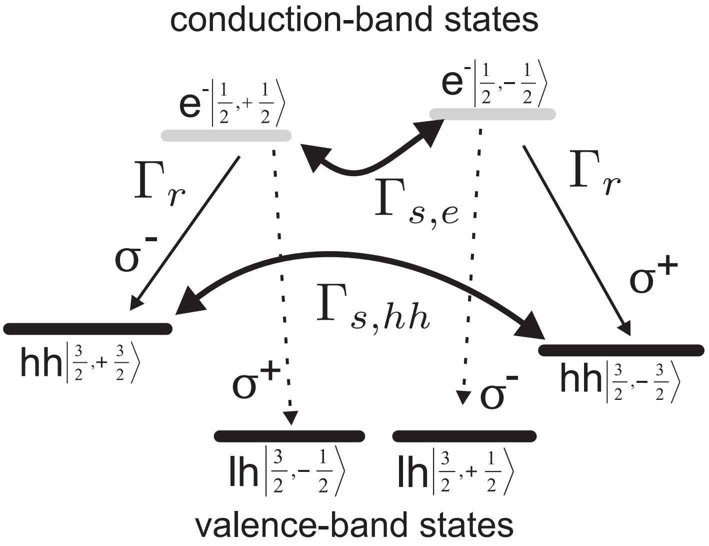

Figure 3.21: The optical selection rules in (small) InAs quantum dots in an external magnetic field.

Figure 3.21 shows the allowed transitions and the optical polarizations. The light-hole transitions are also shown, due to efficient energy relaxation the states are not populated at low temperatures.

It should be noted that the macroscopic radial symmetry (if there is any) is broken microscopically (due to the crystal structure) and the light-hole and heavy-hole states are mixed. Many-body effects [74] break that symmetry, too. One consequence is that excitonic transitions with $\Delta N \neq 0$ become allowed.

The polarization of quantum-dot ground-state emission is a direct measure for the spin of the electron. This allows for easy optical read-out.

One note about the sign of helicity: A photon has a helicity of ±1 with respect to its direction of motion. We always consider the B-field parallel to the z-axis. Let us consider a photon having an angular momentum $J_{Ph} = +1$ along $+z$. The polarization of the light is considered as $\sigma+$ only if it is propagating in positive z direction, if it is emitted to the back ($-z$), it is called $\sigma-$ polarized.

Non-normal emission. The external magnetic field determines the spin-quantization axis for the Zeeman-split spin states of the carriers. Only for this direction, the selection rules for optical transitions hold exactly. This fact is neglected in literature quite often. For a photon emitted under angle Θ_e with respect to the quantization axis, the polarization $P(\Theta_e)$ is related to the polarization of normal emitted photons $P(0)$ by

$$P(\Theta_e) = P(0) \cdot \cos(\Theta_e)$$

A more detailed discussion of this issue is given in Pryor et al. [75]. Due to refraction at the interface sample – vacuum, the relevant angle is not the angle under which the photon is detected. At any interface, we have to consider the Fresnel equations. Due to different transmission coefficients for s- and p-polarized light, the polarization of light is altered. That translates to a change of polarization:

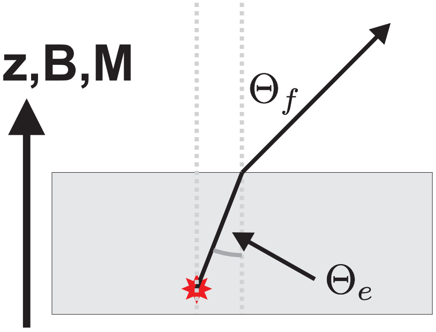

Figure 3.22: Geometry for non-normal emission from a quantum dot.

$$P_{det} = \frac{2\cos(\Theta_e - \Theta_f)}{\cos^2(\Theta_e - \Theta_f) + 1} \cdot P(\Theta_e)$$

The semiconductor material here is GaAs with a relatively high refractive index of $n_{GaAs} = 3.4$. If a photon in $\sigma+$ or $\sigma-$ circularly polarized states is generated and detected at $\Theta_f = 45\,°$ with respect to the surface normal in vacuum, it was emitted at an angle of 12 °. If the initial polarization was perfectly circular ($P(0) = 1.0$), the detected polarization is $P_{det} = 0.96$.

In a real measurement, the analysis is more complicated. First, we have to integrate over a certain solid angle corresponding to the numerical aperture of the imaging optics. Additionally, similar calculations as above have to be done at each glass-vacuum interface of the imaging optics. Because the exact beam path is complex (and mostly unknown) for microscope objectives, we can only keep in mind that the initial photon polarization is higher than the detected one!

In single quantum-dot experiments the $\sigma+$ and $\sigma-$ polarized photons also have different energy due to Zeeman splitting. Then we can deduce the initial electron polarization via the occupation of the corresponding Zeeman level and neglect optical polarization.

InAs quantum dots. In wide GaAs/AlGaAs quantum wells, the heavy-hole and light-hole valence bands are degenerate (at the Gamma-point). In InAs quantum dots, due to confinement and strain, the heavy- and light hole degeneracy is lifted. That can easily be understood as the effective masses are different and the confinement energy depends on the mass of the particle. In an infinite square-well potential, the energy is given by

$$E_n = \frac{\hbar^2 \pi^2}{2m\, L^2} \cdot n^2$$

In flat InAs quantum dots, the splitting between light- and heavy hole states is of the order of 100 meV [60].As our experiments are conducted at temperatures below 100 K (corresponding to 8 meV), the light holes do not take part in recombination. Therefore, the photon polarization directly resembles the electron spin polarization and is usually given in terms of the circular polarization degree:

$$CPD = \frac{n_\uparrow - n_\downarrow}{n_\uparrow + n_\downarrow} = \frac{I_{\sigma+} - I_{\sigma-}}{I_{\sigma+} + I_{\sigma-}}$$

Where $n_{\uparrow\downarrow}$ are the averaged numbers of electrons in the conduction band ground state with spin up and spin down. In experiments, one usually measures the intensities of the circularly polarized emission $I_{\sigma\pm}$.

3.3.2 Many-carrier effects

If the quantum dot is pumped with high excitation density we also see luminescence from p-shell recombination (Fig. 3.14). As such a process cannot be excluded completely we discuss its impact on the storage of a single electron spin. The electronic ground-state level in a quantum dot has no orbital angular momentum. Therefore, two electrons can only occupy it if their spin is opposite.

The subsequent addition of two spin-polarized electrons to a quantum-dot is shown in Fig. 3.23. The first spin-polarized electron in the ground state of the dot (left) blocks that state for another electron with the same spin orientation. The second electron must stay in the p-shell (middle). Spin-orbit coupling is an efficient spin-flip mechanism in the p-shell ($L = 1$). If the second electron flips its spin, it can relax

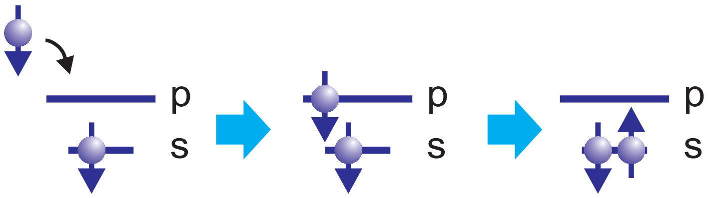

Figure 3.23: First, the dot is initialized with a spin-polarized electron. For an additional electron, Pauli-blocking forbids occupation of the same state. But after a spin flip it can directly relax to the ground-state.

to the ground state. The relaxation from the p-shell into the ground state is fast in InAs dots because the LO phonon energy (GaAs: $\hbar\omega_{LO} = 36\,\text{meV}$) is of the same order as the level splitting.

If we inject an additional hole for read-out, the polarization of the photon is not well defined because recombination can take place with both of the two electrons. At even higher electron density a third electron can be injected into the dot. This electron can remain spin-polarized in the p-shell. Comparing the emission from the s-shell (with two electrons with opposite spin) and from the p-shell (only one spin-polarized electron), emission from the p-shell is higher polarized! In all-optical experiments, this has been observed, see Kalevich et al. [67]. This many-electron regime must be avoided for efficient electron spin storage.

3.3.3 The single electron spin as a qubit

Let us return to the single electron in a quantum dot. The Zeeman doublet of spin-up and spin-down states is a well-isolated quantum-mechanical two-level system. Such a system can be used as the building block for quantum information processing, the qubit [76]. Also in other approaches the spin is used as the qubit: in nuclear magnetic resonance techniques the nuclear spin, the electron spin in GaAs quantum dots (2DEG), molecular spin arrays, and the electron and nuclear spin at nitrogen-vacancy centers in diamond. Therefore the spin of a single electron in a self-assembled InAs quantum dot is a promising candidate for a qubit, too [7, 19, 77]. Here, we only want to outline the basic ideas, which make that field so interesting. The physical fundamentals are well known but the (theoretical) application of quantum systems to information science came first up with Richard Feynman and David Deutsch in the 1980s.

The qubit is defined in its Hilbert space $\mathcal{H}$ spanned by the basis vectors $|0\rangle$ and $|1\rangle$. In contrast to classical bits, which can take either the value 0 or 1, the qubit can be put into superposition of the two basis states:

$$|\Psi\rangle = \alpha_0|0\rangle + \alpha_1|1\rangle \quad \text{with} \quad \sum_i |\alpha_i|^2 = 1$$

As the coefficients α_i are complex numbers, the state vector Ψ can be described on a Bloch sphere, see the Fig. 3.24.

The combination of qubits (the so-called quantum register) is created by taking the tensor product of the states:

$$|u\rangle_A \otimes |v\rangle_B \in H_A \otimes H_B \equiv |u\rangle|v\rangle \equiv |uv\rangle$$

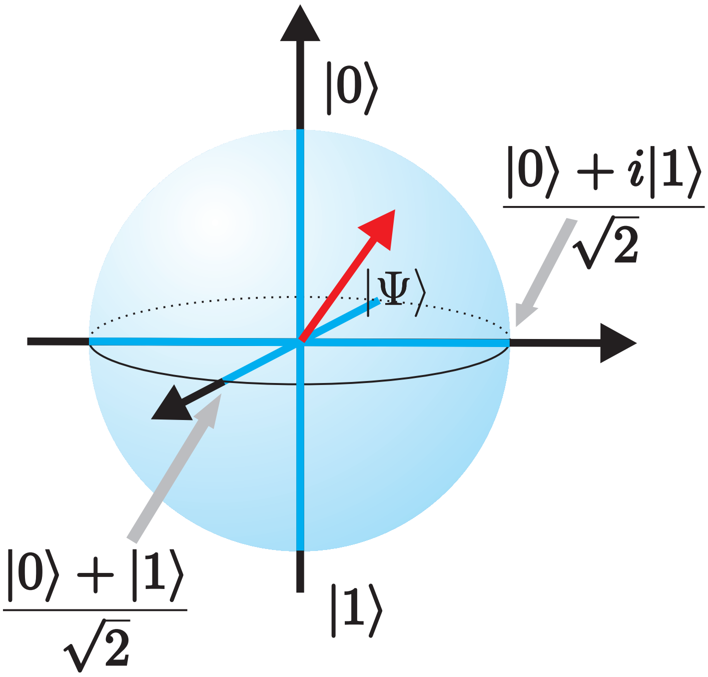

Figure 3.24: The Bloch sphere for a single electron spin. The direction of the axis between the poles is determined by the magnetic field.

Following the binary notation, we can write a 3-qubit state as follows:

$$|1\rangle \otimes |0\rangle \otimes |1\rangle \equiv |101\rangle \equiv |5\rangle$$

If we put three qubits independently into superposition, we get:

$$(\alpha_0|0\rangle + \alpha_1|1\rangle) \otimes (\alpha_2|0\rangle + \alpha_3|1\rangle) \otimes (\alpha_4|0\rangle + \alpha_5|1\rangle)$$

$$\equiv c_0|000\rangle + c_1|001\rangle + c_2|010\rangle + c_3|011\rangle + c_4|100\rangle + c_5|101\rangle + c_6|110\rangle + c_7|111\rangle$$

$$\equiv \sum_{n=0}^{2^N} c_n|n\rangle \quad \text{with} \quad \sum_i |c_i|^2 = 1\,, c_i \in \mathbb{C}$$

Thus, to fully describe a N qubit system we need 2^{N+1} real numbers, which is in stark contrast to a classical boolean register.

This, however, would be classical computing with an extremely large computer. The key to quantum computation lies within the temporal evolution of the quantum state, the evolution of superposition. This is also called “quantum parallelism”.

The time evolution of a single state is obtained via an unitary operator $\mathcal{U}$:

$$|\Psi(t)\rangle = \mathcal{U}(t)|\Psi(0)\rangle \text{ with } \mathcal{U}(t) = e^{-\frac{i}{\hbar}dtH(t)}$$

If we have an operator that transforms the basis states like

$$|0\rangle \to |f(0)\rangle \ \ , \ |1\rangle \to |f(1)\rangle,$$

then a superposition is evaluated like

$$\frac{|0\rangle + |1\rangle}{\sqrt{2}} \to \frac{|f(0)\rangle + |f(1)\rangle}{\sqrt{2}}.$$

In a single step of using the operator, two results are obtained! It is clear that not both results can be used for further classical evaluation, but there are algorithms, which make use of it and outperform all known classical algorithms.

The main problem of using electron spins in self-assembled semiconductor quantum dots is the interaction with the environment, decoherence. Therefore, very strong limits are put to the fidelity of the initial states (and, for sure, to the operations). If these conditions are not met, the error rate is larger than the rate of successful calculation. In Chap. 4 we will come to the main results of this work, the electrical preparation of such high fidelity electronic spin states in quantum dots.

Biexcitons and entangled photons for quantum cryptography. For our purposes, quantum computation, we must avoid situations where any charged exciton or biexciton is in the dot. However, much effort has been taken in very recent time to achieve controlled biexciton recombination for production of polarization-entangled photon pairs [78, 79, 80]. That is the building block of novel quantum-cryptography methods. They make use of the decoherence problem mentioned above: Any interaction with environment (eavesdropping) can easily be detected in a quantum state.

For these purposes, two polarization-entangled photons are needed. The biexciton decay can provide such pairs as shown in Fig. 3.25.

We start with a dot occupied by two electrons and two holes, both in the ground state where they exist as a Coulomb-correlated biexciton. The first electron that recombines with a hole emits a photon either $\sigma-$ or $\sigma+$ circularly polarized. As both electrons are in the ground state, they must have antiparallel spin. Therefore, the second (single excitonic) recombination leads to an opposite-circularly-polarized photon. The energy of the first photon is different from that of the second due to Coulomb correlations[3]. As long as no which-path information is collected, both photons are polarization entangled in the Bell-state:

$$\frac{1}{\sqrt{2}} \left(|R_{XX} L_X\rangle + |L_{XX} R_X\rangle \right).$$

---

[3] The strength and sign of biexciton binding energy depends on the dot morphology, see [81]

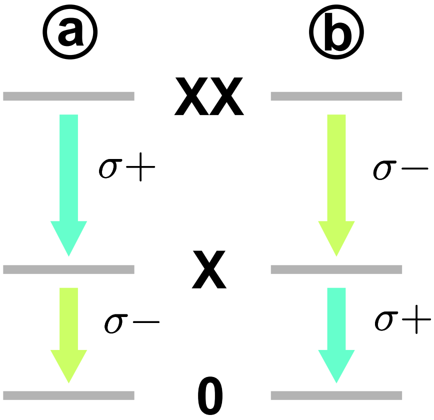

Figure 3.25: Generation of two polarization-entangled photons via the biexciton cascade. Path **a** and path **b** are indistinguishable which leads to entanglement as explained in the text.

Noteworthy is: The photons have different energy and can easily be separated with a dichroic mirror! In most other approaches (like parametric down-conversion), both photons have the same energy.

The main problem during that quantum-dot based generation is that the two paths must be completely indistinguishable. Quantum dots that break the (lateral) radial symmetry by a different shape or strain are no candidates for that. Such an asymmetry leads to the fine structure splitting and without external magnetic field; the ground-state of the quantum-dot creates linearly polarized photons. We also did experiments to determine the fine structure splitting in our samples because an asymmetry contributes to spin-relaxation.

3.3.4 Shape asymmetry in quantum dots

The possible combinations of electron and hole spin leads to a multiplet of states, which can be split energetically (fine structure splitting). Two main contributions exist: The Zeeman splitting due to interaction of the angular momentum with an external or internal magnetic field, and the splitting due to exchange interaction of the electron and hole spin. The lateral shape of the quantum dot heavily influences both contributions. The excitonic fine structure [82] originates from the exchange energy which can be described by the excitonic wave function $\Psi_X(r_e, r_h)$, where r_e and r_h are the position of the electron and hole, respectively [83]:

$$E_{Exch.} \propto \int d^3r_1\, d^3r_2\, \Psi_X(r_1, r_2) \times \frac{1}{|r_1 - r_2|} \Psi_X(r_2, r_1)$$

From a crystallographic point of view it is obvious that one distinguishes two regimes: A short-range part where both carriers are in the same Wigner-Seitz cell and a long-range part where both are farther apart. The short-range part splits the excitonic multiplet into optically dark and bright excitons. The shape of the dot contributes mainly to the long-range interaction and splits the bright excitonic states. A magnetic field extends the fine structure via the Zeeman term and the Overhauser shift [84, 85]. The latter can lead to effective magnetic fields of up to 2 T.

A quantum dot which shows perfect in-plane radial symmetry belongs to the D_{2d} symmetry group. This symmetry can be disturbed by an asymmetry of the composition which leads to asymmetric confinement. Additionally, strain in the crystal and electric crystal fields lower the radial symmetry. As the read-out here is done optically, we will constrain ourselves here to the optically active $M = \pm 1$ states. For a quantum dot with D_{2d} symmetry, the states have the following energies (as usual in Faraday geometry):

Table 3.2: Dot states for D_{2d} symmetry.

State	**Energy**
$\vert +1\rangle$	$+\frac{1}{2}\Delta_0 + \frac{1}{2}\mu_B(g_{e,z} + g_{h,z})B_z$
$\vert -1\rangle$	$+\frac{1}{2}\Delta_0 - \frac{1}{2}\mu_B(g_{e,z} + g_{h,z})B_z$

Where the state is given in the $|M_z\rangle$ notation: $|-1\rangle \equiv |+\frac{1}{2}, -\frac{3}{2}\rangle$ and $|+1\rangle \equiv |-\frac{1}{2}, +\frac{3}{2}\rangle$. Δ_0 is the singlet-triplet splitting energy which splits the $|M| = 1$ and $|M| = 2$ states. It has contributions from short-range as well as long-range exchange splitting. The B_z dependent part is the Zeeman splitting where electron- and hole Landé g-factors contribute. The energy splitting of the two basis states increases linearly with the magnetic field, see Fig. 3.26a. In all these considerations we have substracted the diamagnetic shift. It is proportional to B^2 and leads to a common offset for both spin states.

For dots with reduced symmetry ($< D_{2d}$), the basis states need to be redifined due to different exchange energies in the dot plane with respect to the asymmetry axes. In analogy to [83], we define $\beta_1 = \mu_B(g_{e,z} + g_{h,z})B_z$ for the magnetic part and the parameter $\delta_1 = 0.75(b_x - b_y)$ for the deviation from circular symmetry. The diameter in lateral x and y direction is b_x and b_y, respectively.

The plot of the energies in Fig. 3.26b shows two regimes: at low fields, the basis states are linear combinations of the angular-momentum eigenstates $M = \pm 1$. Their energy increases quadratically with the magnetic field. If the Zeeman energy β_1 gets much larger than the fine structure splitting energy δ_1, the behavior gets similar to the symmetrical case in Fig. 3.26a.

Table 3.3: Dot states for $< D_{2d}$ symmetry.

State	Energy
$\lvert L_1\rangle \propto \lvert +1\rangle + \left(\frac{\beta_1}{\delta_1} + \sqrt{1+\frac{\beta_1^2}{\delta_1^2}}\right)\lvert -1\rangle$	$+\frac{1}{2}\Delta_0 + \frac{1}{2}\sqrt{\beta_1^2+\delta_1^2}$
$\lvert L_2\rangle \propto \lvert +1\rangle + \left(\frac{\beta_1}{\delta_1} - \sqrt{1+\frac{\beta_1^2}{\delta_1^2}}\right)\lvert -1\rangle$	$+\frac{1}{2}\Delta_0 - \frac{1}{2}\sqrt{\beta_1^2+\delta_1^2}$

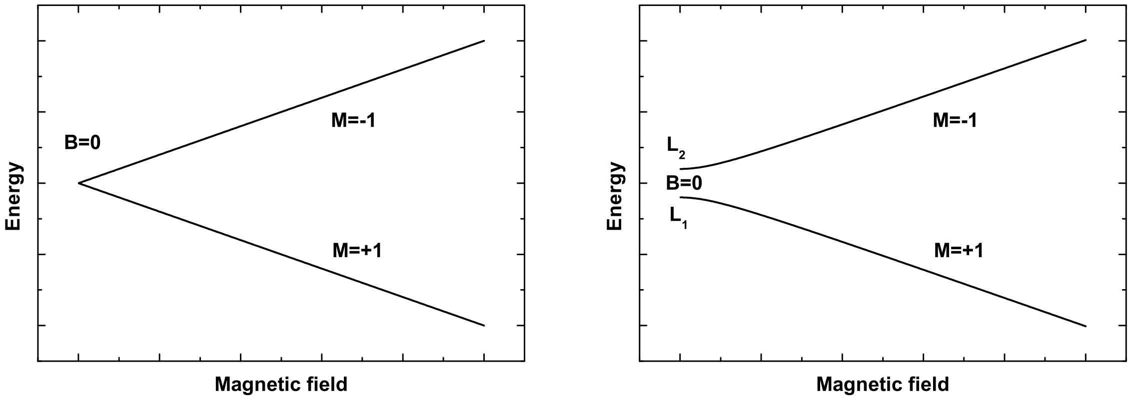

(a) Dot with perfect D_{2d} symmetry (b) Quantum dot with reduced symmetry

Figure 3.26: Magnetic-field dependency of a symmetric and an asymmetric quantum dot. The symmetric dot shows only linear Zeeman splitting while the asymmetric dot has already split states at zero magnetic field. For higher field, the Zeeman energy outperforms the fine structure splitting and angular-momentum eigenstates are restored.

We have optimized the quantum-dot growth to get dots with high indium content. Additionally, the dots are relatively thin in growth direction. That combination seems to lead to dots with very high symmetry. We conducted experiments where the photons from the dot are selected for linear polarizations and recorded with 35 µeV spectral resolution. We could not find any splitting in the absence of an external magnetic field! Apparently, the optimal symmetry is met with high accuracy.

3.3.5 Spin relaxation and decoherence

Up to now, we only discussed static properties of carriers in quantum dots and their interaction with photons. For spintronics in general the incoherent dynamics of the spin of carriers is of interest. For quantum information processing using the electron spin as qubit, spin decoherence (or dephasing) is the main limiting factor and is subject of many investigations.

The incoherent part of spin relaxation is the relaxation between the two spin states, spin up, and spin down. It's relaxation time is called longitudinal relaxation time T_1. The coherent part is termed transverse relaxation time T_2 and is responsible for the loss of coherence of a state in superposition.

In nuclear spin systems, there is a "bottleneck" for energy relaxation. T_1 can therefore be several orders of magnitude higher than T_2. This bottleneck does not exist for electrons in bulk or quantum well semiconductors: Interaction with phonons and/or changing the momentum of the electron makes energy dissipation easy. The natural solution to avoid fast spin relaxation in semiconductors is to use discrete systems like quantum dots.

To describe electron spin dynamics in semiconductor quantum dots large parts can be borrowed from NMR (nuclear magnetic resonance) and ESR (electron spin resonance) experiments. The electron spin is isolated, similar to the nuclear spin in NMR. The g-factor (and therefore the Larmor frequency, too) is much larger than in NMR, more like in ESR. However, one can usually neglect spin-spin interactions, which are important in ESR. As the g-factor strongly fluctuates in the quantum dot ensemble, standard continuous-wave ESR techniques are not applicable. This point is compensated for very well by the possibility to couple electrons to photons in semiconductor quantum dots!

The quantum-mechanical spin system can be described by the Bloch equation for the magnetization $\boldsymbol{M}(t)$:

$$\frac{\partial \boldsymbol{M}}{\partial t} = g_e \mu_B \boldsymbol{B} \times \boldsymbol{M} - \frac{1}{T_1}\boldsymbol{M}_{\parallel} - \frac{1}{T_2}\boldsymbol{M}_{\perp}$$

The first term gives us the Larmor precession around the external magnetic field. The second results in spin relaxation of the component of $\boldsymbol{M}$ parallel to $\boldsymbol{B}$, the third describes decoherence. Both relaxation contributions are introduced phenomenologically because a more profound way needs to include interaction of the spin with the environment, which is beyond the scope of this work.

Obviously, the parallel and transverse magnetization (spin polarization) decay exponentially:

$$\boldsymbol{M}_{\parallel} \propto e^{-t/T_1} \quad \text{and} \quad \boldsymbol{M}_{\perp} \propto e^{-t/T_2}$$

Density matrix. The density matrix formalism allows for easy separation of occupation and coherences of a quantum state. The density matrix for the state

$$|\Psi\rangle = \alpha_0|0\rangle + \alpha_1|1\rangle$$

is given by

$$\rho = \begin{pmatrix} |\alpha_0|^2 & \alpha_0\alpha_1^* \\ \alpha_0^*\alpha_1 & |\alpha_1|^2 \end{pmatrix} \tag{3.1}$$

The diagonal terms describe the occupation of the two states, the off-diagonal terms the coherences. Because the density matrix must be hermitian ($\rho^\dagger = \rho$), only 3 real values are needed to fully define it. The same information is also contained in the Bloch vector $\boldsymbol{\nu}$: In cartesian representation (ν_x, ν_y, ν_z) or (Θ, ϕ, $|\boldsymbol{\nu}|$) in spherical coordinates.

In the density matrix formalism, it is easy to write down the effect of relaxation and decoherence:

$$\begin{pmatrix} |\alpha_0|^2 & \alpha_0\alpha_1^* \\ \alpha_0^*\alpha_1 & |\alpha_1|^2 \end{pmatrix} \xrightarrow{T_2} \begin{pmatrix} |\alpha_0|^2 & 0 \\ 0 & |\alpha_1|^2 \end{pmatrix} \xrightarrow{T_1} \begin{pmatrix} \rho_\uparrow & 0 \\ 0 & \rho_\downarrow \end{pmatrix}$$

$\rho_\updownarrow$ are the thermal equilibrium probabilities of finding spin-up or down state which is given by the energy splitting. Decoherence leads to loss of phase information (coherences) and therefore limits the lifetime of the qubit.

Ensembles. If one investigates at the same time an ensemble of electron spins we have to exchange the single-particle decoherence time T_2 with the ensemble dephasing time T_2^*. Each of these electron spin systems differs from the others a little bit due to

- Local fluctuations of the magnetic field, e.g. by isotope variations of the semiconductor
- g-factor fluctuations
- Hyperfine structure of quantum dot states (modified strain or confinement) in the ensemble.

That leads to small fluctuations of the precession frequency and unavoidably, the qubits are not coherent anymore among themselves! This is only an ensemble effect; the single qubit can be in a coherent state for much longer time. T_2^* is only of importance for experiments where isolated qubits cannot be measured. For quantum devices, we must deal with single systems anyway. We summarize the relevant timescales here:

$$T_1 > T_2 > T_2^*$$

We will investigate the relevant mechanisms for excitons and electrons in InAs quantum dots in the following.

Spin relaxation

Spin relaxation is closely related to the foregoing discussion about the shape of dots in Chap. 3.3.4: Is the spin a good quantum number? If not, and this is the case for elongated quantum dots where basis states are made out of both spin states, then spin relaxation is very efficient. We will discuss possible spin-relaxation channels for excitons and single carriers. We follow the topic in historical order: First, excitonic spin relaxation was investigated as this is easily accessible using femtosecond titanium:sapphire laser oscillators for excitation and time-resolved detection of the luminescence. More sophisticated heterostructures and measurement setups made single-particle spin-relaxation measurements possible.

Exciton spin relaxation. Especially all-optical approaches to quantum computation with semiconductor quantum dots rely on long spin relaxation times of excitons in the dots. As we read-out our electronic spin state by addition of an unpolarized hole to the spin-polarized electron and observe the excitonic emission, excitonic spin-relaxation processes are of high importance here, too. The most apparent experiment is the resonant excitation of a spin-polarized exciton in the dot with a mode-locked titanium-sapphire laser combined with time- and polarization-resolved observation of the emitted photons. As the photon energy is in the near infrared, either a near-infrared synchroscan streak-camera [4], frequency upconversion in nonlinear crystals (like in [86]), or time-resolved single photon counting techniques (either with special photo-multiplier tubes or avalanche photo-diodes in Geiger mode) can be used. Figure 3.27 shows exemplarily the transients for the two circular polarizations of a quantum-dot ensemble recorded with a streak camera after circular excitation.

One can learn about spin relaxation from experiments with continuous-wave excitation, too: Gammon et al. [88] found that in GaAs quantum dots the spin relaxation rate is lower than the radiative recombination. In InGaAs quantum disks, Gotoh et al. [89] measured a spin relaxation time of about 0.9 ns. In self-assembled InAs quantum dots, Bayer et al. [82] did not observe spin relaxation during the radiative lifetime. In these experiments with non-resonant circularly polarized excitation the pure ground-state spin relaxation rate cannot be determined. Spin relaxation during energetic relaxation of the carriers, in the GaAs matrix and in the 2D wetting layer cannot be separated from intrinsic dot spin relaxation. A resonant excitation experiment was shown by Paillard et al. [86]. They found no spin relaxation at all during the carrier lifetime. The lifetime of an exciton is about 1 ns in InAs quantum dots. Most experiments suffer from non-symmetric quantum dots and exchange

---

[4] Hamamatsu C4334

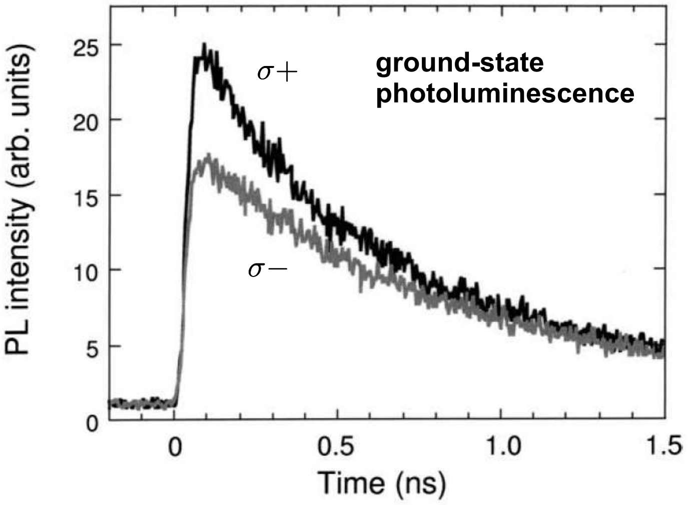

Figure 3.27: Time- and polarization-resolved photoluminescence of an InAs quantum-dot ensemble (from [87]). Here, the spin lifetime is rather short.

splitting (see Chap. 3.3.4) dominates spin relaxation processes.

Therefore, we consider now only nearly round, flat quantum dots grown along the crystal axis [001]. Because such a dot has much in common with a quantum well similar spin-relaxation channels can be expected. In III-V quantum wells, spin-orbit interaction is the most important mechanism for spin relaxation.

Spin-orbit interaction. A particle (electron) moving in an electrical field experiences an effective magnetic field in its rest frame. That magnetic field interacts with the spin of the electron. This interaction is dependent on the $\boldsymbol{k}$ vector of the electron. The magnetic field is obtained via the Lorentz transformation ($v \ll c$)

$$\boldsymbol{B}_{eff} = \frac{\boldsymbol{E} \times \boldsymbol{v}}{c^2}$$

$\boldsymbol{v}$ is the electron's velocity and $\boldsymbol{E}$ the electric field. From the Dirac equation, we then get the spin-orbit Hamiltonian in general form:

$$H_{SO} = \frac{\hbar^2}{4m^2c^2} (\boldsymbol{\nabla V} \times \boldsymbol{p}) \cdot \boldsymbol{\sigma}$$

$\boldsymbol{V}$ is the electric potential, $\boldsymbol{p}$ the momentum and $\boldsymbol{\sigma} = (\sigma_x, \sigma_y, \sigma_z)$ is the vector of Pauli spin matrices.

Where does the electric field come from? Zincblende semiconductors do not show inversion symmetry, this is called bulk inversion asymmetry. An electron moving though such a material feels an anisotropic potential. The theory on this is described by Dresselhaus [90]. The Hamiltonian in the valence band spin-1/2 basis (see Silbee [91] for a recent review) mixes the spin eigenstates of the symmetrical problem:

$$H_D = \beta(k_x\sigma_x - k_y\sigma_y)$$

β is the Dresselhaus constant. This interaction is the basis for the D'yakonov-Perel' [92] spin relaxation mechanism. It describes the precession of the electron spin around its direction of motion due to Dresselhaus effective magnetic field. In semiconductors with intrinsic piezoelectric fields these have to be considered, too.

In a heterostructure, there can also be a structural inversion asymmetry. For example in a quantum well where the barriers have different heights, an internal field builds up. This can also be supported by external gates where a voltage is applied. That is known as Bychkov-Rashba spin-orbit interaction [93] described by this Hamiltonian (α is the Rashba constant):

$$H_R = \alpha(k_x\sigma_y - k_y\sigma_x)$$

In self-assembled quantum dots Rashba asymmetry will always be present and contributes to spin relaxation.

Both contributions couple the ideally orthogonal spin eigenstates of the carriers and both mechanisms apply also to the holes in the valence band. A useful derivation of relaxation rates is given by Tsitsishvili et al. [94]. The spin of excitons in large quantum dots ($\geq 40\,nm$) relaxes in about 1 ns, in smaller dots these mechanisms are strongly suppressed because interaction with long-wavelength acoustical phonons is less efficient there.

Spin relaxation of single electrons. The determination of the exciton spin relaxation time is experimentally limited by the exciton lifetime. It has been suspected that the single-electron spin relaxation time is several orders of magnitude longer if measured correctly. Then, other spin relaxation mechanisms become relevant like hyperfine interaction with the spins host material and spin-orbit coupling. The measurement has firstly been realized by Kroutvar et al. [6]. In a Schottky-diode structure a spin-polarized exciton was excited optically but due to the band structure the hole tunnels out of the dot directly. They determined a lower limit on electron spin relaxation time of 20 ms. This was measured at a magnetic field of 4 Tesla. This field effectively polarizes all nuclear spins and spin-relaxation is inhibited. That experiment has been repeated for single-quantum dots [95].

We have seen that excitonic spin relaxation is efficient. It is not fully clear up to which amount excitonic effects were involved in these experiments [6, 95]. All-electrical spin injection devices where the electron spin is polarized with near-unity fidelity could clarify that: The spin-polarized electron is firstly injected at time T. Read-out of the electron spin must be done by injection of a hole at time $T + \Delta t$. If that is possible (not in devices discussed in this work), undisturbed long-time observation of the electron spin can be realized.

Spin decoherence

Maybe the most important requirement to realize quantum computation in a chosen system is the ability to perform the needed number of operations (like phase gates for single qubits, controlled-NOT gates of two or more qubits, and also the read-out process). The coherence of the qubits must be guaranteed during these operations.

In general, decoherence is caused by fluctuating fields, which reduce the coherences $\alpha_0\alpha_1^*$ and $\alpha_0^*\alpha_1$ from Eq. 3.1. An upper bound for the coherence time T_2 is given by the longitudinal relaxation time T_1: If we consider a two-level system with transition probability W between the two states. One can show (see e.g. [96]) that for the relaxation rate holds: $T_1^{-1} = 2W$. On the other side, the transverse relaxation rate T_2 cannot be smaller than all non-adiabatic contributions which are given by W. Hence, the lower limit of T_2 is given by:

$$T_2 \leq 2\,T_1 \tag{3.2}$$

In reality there are more contributions, T_2 is always lower than T_1. It is illustrative that after a system has relaxed longitudinally, the Bloch vector is along the z-axis. Then, there cannot exist any coherences in the (x, y) plane! For this reason the term “pure dephasing” has been introduced. Pure dephasing includes all decoherence processes except population relaxation.

Electrons in quantum dots. In semiconductor quantum dots several mechanisms are responsible for decoherence. The atoms which are in the dots do all have a nuclear spin as shown in Table 3.4.

The interaction of a single electron with the nuclei of the quantum dot is described by the Hamiltonian

$$H_N \;=\; \boldsymbol{S} \cdot \sum_i A_i \boldsymbol{I}^i \;=\; g\mu_B \boldsymbol{S} \cdot \boldsymbol{B}_N \tag{3.3}$$

$\boldsymbol{S}$ is the electron spin, A_i is the hyperfine coupling constant and $\boldsymbol{I}^i$ the nuclear spin of nucleus i. If the nuclear spins are randomly oriented (without external magnetic field and without long interaction with many spin-polarized electrons [99]), their impact

Isotope	**Natural abundance**	**Spin**	**Hyperfine constant** A (µeV)
^{69}Ga	60.1%	3/2	42
^{71}Ga	39.9%	3/2	
^{113}In	4.3%	9/2	56
^{115}In	95.7%	9/2	
^{75}As	100%	3/2	46

Table 3.4: Spin and hyperfine coupling constants for the relevant elements in an InAs/GaAs quantum-dot. Natural abundance data is taken from [97] and the hyperfine constant from Ref. [98]. For the latter we list the average of the isotopes.

can be described by an effective nuclear field $\boldsymbol{B}_N$. Electrons will precess around that field coherently. For an ensemble of dots that means relatively fast dephasing [100]. If an external magnetic field as small as 100 mT is applied, all nuclear spins are polarized and spin dephasing is suppressed. The intrinsic influence of nuclei on the electron spin is assumed to be smaller and leads to the following dependency [101]:

$$T_2 \propto \frac{N}{A}$$

N is the number of nuclei in the dot, for usual small InAs quantum dots it is in the range of 10^3 to 5×10^4. The expected electron-spin coherence time in quantum dots is in the order of microseconds. Recent experiments with GaAs quantum dots [102] actually reached that, 1.2 µs is their lower bound for T_2.

Interestingly, phonon-assisted spin-orbit interaction (see above) is theoretically unimportant for spin dephasing [103], it leads to no further reduction of T_2.

For holes the situation is different: It is commonly assumed (see, e.g. Ref. [100]) that hyperfine interaction of holes with nuclei is low because the hole Bloch functions have p-symmetry.

3.4 Conclusions

We discussed the properties of electrons in InAs/GaAs quantum dots. If the electron Zeeman doublet is used as a qubit coherence and spin relaxation have to be minimized: The quantum-dots should be thin in order to get a large ground-state – excited-state splitting which makes spin-relaxation inefficient. Laterally, they should also be relatively small because spin-orbit coupling is then suppressed. Even if the nuclear moment of indium is larger than that of gallium, high indium content is favorable for high quantization energy and large level separation. For operation in a magnetic field, nuclear spins are polarized and the spin coherence time reaches microseconds. However, the magnetic field must not be too large because a large energy difference of the spin states leads to faster loss of coherence due to longitudinal spin relaxation. That is one of the main reasons to use efficient spin aligners like ZnMnSe, which operate at low fields.

As a first approximation, a quantum dot can be considered as an in-plane quantum well with additional lateral parabolic confinement. Only accurate modeling and numerical simulations of a quantum dot leads to a coherent picture of the electronic states in the dot. We found very good agreement of the calculated electronic structure and experimental luminescence data.

Concerning the operation in a spin-LED device, it is indispensable that a single electron is in the quantum dot. For application within the context of quantum-information processing we have to deal with a single, isolated quantum system. Optical read-out of the spin state is the great advantage over other systems as coupling to the photon's helicity is exactly met.

Chapter 4

The spin-injection LED and spectral polarization

In this chapter, we use knowledge from the previous investigations and combine the spin-aligner and the quantum dots. We put the dots in the intrinsic region of a standard p-i-n light-emitting diode. Electrons from the top contact traverse the spin-aligner ZnMnSe layer where they get polarized with near-unity accuracy. We have seen that InAs/GaAs quantum dots are an ideal system for long-time storage of spin-polarized electrons. The challenge is now to transport the electrons to the dots while preserving the high spin polarization. We accomplish this in a p-i-n light-emitting diode (spin-LED) structure.

We discuss firstly details about the fabrication. We then explain the operation of the device with help of numerical band-structure calculations. Subsequently we show results on the initialization of quantum-dot ensembles with spin-polarized electrons (Chap. 4.3). We observed an unexpected inhomogeneity of the spin polarization in the ensemble, which we investigated afterwards. Using these results, we optimized the sample and were able to achieve near-unity fidelity in the preparation of spin-polarized electrons in single InAs/GaAs quantum dots (Chap. 4.5).

4.1 Structure and preparation

The semiconductor heterostructure (compare Fig. 4.1) shows a similar structure for all samples that are discussed in this work. First, on a p-doped GaAs substrate, a 475 nm thick p-doped GaAs buffer layer is grown ($p = 1.5 \times 10^{18}\, cm^{-3}$). The dopand

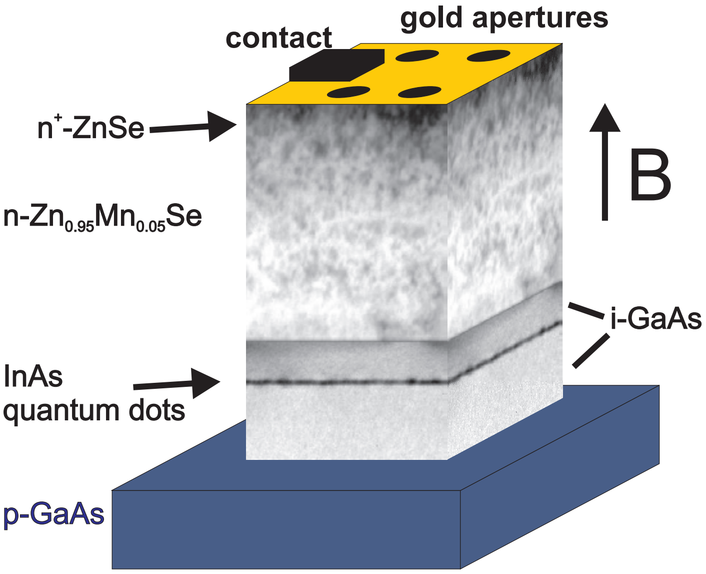

Figure 4.1: Scheme of the spin-LED. A cross-section TEM image is superimposed on a mesa. For details, see text.

was either carbon or beryllium, which had no influence on the characteristics. Then, 100 nm i-GaAs (undoped, intrinsic) is deposited to separate the doped region from the optically active quantum dots. This layer also leads to much cleaner subsequent growth of the dots. Then by deposition of InAs, the quantum dots are grown. To get high crystal quality, the underlying p-GaAs is grown at 570 ° C. InAs must be grown at a lower temperature (470 ° C). To avoid a long growth interruption while decreasing the sample temperature for dot growth, we reduce gradually the temperature during the lower i-GaAs layer growth. This is favorable in contrast to an interruption, which leads to surface contamination by residual substances from the growth chamber.

By adjustment of the quantum dot growth parameters, the morphology of the dots can be tuned over a broad range. Two mechanisms have to be mentioned: The amount of InAs deposited in relation to the critical thickness of InAs on GaAs and the deposition time and/or an additional ripening phase after dot growth. We have shown in Chap. 3, that for good spin storage a small quantum dot with high indium content is needed. Therefore, the amount of InAs must be close to the critical thickness. To accomplish this with high reproducibility we finally used a very low growth rate of $0.0057\,\mathrm{ML} \cdot \mathrm{s}^{-1}$. That is a good compromise between reproducibility and sample quality because even longer growth times would lead to the incorporation of residual impurities from the MBE chamber.

After dot growth, the dots are almost immediately (approx. 10 s interruption by shutter control) capped with intrinsic GaAs at the InAs growth temperature. For best results, we have chosen the cap layer thickness to be 25 nm, which is large enough to avoid any influence of the magnetic spin-aligner layer on the electrons in the quantum dots. We have also investigated the dependency of this thickness on spin injection fidelity, see Chap. 4.4.

Spin-aligner. For transport of this III-V heterostructure to the II-VI MBE we capped it with an arsenic layer which is evaporated in the II-VI chamber before growth start. This effectively prevents the surface from oxidation. Park et al. [104] found out that even without arsenic layer 65% spin transport efficiency can be reached. For spintronic applications, this is possibly sufficient but for high-fidelity preparation of spin states in quantum dots, the best possible measures have to be taken. A very critical point is the electronic interface between these two parts: The conduction band offset depends strongly on the growth-start conditions of the ZnSe based spin-aligner. To keep this offset low, we started under zinc-rich conditions, which leads to an offset in the conduction band as low as 26 meV [105]. The spin-aligner layer with various compositions (see Chap. 2) is usually grown with a thickness of 750 nm. For the first monolayers, the manganese shutter is left closed to avoid formation of MnAs or other unwanted compounds. To achieve an ohmic contact and to distribute the current evenly over the sample, we grow 200 nm highly-doped ($n = 5 \times 10^{18}\,\mathrm{cm}^{-3}$) ZnSe as the top layer.

Contact. An indium contact pad is used to provide good ohmic conductance from the top n-contact to the spin-aligner layer. It is structured by a standard photolithography lift-off process (quadratic fields with different sizes, for example $32 \times 32\,\mu\mathrm{m}^2$ for a $300 \times 300\,\mu\mathrm{m}^2$ mesa field). We deposited 200 nm indium in a high-vacuum evaporation chamber. After fabrication of the mesas, the sample is annealed to alloy the indium contact with the n-ZnSe contact layer for best electrical conductivity. This is done for 2.5 min at 150 °C in nitrogen atmosphere.

Nano-apertures. The gold nano-apertures are produced via an electron-beam lithography[1] lift-off process. We used a 300 nm-thick positive resist (PMMA, polymethyl-methacrylate) with a molecular weight of $950,000\,\mathrm{g\,mol}^{-1}$ [2]. The exposure (dose $100\,\mu\mathrm{C\,cm}^{-2}$) to high-energetic electrons breaks the hydrocarbon molecules which makes them easy soluble in the developer. The best results were achieved with

---

[1] System used: Zeiss Leo 35 electron beam system with Raith lithography add-on *Elphy plus*

[2] PMMA 950k A4, MicroChem Corp., USA

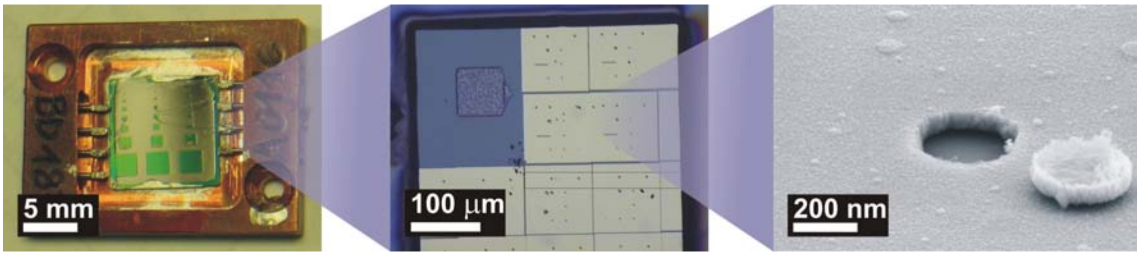

Figure 4.2: Left to right: Image of the device with the chip in the copper holder; optical microscope image of a single mesa with gold apertures; electron microscope image of a single aperture.

a mixture of methyl isobutyl ketone (MIBK) and isopropyl alcohol at a ratio of 1:3 for 20 s.

Mesa structuring. To keep the amount of energy (heat) deposited in the device small while allowing for high current densities we etched mesas out of the sample. This also decreases the possibility of a shortage due to crystal defects. By an additional photolithography step these mesas were defined and the semiconductor etched by a two-step process: First, removal of the II-VI layer by a diluted aqueous solution of potassium dichromate ($K_2CR_2O_7$) combined with hydrobromic acid (HBr). To etch further (about 2.5 µm) down into the III-V layers, an etchant with a higher concentration of potassium dichromate is used.

Packaging. In addition to the top contact, a p-type back contact is needed. Using silver conducting glue the sample is fixed on a special sample holder made out of copper. This ensures best electrical and heat conductivity. For electron injection, the 25 µm gold bonding wire is fixed to the top indium contact pad with a conducting epoxy adhesive [3]. At cryogenic temperatures a current of up to 1 A can be applied without any degradation. The completed sample is shown on the left in Fig. 4.2.

4.2 Operation

Even though the basic operation principle of the spin-LED is well known because it is similar to a standard p-i-n diode, we were interested in details of the band structure. The position of the Fermi level with respect to the confined states in the dots is one

---

[3] EPO-TEK H20E

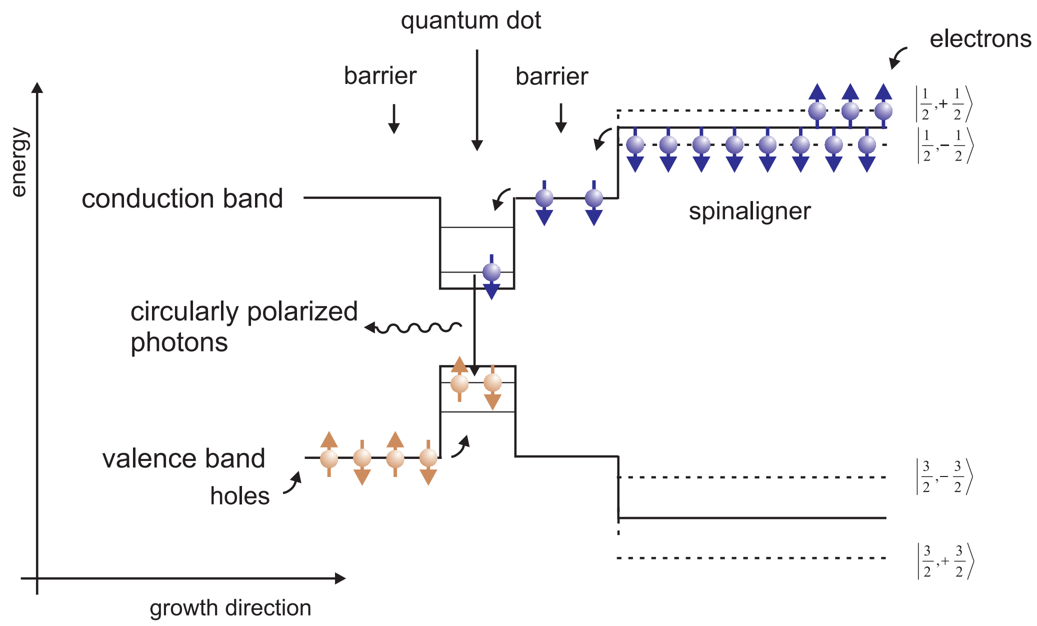

Figure 4.3: Principle of operation of the spin-LED: Unpolarized electrons from the top contact (shown on the right) are polarized in the spin-aligner layer before they enter the quantum dots. Recombination with a matching hole results in emission of a circularly polarized photon.

of the questions, which had to be addressed. First, we sketch the operation mode in Fig. 4.3, neglecting band-structure details. The unpolarized electrons from the metal lead get polarized due to the giant Zeeman splitting of the spin-up and down states in the spin aligner ZnMnSe (see Chap. 2). Via an injection mechanism discussed later, they reach the ground state of the quantum dot. As pointed out before the current density must be chosen such that two electrons entering a single quantum dot at the same time is excluded.

The holes from the bottom contact do not have a defined spin polarization when they enter the quantum dot. Due to the selection rules (see Chap. 3.3.1), the spin or helicity of the photon from electron-hole recombination is directly related to the spin polarization of the electron prior to recombination.

To get deeper insight into the band structure we conducted numerical simulations to calculate the band structure consistently. Here, we are mainly interested what changes in the band structure if an external voltage is applied. That requires solving the nonlinear Poisson equation

$$-\nabla\left(\epsilon(\boldsymbol{r})\nabla\cdot\Phi(\boldsymbol{r})\right)=\rho(\boldsymbol{r}) \tag{4.1}$$

$\epsilon(\boldsymbol{r})$ is the spatially inhomogeneous dielectric constant, Φ is the electric potential and $\rho(\boldsymbol{r})$ the electric charge density. The latter has contributions from electrons, holes, ionized donors and acceptors as well as from the piezoelectric polarization charges. Since the charge density depends on the electric potential, this is called non-linear Poisson equation.

The dynamics in a device under operation is satisfied by solution of the current continuity equation:

$$\frac{\partial \rho}{\partial t} = \nabla \cdot \boldsymbol{j} - r + g \tag{4.2}$$

Whereas $\boldsymbol{j}$ is the current density and r and g are the recombination and generation rate, respectively.

This is an iterative process because redistribution of carriers leads to an altered electrostatic environment and the potential $V(\boldsymbol{r})$ is changed. The process is repeated until the changes become small and a quasi-steady-state result is obtained. Additionally, recombination in the quantum dot region was taken into account. As these band structure calculations need to consider the whole device and very small (quantum dots) and large (spin aligner and barrier) regions meet, these simulations were only performed in one dimension (the growth direction). That means for the quantum dots that is has been approximated by a quantum well where the ground state exactly corresponds to the quantum-dot ground state.

We used the program nextnano [58] for the calculation and the relevant material parameters have been added to its material library. Fig. 4.4 shows two results of the simulation, Fig. 4.4a is without applied voltage and Fig. 4.4b is for 1.2 V applied in forward direction. Without applied voltage, the pinned Fermi levels in the doped regions determine the actual band structure appearance: About 1.3 V offset between the top of the conduction band in the substrate and the spin aligner. To inject electrons from the spin aligner into the quantum dots, about 1.2 V have to be applied which changes the structure to near-flat band conditions. Then, we observe that the electron quasi Fermi level has entered the conduction band states in the quantum dots. The same applies to the hole quasi Fermi level. The current flowing in the structure is compensated by recombination of the carriers in the quantum dots.

In our real devices, a larger voltage has to be applied because in our simulations perfectly ohmic contacts were assumed. In some devices this assumption was true but others needed up to 4 V for proper operation. This is independent of sample growth: Two different mesas on a single wafer can show completely different current-voltage characteristics, refer to Fig. 4.5.

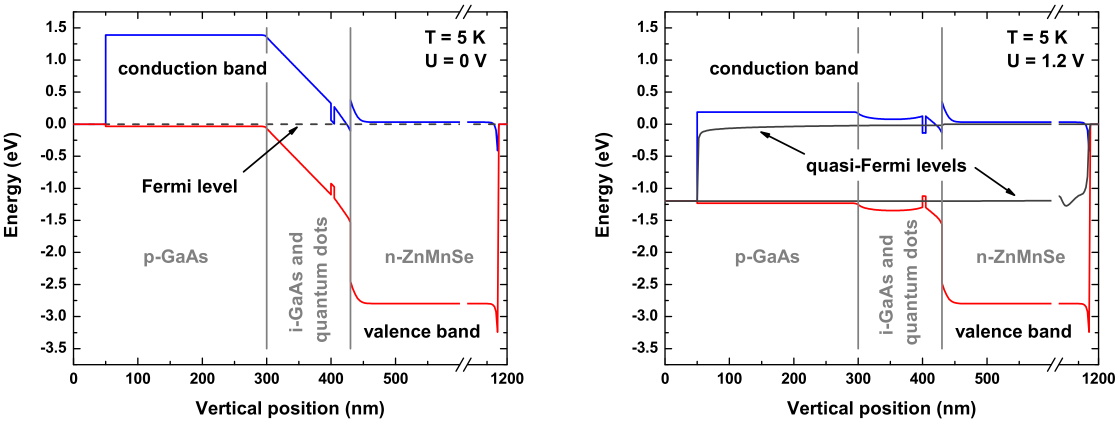

(a) Without applied voltage

(b) 1.2 V applied in forward direction

Figure 4.4: Band structure of a spin-LED device simulated numerically. By applying an external voltage in forward direction, the band structure is tilted towards flat-band conditions.

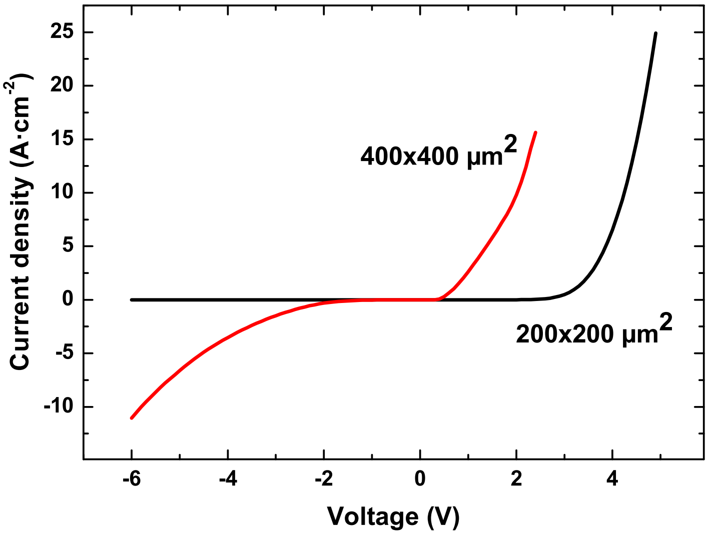

Figure 4.5: Current-voltage characteristics for two mesa on a single wafer. As the mesa area is different, current is normalized to account for that.

Different contacts are most probably responsible for this discrepancy: sometimes Schottky-type contacts form and a Schottky barrier alters the band structure close to the surfaces. This seems not to hinder a proper operation of the spin-LED neither does it influence the achieved spin polarization.

4.3 Spectral polarization: ensemble measurements

The measurements of the spin-LEDs were performed in a superconducting-coil magnet cryostat (0 . . . 14 T, 4.2 . . . 310 K) where optical access to the sample is provided. The sample can be adjusted via a three-axis piezo unit over a range of 7 mm in each spatial direction. This is essential to position a single mesa in the focus of a 35 mm lens which will collect the luminescence. Special care was taken that all optical elements were mounted tension-free and, if possible, free-lying. That ensures that no birefringence due to stress is introduced while cooling down to helium temperature. Such an effect would render all polarization-sensitive measurements unusable. We confirmed that Faraday rotation is negligible for our measurements. However, the effects of Fresnel refraction at the sample–vacuum interface and relaxed selection rules due to non-normal emission (see Chap. 3.3.1) are relevant here.

The polarization selectivity is achieved by passing the luminescence from the sample first through a broadband quarter-waveplate which transformes circular polarization into a linear one, and then select the desired polarization with a high-contrast Glan-Laser polarizer. The photons are focussed by an aspheric lens on a standard multimode fiber and guided to a spectrometer. For maximum flexibility, an InGaAs array detector recorded the signal.

An example for the electro-luminescence, selected for $\sigma-$ and $\sigma+$ polarized photons, is shown in Fig. 4.6 (black curves). The $\sigma+$ component is obviously much more intense. On the high-energy side of the quantum-dot emission, luminescence from recombination in the wetting-layer can be seen.

For a given magnetic field the circular polarization degree (CPD) of the emitted photons is calculated from the two circularly polarized electroluminescence spectra:

$$CPD = \frac{I(\sigma+) - I(\sigma-)}{I(\sigma+) + I(\sigma-)}$$

The red curve in Fig. 4.6 is the polarization degree calculated for each spectral position. We do observe a strong dependency of polarization on emission energy similar to Fig. 4.6. This has been observed in all our experiments with quantum-

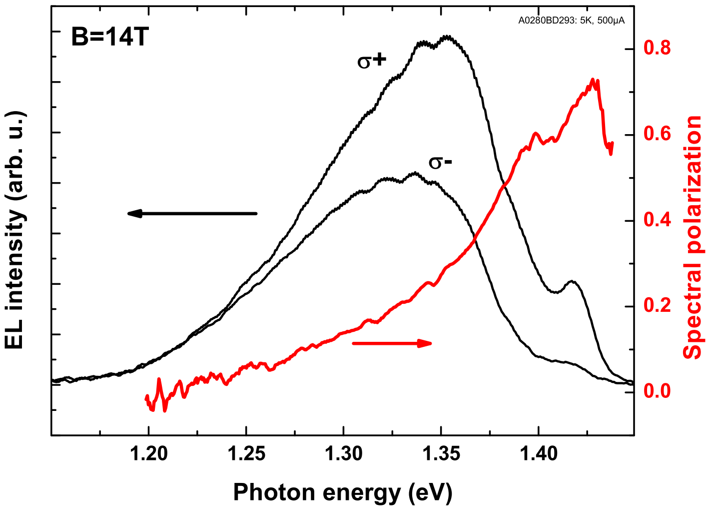

Figure 4.6: Example for the spectral polarization in a quantum-dot ensemble. Electroluminescence spectra were recorded for the two circular polarizations and the polarization degree calculated. An extreme dependency on photon energy is clearly visible.

dot samples. In devices with quantum wells as the active region, this effect is nonexistent [106, 107].

What kind of mechanism could lead to such a behavior? In the following we investigate the influence of different quantum dot parameters (shape, quantization energy), the influence of the local electronic Fermi level at the dot position, the temperature dependency and finally the influence of high current densities.

4.3.1 Different quantum-dot parameters

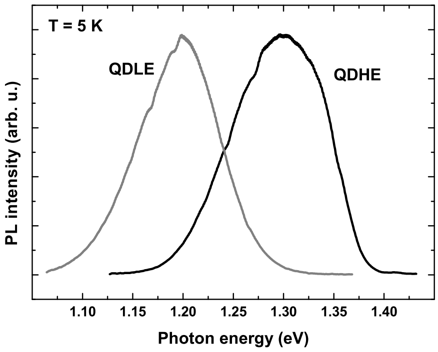

Figure 4.7: Photoluminescence spectra of the low- and high-energy quantum dots.

Mostly, two types of quantum dots are presented here which are called high-energy (HE) dots and low-energy (LE) dots (compare Fig. 3.7 on page 33). Figure 4.7 shows low-temperature photoluminescence spectra of both types of quantum dots. They overlap to some extent and the growth of the dots is very similar, details were given in Chap. 3.2.1.

Several traces of the spectral polarization are shown in Fig. 4.8 (see also [56]). For clarity, the electroluminescence signal is superimposed. Both samples are nominally equal with exception of the quantum dots. A possible interpretation is: In low-energy quantum dots (having a smaller quantization energy), spin relaxation processes via the excited

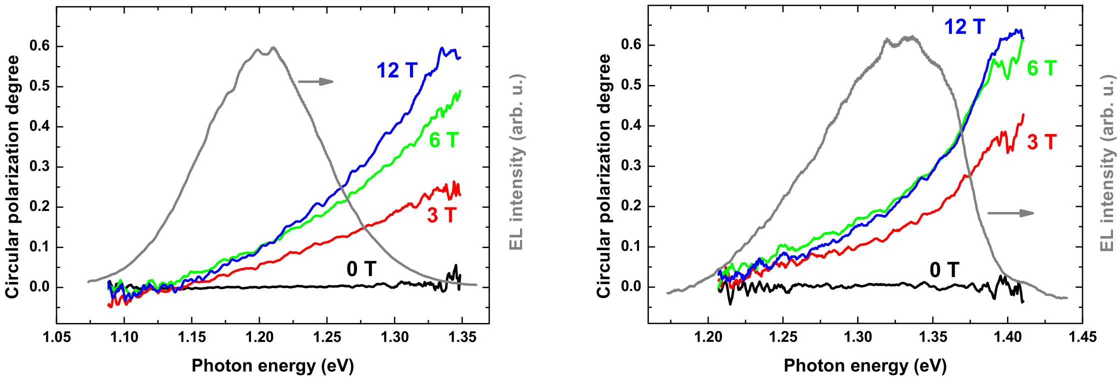

(a) Low-energy quantum dots (QDLE) (b) High-energy quantum dots (QDHE)

Figure 4.8: Spectral polarization for the low- and high-energy sample for different magnetic fields. The similarity is obvious despite of different quantum-dot morphology.

states are more probable than in high-energy quantum dots (with high quantization energy). This argument (and many others) does not agree with the fact that in the result with single-dot resolution near-unity polarized dots are equally distributed all over the spectrum (this will be shown later in Chap. 4.5).

Let us recall the main differences of the two quantum-dot types: From the high-resolution TEM images (see Chap. 3.2.1) we know that the low-energy dots are higher, have slightly higher indium concentration but are laterally smaller than the high-energy dots. For example spin-relaxation by spin-orbit interaction (see Chap. 3.3.5) should be much more efficient in laterally large quantum dots than in small ones! This mechanism is of no importance here.

4.3.2 Dependency on doping

The strong influence of the ZnMnSe doping concentration on the spin polarization of the electrons in the spin aligner was discussed in detail in Chap. 2. Here we will discuss the impact of high or low doping on the band structure and the states in the quantum dots. Not much about these topics can be found in literature due to the complexity of the problem: On one hand a macroscopic description with quasi-Fermi levels is needed to learn about the band structure. On the other hand, the quantum dots where the electron spin is analyzed are sensitive to local effects.

Let us start with simulations of the band structure for two different doping levels of

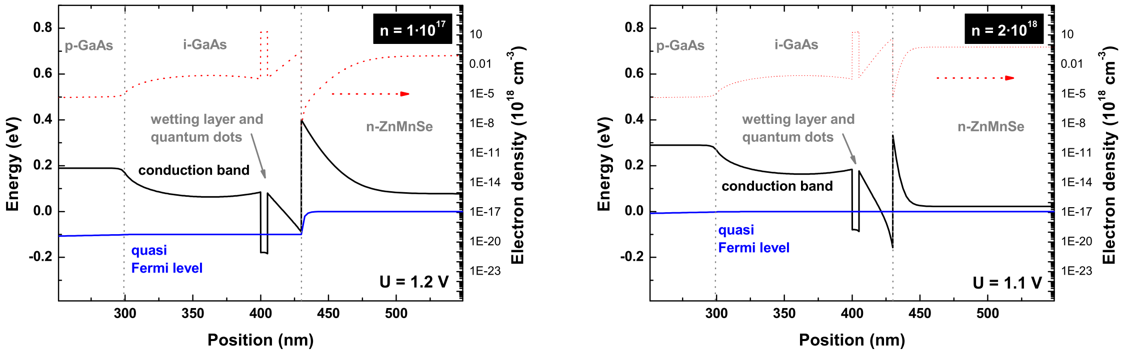

(a) Low-doped sample (b) High-doped sample

Figure 4.9: Simulated conduction-band structure in the quantum-dot region under applied voltage. The only difference in the two simulations is the doping concentration in the ZnMnSe spin aligner as shown in the plot. Shown is the conduction band edge at the Gamma-point (black), the electron quasi-Fermi level (blue) and the electron density (dotted red).

ZnMnSe: $n = 1\times10^{17}\,\mathrm{cm}^{-3}$ and $n = 2\times10^{18}\,\mathrm{cm}^{-3}$. The former corresponds to a very low, nondegenerate situation and the latter to the degenerate case. The simulations are very time-consuming even if conducted only in one dimension, as shown here. A shortcoming of our one-dimensional simulation is the loss of information about the density of states in the quantum-dot region. We modeled the quantum-dots with a 5 nm thick $\mathrm{In}_{0.4}\mathrm{Ga}_{0.6}\mathrm{As}$ layer. The band gap is then similar to the quantum-dot ground-state energy in the sample. As noted, the density of states is only an approximation as it is not discrete like in a real quantum-dot. Fully 3-dimensional quantum-mechanical calculations would be impossible on standard computers due to enormous memory consumption.

The (effective) electron Fermi level in the spin aligner layer is pinned to a certain energy value with respect to the band edge due to the relatively high donor concentration. The same holds for the p-type bottom GaAs layers. The Fermi-level in the intrinsic region in between is determined by the pinned levels and by the diffusion constants in the materials. Figure 4.9 shows the numerical simulation results for the two doping concentrations of the ZnMnSe layer. The plots are taken from voltage-dependent simulations.

The experimental current sheet density in operation of a standard mesa of $(400\,\mu\mathrm{m})^2$ at $500\,\mu\mathrm{A}$ is

$$j = 3125\,\frac{\mathrm{A}}{\mathrm{m}^2}.$$

Therefore, we selected the simulations in Fig. 4.9 for equal current density (which in turn is dependent on doping concentration): $U = 1.2\,\mathrm{V}$ ($n = 1 \times 10^{17}\,\mathrm{cm}^{-3}$) and $U = 1.1\,\mathrm{V}$ ($n = 2 \times 10^{18}\,\mathrm{cm}^{-3}$), respectively.

Clearly visible is the changed gap between the Fermi level and the conduction band for the two samples. Electrons diffuse from the spin-aligner n-ZnMnSe to the intrinsic GaAs and a potential valley forms. In the high-doped case, this valley is well filled with electrons resulting in a two-dimensional electron gas (2DEG). In the low-doped case, this valley is much less filled (factor of 20). Due to the finite mobility of electrons in the low-doped case, the quasi Fermi level gets a kink towards lower energies at the interface. That leads to a comparable position of the Fermi level in the quantum-dot region in both cases!

Sample	**Nominal donor concentration**	**Hall n (RT)**
SL2E18	$2 \cdot 10^{18}$ cm^{-3}	$\sim 2 \cdot 10^{18}$ cm^{-3}
SL1E18	$1 \cdot 10^{18}$ cm^{-3}	$\sim 8 \cdot 10^{17}$ cm^{-3}
SL2E17	$2 \cdot 10^{17}$ cm^{-3}	~ 0 cm^{-3}
SL0E0	0 cm^{-3}	~ 0 cm^{-3}

Table 4.1: Spin-LEDs of the doping series. The design concentration has been calibrated in relation to the $ZnCl_2$ cell temperature for MBE and the Hall data are determined experimentally.

Experimental situation. We compare here a set of samples (Table 4.1) with varied donor concentration in the spin-aligner. Using an extensive set of samples for calibration of the MBE system, we determined the needed cell temperature for $ZnCl_2$ first. Using these parameters, we have grown the spin-LEDs and reference samples for Hall-measurements. Room-temperature Hall results are shown in Table 4.1 for comparison. The two higher-doped samples show conductivity as expected. For sample SL2E17, the nominal electron concentration is $n = 2 \times 10^{17}\,\mathrm{cm}^{-3}$ but room-temperature Hall measurements of the spin-aligner layer itself were not possible due to high resistivity. From further Hall investigations, the reason could be fixed to trapping centers in the semiconductor. The impurity-trap density is at least $4 \cdot 10^{17}\,\mathrm{cm}^{-3}$. This leads to complete depletion of the ZnMnSe layer in that sample. We use an only 750 nm thick spin-aligner layer in these samples so the low conductivity does not hamper electrical transport. A similar situation seems to be valid for the nominally undoped sample SL0E0, conductivity is provided via impurity states.

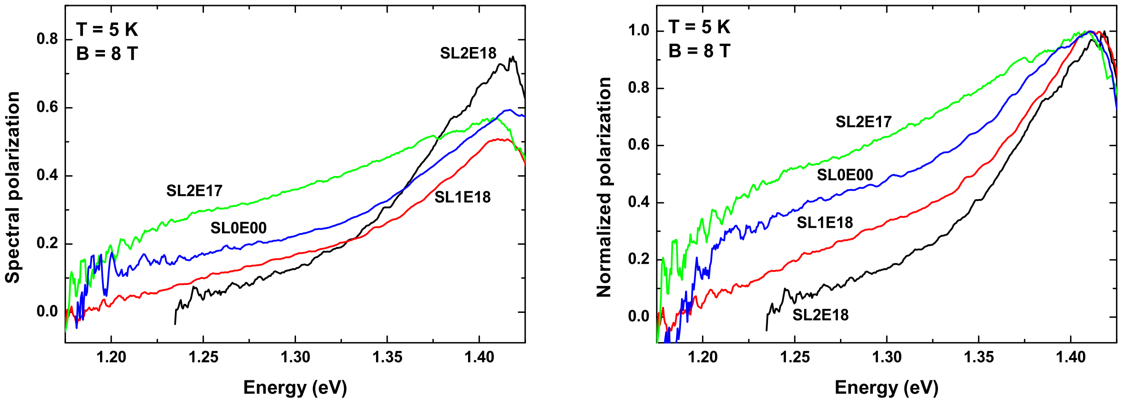

(a) Spectral polarization (b) Normalized data

Figure 4.10: Experimental spectral polarization at $B = 8\,\mathrm{T}$ in a series of samples with varied doping in the spin aligner. On the left, the raw polarization is shown. It is also determined by the spin-aligner performance. Therefore, the data on the right have been normalized to the maximum polarization at the high-energy side of the quantum dots.

In Fig. 4.10 the experimental spectral polarization is summarized. The left graph shows the raw polarization data. A dependency of the slope on the doping concentration can be seen which is more prominent on the low-energy side. However, the influence of sample preparation and/or MBE growth makes interpretation difficult. To compensate for these effects all plots have been normalized to the high-energy side polarization degree (right plot). A reduced donor concentration in the spin aligner clearly improves the low-energy quantum-dot polarization from near zero up to 50%!

An important question about the 2DEG at the interface between GaAs and ZnMnSe is the influence of magnetic ions: As mentioned above in the growth conditions, the manganese atomic beam is switched on a little later than the II-VI growth starts. We estimate a separation of a few nanometers. In previous investigations [108], we estimated that the range over which the giant Zeeman effect is effective is a few nanometers, too. The 2DEG electrons are not necessarily spin-polarized under these assumptions.

In high-doped samples, the electrons could tunnel from the 2-DEG directly into the quantum-dot ground state. The highly mobile electrons at the Fermi energy are highly polarized because they originate directly from the spin aligner. The low-energy electrons experienced many scattering processes and have lost their spin polarization. The existence of highly polarized quantum-dots at the low-energy side can be explained by the hypothesis that locally, the electronic structure is changed and electrons enter the dots from the wetting layer.

4.3.3 Energy relaxation of carriers

To find out which mechanism is dominant here, the mechanisms of carrier injection into quantum dots must be understood. Unfortunately, there are several competing theories, which will be summarized here.

Quantum-dot laser devices [109, 110] as well as semiconductor optical amplifiers (SOA) rely on the ultra-fast capture of carriers into a quantum dot [111]. The problem is that the density of states in a dot is discrete. Either electron-electron scattering (Auger process) or coupling to another particle is needed. If the energy difference is of the order of the phonon energy, it can perform that task. In structures, which are doped up to the quantum dot (spatially), plasmons can take that role but in undoped structures like ours, only phonon scattering is possible. The lack of a continuous phonon spectrum to match all possible state separation energies in the quantum-dot is commonly described as the "phonon bottleneck" [112]. Fortunately, this does not apply to real quantum dots and in most experiments relaxation happened in the picosecond range [113, 114, 115]. As most devices are operated in the high-carrier density regime, Auger electron-electron scattering seems to be the dominant mechanism.

Do many-carrier effects play a role in our devices, too? The strongest evidence of many-body effects in quantum-dots is the occupation of excited states (see also Chap. 3.2.4). We investigate this question in the following section.

4.3.4 Current-density dependency of polarization

Usually, we try to stay in the low electron-density range. The importance has already been shown in detail in Chap. 3.3.2. Summarizing, more than one electron in a single quantum dot must be avoided. Anyway, a qubit must be realized by a single quantum system. Apart from that, because electrons cannot occupy the same ground state, spin flips will occur if more electrons are in one dot. We can conclude that the polarization of the quantum-dot emission is a direct measure for dot occupancy.

Nevertheless, in optical measurements it is quite easy to reach multi-electron occupation in quantum dots. Is this also possible in a spin-LED device? Figure 4.11 shows experimental results, which are valid for all samples discussed here.

The sample shown here, QDLE, has a (relatively high) dot density $\rho = 2.5 \times 10^{11}\,\mathrm{cm}^{-2}$ as determined by plan-view transmission electron microcopy. Using that, we calibrated the current we applied to the number of electrons per quantum-dot flowing in a nanosecond through the sample. As one nanosecond is roughly the

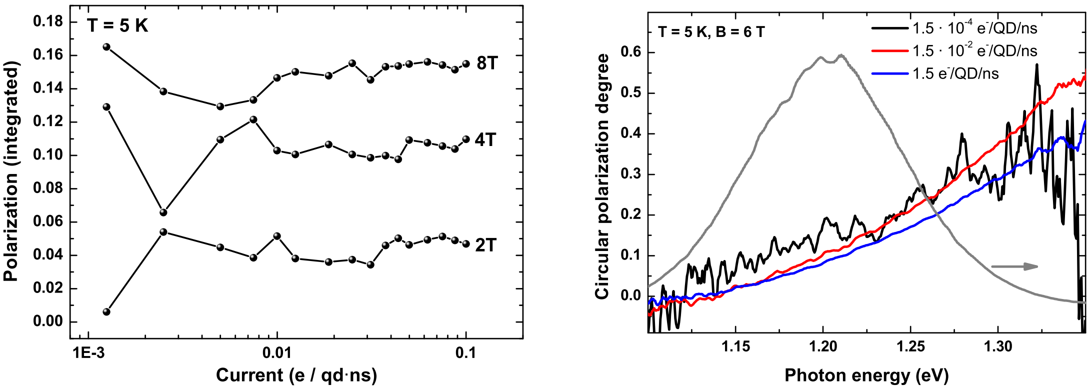

(a) Integrated polarization (b) Spectral polarization

Figure 4.11: Current-dependent measurements of a spin-LED. The polarization is determined by integrating the whole quantum-dot spectrum. Current is given in electrons per quantum-dot and nanosecond. The sample was not optimized and the over-all polarization values are small (sample QDLE).

lifetime of an electron-hole pair in the dot, this value is just the averaged occupation number of a single quantum dot. In electrical measurements, we have obviously problems reaching the many-electron-per-dot range (the maximum device current was about 100 mA).

Generally, no dramatic changes in the spectral polarization could be seen (Fig. 4.11b). On the low-energy side, the dots show slightly better polarized emission at very low current densities. Such an effect is expected for shell filling. We have to note that the effect is of the order of the detector's error. On the high-energy side, we observe the same behavior (but for higher currents). An effect similar to Pauli-blocking [67] would have opposite effect on the low- and high-energy side of the quantum dot ensemble. We can conclude that many-carrier effects do not play a role here! This topic has been discussed in [116].

4.3.5 Lattice temperature and spectral polarization

The main influence of temperature on the polarization is due to the thermal polarization of the manganese ions in the spin aligner (see Chap. 2.2). Only at low temperature, all spins are aligned and the electrons are optimally polarized.

To identify the effects of the temperature-dependent magnetization in the spin aligner we cannot analyze absolute polarization values. The performance of the spin-aligner

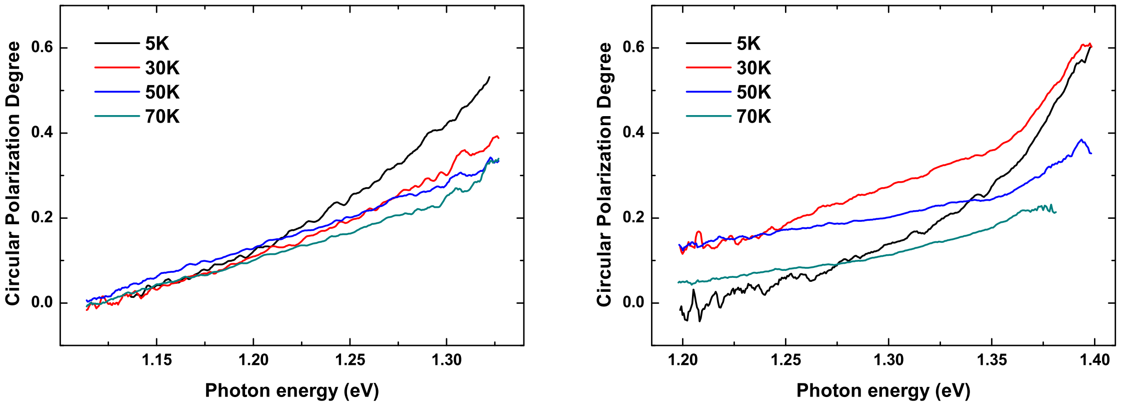

(a) Low-energy sample

(b) High-energy sample

Figure 4.12: Temperature dependent polarization traces for the low- and high-energy quantum-dot spin-LED. In both samples, the low-energy polarization decreases at higher temperature than the polarization on the high-energy side of the spectrum. The effect is more pronounced for the low-energy-quantum dot sample.

ZnMnSe is too sensitive to growth conditions. However, we can compare the relative polarization at the low-energy side of the quantum-dot emission with respect to the high-energy polarization. The latter is determined by the spin-aligner Zeeman splitting. Both samples in Fig. 4.12 show a surprising dependency on temperature: Up to 50 K, the polarization is increasing, more prominently on the low-energy side.

Such a behavior strongly suggests that we deal with an electron transport mechanism, which can be activated thermally. The electrons have to pass the depletion region in ZnMnSe close to the III-V/II-VI boundary. There, the electrons do not loose their polarization due to interaction with manganese ions. The next barrier is the i-GaAs spacer above the quantum dots. Two mechanisms help to overcome that barrier: tunneling through the barrier and/or a drift-diffusion process over the barrier.

The observed dependency on temperature suggests that we deal with a combination of both: a phonon-assisted tunneling process. Scattering with phonons activates electrons in the two-dimensional electron gas at the interface. At higher energy, the tunneling probability is enhanced.

The tunnel rate does always depend exponentially on barrier width. Therefore, we investigate in the following section the dependency of polarization on spacer thickness. Then we will summarize our investigations on the spectral polarization in spin-LEDs.

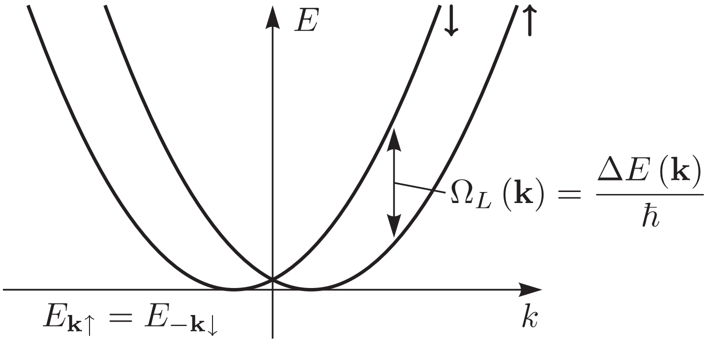

Figure 4.13: The $\boldsymbol{k}$-dependent effective magnetic field in the D'yakonov-Perel mechanism lifts the degeneracy of the spin-split bands for $k \neq 0$.

4.4 Spin transport in spin-LEDs

The spacer layer above the quantum dots influences the devices in several ways: If we consider tunneling of electrons from the III-V/II-VI boundary directly into the quantum dots, the spacer thickness determines the width of the tunnel barrier. If it is increased, the tunneling probability decreases exponentially. On the other hand, if we consider electron transport through the GaAs spacer layer, an increased thickness makes spin relaxation more probable. In non-centrosymmetric semiconductors like GaAs spin relaxation via the D'yakonov-Perel' - mechanism [92] (see Chap. 3.3.5) is important. The moving electron feels an effective magnetic field in its rest frame. The spin-degeneracy in the conduction band is lifted for $k \neq 0$. Because this effect is dependent on the direction of the electron momentum $\boldsymbol{k}$, the band dispersion looks like in Fig. 4.13. For a certain $\boldsymbol{k}$, two possible energies exist which leads to a precession of the electron spin around its $\boldsymbol{k}$-vector with frequency $\Omega_L = \Delta E/\hbar$.

This mechanism is also in agreement with higher spin polarization at elevated temperatures (see Fig. 4.12): Due to enhanced scattering of the electron with phonons, the precession is inhibited. That is similar to the quantum Zeno effect [117, 118] and is called "motional narrowing". The term is borrowed from NMR experiments:

Fluctuations in the chemical environment of a nuclear spin species leads to broadening of the resonance, as expected. However, if the shifts occur very often during the precession period the line shape of the resonance gets narrower again. The same applies here: If scattering events occur often during the precession time $\tau_{DP} = \Omega_L^{-1} >> \tau_p$ (τ_p is the impulse relaxation time), spin precession is effectively suppressed.

Let us now focus on the experiments with varied spacer thickness in Fig. 4.14a: In the sample series shown here, the spectral polarization shows similar behavior giving evidence for comparable sample structure and growth. The spectral polarization of the 75 nm spacer layer sample is strongly reduced. The averaged polarization (from

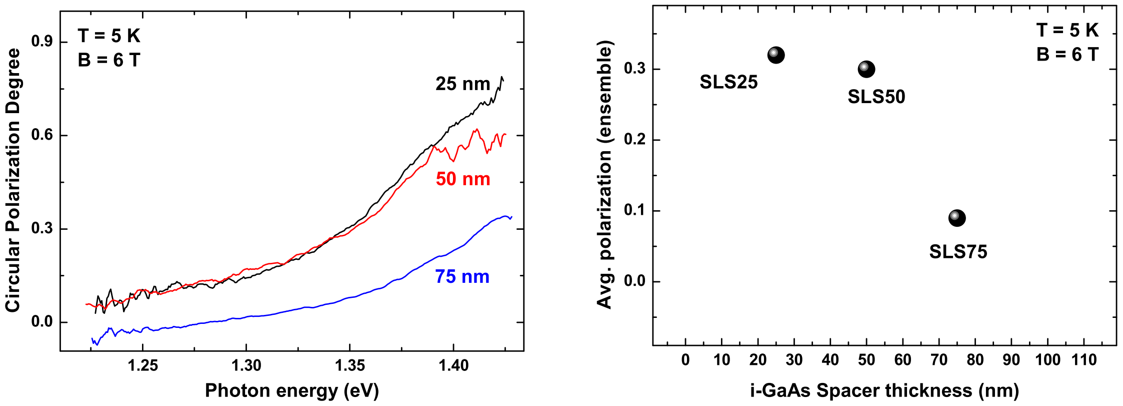

(a) Spectral polarization (b) Maximum ensemble polarization

Figure 4.14: Spectral polarization at constant magnetic field for three spacer thicknesses. The maximum value is plotted in the right panel. The strong decrease of polarization is contrasted to current spin-transport experiments as explained in the text.

1.25 eV . . . 1.43 eV) in Fig. 4.14b reflects the strong decrease of polarization.

Let us compare the fast loss of spin polarization with data from literature: First spin-resolved experiments on drifting electrons were done by Kikkawa et al. [119]: Measurements of the Faraday rotation angle with high spatial resolution revealed coherent spin transport over 100 µm in low-doped GaAs. Later experiments support these results [120, 121, 122]. In any case, spin relaxation due to Dresselhaus spin-orbit interaction would lead to exponential decrease of the spin polarization. In contrast, we observe an abrupt loss of spin polarization (Fig. 4.14b) at about 85 nm. It is also very unlikely that we do observe complete spin precession periods because our length scale is very small. However, sometimes spin relaxation and coherent precession is difficult to distinguish, see [122].

This suggests that the spin injection mechanism is based on tunneling. Only that can explain a very fast decrease of spin polarization on the scale of 100 nm.

4.5 Spin-state preparation in single quantum dots

In the previous sections, we investigated different properties of the spin-injection LED and presented the difficulties, which have to be considered to achieve high polarization. The main building blocks, the spin-aligner (see Chap. 2) and the quantum dots (Chap. 3) have now been optimized for best performance. In this chapter, the main result is shown: the successful preparation of spin-polarized electrons in single InAs quantum-dots. First, we summarize additional measures, which made single-dot experiments with spin-LEDs possible.

Measurement. The measurements on spin-LEDs with single-quantum-dot resolution were performed similar to the ensemble measurements. Now, the luminescence is detected through a single gold nano-aperture (see page 74). The 3D piezo translation stage is now needed to position such a single aperture below a 25×, NA = 0.4 microscope objective. Because large amounts of magnetic materials disturb the magnetic field at the sample position and can lead to mechanical damage, a commercial objective was disassembled and its mounting rebuilt with brass and high-grade non-magnetic steel.

To further enhance the spatial resolution of the setup we used a standard telecommunication single-mode fiber (patch-fiber) to collect the luminescence and guide it to a spectrometer. Dispersed in a 0.8 m-double-spectrometer with 2 × 1200 l/mm gratings it is detected by a special silicon CCD optimized for the near-infrared range[4]. The spectral resolution of the setup is 35 µeV. Still, the exposure time was about 60 s to record single quantum dot electro-luminescence. The poor signal intensity can easily be understood: Emission from the quantum-dot is spatially nearly isotropic and the gold aperture selects only a small solid angle. For a 700 nm diameter aperture the apex angle is only 0.02 °, the collection efficiency just 10^{-4}. In contrast to Chap. 4.3, we analyze here the emission of a single quantum dot. The $\sigma-$ and $\sigma+$ emission lines are split by the Zeeman splitting in the dot (due to the external magnetic field) and we can easily separate them in the recorded spectra. We do not need to consider the loss of polarization due to Fresnel refraction and relaxed selection rules here (compare Chap. 3.3.1).

---

[4] Andor DU-BR DD back-illuminated deep-depletion

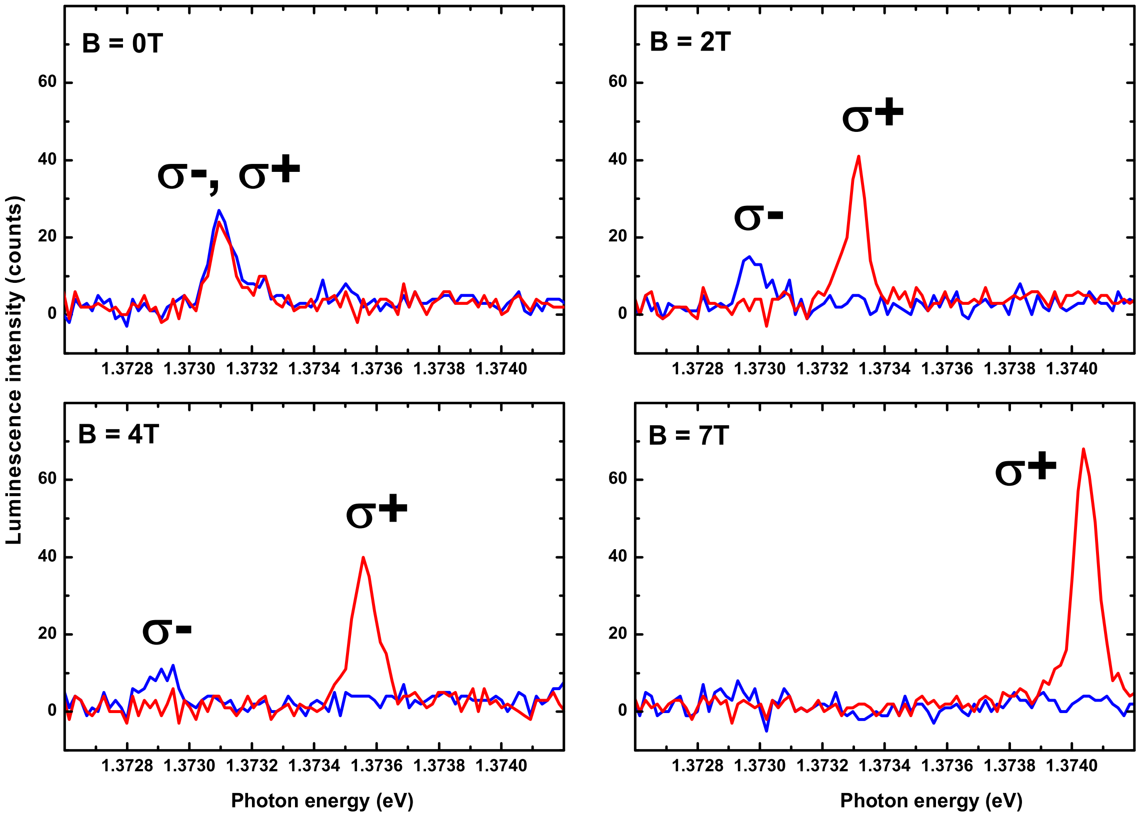

Figure 4.15: Polarized electro-luminescence of a single quantum dot. Without external magnetic field, both components contribute equally to the signal. If the field is increased, the $\sigma+$ component gets stronger. Finally, at $B = 7\,\mathrm{T}$, only emission from the higher spin-state is visible (sample SLSQD2).

4.5.1 Initialization of a single dot

The successful initialization of a single quantum dot with a spin-polarized electron is shown in Fig. 4.15. Without external magnetic field both electronic spin states are equally occupied leading to the same rate of $\sigma+$ and $\sigma-$ circularly polarized photons. If now the field is increased, the two former spin-degenerate states split up in the spin-doublet due to the Zeeman splitting in the dot. The excitonic splitting is of the order of 1 meV at $B = 7\,\mathrm{T}$. At $B = 7\,\mathrm{T}$, only emission from excitonic higher-lying ($\sigma+$-polarized) transition is visible, the other transition is weaker than our noise rate. The level ordering is consistent with the fact that the excitonic g-factor in the quantum dot is of opposite sign than the electronic g-factor in the spin-aligner layer, as emphasized in Fig. 4.16.

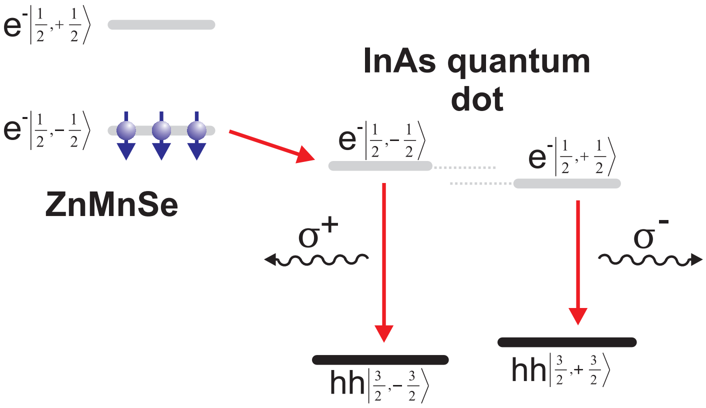

Figure 4.16: Spin quantum numbers and optical selection rules for electronic transitions in the spin-LED (magnetic field in faraday geometry). We want to emphasize the special level arrangement in the spin aligner and the dot: Via electron injection, the higher lying spin state is occupied in the dot.

The vanishing signal from the lower spin state clearly proves that spin relaxation within the ground state doublet is inefficient. We can give a lower limit to the spin initialization fidelity due to the noise. 5 counts noise level and 70 counts for the $\sigma+$ signal gives a lower bound to the spin polarization degree of 0.87. An upper bound to the spin initialization fidelity is given by the electron spin polarization in the spin aligner. At $B = 6\,\mathrm{T}$, the electronic Zeeman splitting in ZnMnSe is 3.4 meV and the spin temperature should match the lattice temperature of 5 K. Estimating the quantum-dot conduction-band Zeeman splitting to 0.45 meV our values correspond to an effective relative spin-state occupation[5] in the quantum dot of 132 mK. In comparison to the lattice temperature of 5 K, this value is only a little higher than that achieved with continuous optical laser cooling [17] of the spin state (20 mK).

In our electrical approach, the quantum dot is initially empty. On demand, by the external applied voltage, we can fill the dot with a spin-polarized electron. Additionally, the spin alignment and the spin storage are spatially separated and the spin aligner can feed many quantum dots. Our spin-aligner can be seen as a reservoir of spin-polarized electrons.

For the measurements, we integrated for 60 s to obtain the spectra. Magnetic-field dependent measurement took several hours. The device works reliable without any fluctuations in the signal. From previous investigations (see Chap. 4.3), we also know that performance is independent on small current fluctuations and little changes in temperature. The result is reproducible: The gold nano-apertures can be located

---

[5] Because the occupation is inverted here, the term spin temperature is misleading.

easily in our magneto micro-photoluminescence setup and the same quantum dot can be found again later after re-mounting the sample. We repeated this experiment several times and the spin polarization remained the same.

4.5.2 Micro-ensemble initialization

The single quantum-dot spin-state preparation can also be achieved via laser-assisted spin cooling. However, expansion to more quantum dots is connected with unwarranted effort like using many laser systems. In our electrical approach, extension to many dots is inherently given without additional complexity! We know from ensemble measurements (Chap. 4.3) that the polarization did not reach unity there. Therefore, we constructed our own ensemble measurement from many single-quantum-dot measurements. We did the analysis from Fig. 4.15 for many quantum dots and calculated the circular polarization degree of the emitted photons of single dots at a fixed magnetic field. The result is shown in Fig. 4.17. The circular polarization degree is plotted against the ground-state energy of the quantum dot (at zero magnetic field).

The limiting factor is here again the signal-to-noise ratio of the $\sigma+$ and $\sigma-$ polarized emission. A polarization of unity in Fig. 4.17 means that the $\sigma-$ signal is well below the noise.

In this measurement series, five quantum dots were initialized with highest fidelity! This is the first report [16] about the concurrent spin-state preparation in multiple quantum dots, be it optically or electrically.

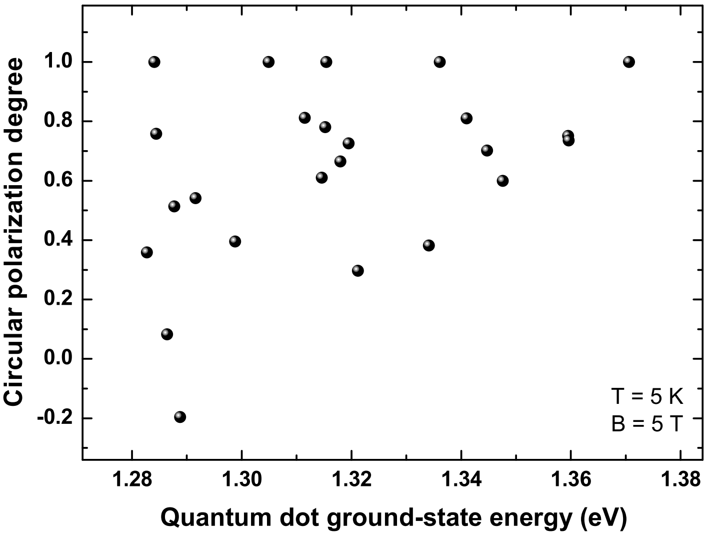

Figure 4.17: Circular polarization degree of the emitted photons of different quantum dots at $B = 5\,\mathrm{T}$. The x-axis is the zero-field ground-state energy of the corresponding quantum dot (sample SLSQD2).

Not all quantum dots show high polarization; even negative polarization can be found. For future applications, this does not play a major role since we can select a subset of the quantum dot ensemble to work with. We checked if this behavior is stable – indeed, over days the same quantum dots show high polarization or not.

We do also observe that the distribution of high- and low polarized dots is not homogeneous: on the high-energy side of the quantum-dot ensemble less often low-polarized emission is observed. This seems to be a general trend, observed in this experiment (Fig. 4.17) and in measurements on similar samples. With this new information we have discussed the ensemble measurements again: The low polarization at low quantum-dot energies in Chap. 4.3 is only due to the fact, that there are more quantum dots which are less polarized. Still, there are some dots highly polarized!

4.6 Conclusions

We demonstrated electrical preparation of spin-polarized electrons in InAs/GaAs quantum dots with very high fidelity. The outstanding properties of the spin-aligner ZnMnSe, the nearly lattice-matched growth on GaAs and the strong magnetic interaction allow for low-field spin-polarization of the electrons. The electrons can be transported over some 10 nm into the quantum dots. The separation of spin polarization and storage makes it possible to prepare spin-polarized electrons in quantum dots with different ground-state energy at the same time. We have shown this by concurrent initialization of 5 quantum dots whereas the determination of the polarization is limited by the noise of the detector.

In a quantum-dot ensemble, not all quantum dots show the same high polarization. The spectral polarization, which can be recorded without time-consuming single-dot analysis, does always show lower polarization at the low-energy side than on the high-energy side of the ensemble.

We analyzed the spectral polarization for different quantum-dots, varied spacing between spin-aligner and quantum-dots, different temperature and carrier densities and modified band structure by variation of the spin-aligner doping.

Based on the results we can identify the primary mechanisms and issues for high-fidelity spin injection: Initially (nearly) perfectly polarized electrons reach the 2-dimensional electron gas at the III-V/II-VI boundary. Preferable by a tunneling process they directly enter the quantum dot (or wetting layer) states. At increased spacer thickness such a process is strongly suppressed, the spacer must be kept relatively small. High-energy quantum dot states in small dots can be reached more easily via a tunneling process. The tunnel rate is strongly reduced for low-energy quantum dots. An increase of temperature can lead to a phonon-assisted tunneling process. Then, the effective tunnel barrier gets reduced.

The fact that we observe highly polarized emission from single quantum dots at the low-energy side of the quantum-dot ensemble is very promising for applications. This finding is difficult to explain on the basis of the models (including calculation of band structure and Fermi levels) used up to now. These models are based on the assumption of a local equilibrium. To explain our findings we propose that the assumption of a local equilibrium is in this case not valid, the equilibrium being disturbed by local modification of the electrical environment, possibly caused by donor or acceptor atoms or defects in the crystal.

For explanations, we have to ask how the calculation of the band structure and the Fermi levels is done: There, a local equilibrium is assumed. That assumption can be violated by local modification of the electrical environment, possibly caused by donor or acceptor atoms or defects in the crystal.

Chapter 5

Summary

Quantum computation makes interesting promises: Problems where classical computers are completely over-burdened like the simulation of even small quantum-mechanical systems could be solved efficiently. However, useful quantum computation has not been demonstrated up to now. One reason is that quantum bits are very sensitive to interaction with the environment and must therefore be kept well isolated. In this work, we tried to make a small contribution to realize the first step in any computation scheme: The well-defined initialization of quantum states, the preparation of spin-polarized electrons in self-assembled InAs/GaAs quantum dots. Our basic approach is to separate the polarization and the storage of the electrons spatially. That allows for using a material with strong magnetic interaction to polarize the electron spin with very high accuracy while leaving the electron undisturbed in the distant storage place, the quantum dot.

It is in the nature of self-assembly processes that the quantity of produced quantum dots is of no concern. However, because the growth is done well below thermodynamical equilibrium (and for other reasons), quantum dot morphology is slightly different from dot to dot. That makes understanding of the electronic properties challenging. We created a realistic three-dimensional model of a single quantum dot based on high-resolution transmission electron microscopy investigations. Extensive numerical calculations gave us a detailed picture of the electronic states and wave functions. The consistency with experimental photoluminescence data is convincing! We then analyzed theoretically the spin-polarization of electrons in quantum dots by optical means, namely recombination with an unpolarized hole. It turned out that the generation of photons by optical recombination and the photon propagation to the detector have to be considered very carefully. Even a slight departure from optimal normal-incidence detection leads to an underestimation of the original electron polarization.

Even though this point has been considered, the electron could have lost or changed the spin polarization while its stay in the dot. For our purposes here, the measurements are influenced by the longitudinal spin-relaxation time T_1. We analyzed the relevant causes like dot asymmetry and can conclude that spin relaxation is inefficient if an external magnetic field is present, which is the case here. We could determine the ideal dot geometry: Small and flat dots with high indium content. We have also studied the transverse relaxation or decoherence time T_2. Qubit operations can be done coherently during this time scale only. To summarize: InAs/GaAs quantum dots are an ideal system where decoherence is strongly suppressed. The electron coherence time is of the order of microseconds, which is enough for thousands of operations. This is essential because in quantum information processing, error correction is very costly, additional qubits have to be introduced. The first step, the initialization of the qubit, must therefore be done with highest possible accuracy.

The diluted magnetic semiconductor ZnMnSe is an ideal system for polarization of electron spins: At low temperatures already a small magnetic field is sufficient to fully deplete the unwanted Zeeman spin subband. In the first chapter, we reviewed other methods and justified our choice. However, in an electrical device conduction must be provided by addition of donor atoms. We have shown that this can reduce the performance drastically: The depletion of the upper spin sub-band is not guaranteed anymore. We were able to explain this by comparing a semi-analytical model with experimental results. We found very good agreement of experiment and theory and give a recipe for best-possible spin-aligner materials at the end of Chap. 2.

Local doping in the spin-aligner layer implicates additional consequences: At higher doping a 2-dimensional electron gas (2DEG) emerges at the III-V/II-VI interface. This is of very high importance for the transport of spin-polarized electrons into the quantum dots: The height of the tunneling barrier between the 2DEG and the dots is increased with increased doping in ZnMnSe. It is fortunate that a lower doping is beneficial also for the intrinsic ZnMnSe spin polarization! Concerning the transport of the electrons into the dots, we concluded that the injection mechanism is most likely a tunneling process directly into the quantum-dot states. This tunneling can be assisted by phonons, which make injection into low-energy quantum dots more efficient. We could show that the spectral polarization of the quantum-dot ensemble opens up an efficient method to investigate large amounts of quantum dots under various conditions.

After the successful optimization of the spin aligner, the quantum dots and the general device structure, we were able to demonstrate the high-fidelity preparation of a spin-polarized electron in a single quantum dot. We have shown that this works in a reliable and reproducible way. The strength of our device is that a quantum dot can be loaded with a spin-polarized electron on demand by application of an external voltage pulse.

In our device-geometry, the spin-aligner can be used to deliver spin-polarized electrons to many quantum dots. We achieved the concurrent preparation of highly spin-polarized electrons in a handful of quantum dots. Not all quantum dots show near-unity polarization but we have developed a method to select a choice of these dots with high polarization. Up to now, the here demonstrated use of a spin-LED to initialize electron spins in self-assembled quantum dots is the only way to tap the full potential of this system, the unique scalability towards many qubits.

Outlook. We were able to give strong indication about the origin of the differences in quantum-dot polarization. However, this topic asks for further investigation. One approach is to investigate electron transport through single quantum dots in the Coulomb-blockade regime. This is technologically very challenging, not much work has been done on this subject.

Towards a future all-electrical quantum computation device the electron- and hole injection has to be controlled separately. The short lifetime of the exciton makes it difficult to perform gate operations. Work on the delayed injection of the hole has already begun in our group. For these investigations, time-resolved measurements must be implemented. We have already set up a time-correlated single-photon-counting setup where single-photon detection with nanosecond time-resolution is possible.

The next step is the manipulation of the qubits. Coherent single-qubit operations have already been demonstrated for an electron in InAs quantum-dots: Rabi oscillations can be driven optically by coherent excitation of the trion state. For experiments with quantum-dot ensembles see [123, 124, 125, 126]. For excitons this has already been demonstrated some time ago (see [127, 128]). Recently, Koppens et al. realized Rabi oscillations of a single electron in a 2DEG quantum dot defined by electrical gates [129]. They used an on-chip coil ESR (electron spin resonance) technique. First steps in this direction have also been realized for the optically prepared electron spin in a self-assembled InAs/GaAs quantum dot [130]. ESR techniques are favorable because they act directly on the Zeeman-split electron spin states without optical excitation of the trion. The challenge is now to combine this with a spin-LED where the electron has been injected electrically.

Two-qubit gates rely on the coherent coupling of spatially well-separated electrons in self-assembled quantum dots. One idea is the coupling of the excitonic states of two qubits via an optical micro-cavity as proposed some time ago by Immamoglu et al. [7]. In our group, great effort is done in this direction, too [131, 132]. The question of the best way to realize coupling between qubits is not answered definitively, not even theoretically. The interaction being strongly linked to the quantum computation scheme and the algorithms one wants to simulate, there probably wont be a single solution ever.

Appendix A

Samples and their basic characterization

Only samples, which are discussed in detail in this work, are shown here!

A.1 Doping series

A.1.1 Epilayers of $\mathrm{Zn_{1-x}Mn_xSe}$

Sample	**$\mathrm{ZnCl_2}$ cell temperature**	**Expected n**	**n (RT)**	**Mobility μ (RT)**
B18	170 K	$8 \cdot 10^{17}\,\mathrm{cm^{-3}}$	$2.4 \cdot 10^{17}\,\mathrm{cm^{-3}}$	$112\,\mathrm{cm^2\,(Vs)^{-1}}$
B17	190 K	$2 \cdot 10^{18}\,\mathrm{cm^{-3}}$	$1.9 \cdot 10^{18}\,\mathrm{cm^{-3}}$	$249\,\mathrm{cm^2\,(Vs)^{-1}}$
B16	140 K	$2 \cdot 10^{17}\,\mathrm{cm^{-3}}$	$0\,\mathrm{cm^{-3}}$	NA

Table A.1: Samples for Hall measurements. They were fabricated to match the spin aligner layers of the spin-LEDs. NA means not available, RT is room temperature. A dependency between the ZnCl cell temperature and the resulting carrier concentration n is obtained.

A.1.2 Epilayers of $\mathrm{Zn_{1-x}Mn_xS_ySe_{1-y}}$ for TEM

Sample	**Internal reference**	**Manganese content x**	**Sulfur content y**
MN05	A0406-B003	HE	

Table A.2: Spin aligner samples for TEM to investigate the influence of lattice mismatch on spin polarization.

A.1.3 Spin-LEDs

Sample	**Internal reference**	**Spin aligner**	**Carrier concentration n (spin aligner, RT)**
SL2E18	A302-BD295	$Zn_{0.95}Mn_{0.05}Se$	$2 \cdot 10^{18}\,cm^{-3}$
SL1E18	A407-B006	$Zn_{0.95}Mn_{0.05}Se$	$8 \cdot 10^{17}\,cm^{-3}$
SL2E17	A407-B007	$Zn_{0.95}Mn_{0.05}Se$	$0\,cm^{-3}$
SL0E0	A421-B011	$Zn_{0.95}Mn_{0.05}Se$	$0\,cm^{-3}$

Table A.3: Spin-LED samples for doping dependent measurements. They are selected to show the same properties concerning the III-V part.

Sample	**$ZnCl_2$ cell temperature**	**Expected donor conc.**	**n (RT)**
SL2E18	198 K	$2 \cdot 10^{18}$ cm^{-3}	$\sim 2 \cdot 10^{18}$ cm^{-3}
SL1E18	180 K	$1 \cdot 10^{18}$ cm^{-3}	$\sim 8 \cdot 10^{17}$ cm^{-3}
SL2E17	140 K	$2 \cdot 10^{17}$ cm^{-3}	$\sim 0 cm^{-3}$
SL0E0	shutter closed	0 cm^{-3}	~ 0 cm^{-3}

Table A.4: Calibration for samples in Table A.3 using the $ZnCl_2$ cell temperature and interpolated values from Table A.1.

A.2 ZnMnSe thickness samples

Sample	Internal reference	Spin aligner thickness
SL250	A0358-BD313	250 nm
SL750	A0358-BD312	750 nm

Table A.5: Samples with varied spin-aligner thickness, they are grown on the same III-V wafer.

A.3 Spin transport samples

Sample	Internal reference	Spacer thickness	InAs thickness
SLS25	A302-BD295	25 nm	0.6 nm
SLS50	A280-BD293	50 nm	0.6 nm
SLS75	A314-BD300	75 nm	0.6 nm

Table A.6: Spin-LED samples of the spacer-thickness series. The spin aligner is not varied here and the quantum dots are grown the same way.

A.4 Samples with apertures for single-dot detection

A.4.1 Photoluminescence samples

Sample	Internal reference	Dot recipe
SQD1	A0438	HE

Table A.7: Samples with metal apertures for single-dot detection. The *dot recipe* corresponds to data in Table 3.1.

A.4.2 Spin-LED samples

Sample	**Internal reference**	**Dot recipe**
SLSQD1	A0406-B003	HE
SLSQD2	A0406-B004	HE
SLSQD3	A0407-B006	HE
SLSQD4	A0452-B015	HE

Table A.8: Spin-LED samples with metal apertures for single-dot detection. The *dot recipe* corresponds to data in Table 3.1.

A.5 Spin-LEDs with different quantum-dot morphology

Sample	**Internal reference**	**Monolayers deposited**	**Luminescence peak position**
QDLE	A0192	2.25	1.2 eV
QDHE	A0280	1.85	1.3 eV

Table A.9: Low-energy and High-energy quantum-dot samples. Growth details are given in Table 3.1. The TEM investigations are used to model the indium distribution for numerical calculations.

List of publications

Parts of this thesis have already been published:

Articles in regular journals

1. **Parallel preparation of highly spin-polarized electrons in single InAs/GaAs quantum dots**
   W. Löffler, M. Hetterich, C. Mauser, S. Li, T. Passow, H. Kalt
   Appl. Phys. Lett. **90**, 232105 (2007).

   Selected for the June 2007 issue of:
   Virtual Journal of Quantum Information

   Selected for the June 18, 2007 issue of:
   Virtual Journal of Nanoscale Science & Technology

2. ***Invited*: Electrical spin injection into InGa(N)As quantum structures and single InGaAs quantum dots**
   7th Int. Conf. on Excitonic Processes in Condensed Matter, Winston-Salem, NC, USA (EXCON 2006)
   M. Hetterich, W. Löffler, J. Fallert, N. Höpcke, H. Burger, T. Passow, S. Li, B. Daniel, B. Ramadout, J. Lupaca-Schomber, J. Hetterich, D. Litvinov, D. Gerthsen, C. Klingshirn, H. Kalt
   upgraded to regular paper
   Phys. Stat. Sol. (b) **243**, 3812 (2006).

3. **Electrical spin injection from ZnMnSe into InGaAs quantum wells and quantum dots**
   W. Löffler, D. Tröndle, J. Fallert, H. Kalt, D. Litvinov, D. Gerthsen, J. Lupaca-Schomber, T. Passow, B. Daniel, J. Kvietkova, M. Grün, C. Klingshirn, M. Hetterich
   Appl. Phys. Lett. **88**, 062105 (2006).

   Selected for the February 20, 2006 issue of:
   Virtual Journal of Nanoscale Science & Technology

Others

1. ***Invited:*** **Quanteninformationsverarbeitung mit Halbleiterquantenpunkten und Cavities**
   W. Löffler
   Minisymposium Nano Optics 2006, Konrad-Zuse-Zentrum für Informationstechnik Berlin (ZIB) (Talk)

Conferences with refereed proceedings

1. **Spin-polarized excitonic emission from single quantum dots after electrical injection**
   W. Löffler, M. Hetterich, C. Mauser, S. Li, J. Leuthold, H. Kalt
   10th Conference on the Optics of Excitons in Confined Systems (OECS 10), Patti, Messina, Italy, 2007 (Talk)
   paper submitted for publication in Phys. Stat. Sol.
2. **Spin and carrier relaxation dynamics in InAs/GaAs quantum-dot spin-LEDs**
   W. Löffler, N. Höpcke, C. Mauser, J. Fallert, T. Passow, B. Daniel, S. Li, D. Litvinov, D. Gerthsen, H. Kalt, M. Hetterich
   International Conference on Nanoscience and Technology (ICN+T) 2006, Basel, Switzerland (Talk)
   Journal of Physics: Conference Series **61**, 745 (2007).
3. **Electrical spin injection into InGaAs quantum dots**
   W. Löffler, D. Tröndle, J. Fallert, E. Tsitsishvili, H. Kalt, D. Litvinov, D. Gerthsen, J. Lupaca-Schomber, T. Passow, B. Daniel, J. Kvietkova, M. Hetterich
   8th Int. Workshop on Nonlinear Optics and Excitation Kinetics in Semiconductors (NOEKS 8), Münster, Germany, 2006 (Talk)
   Phys. Stat. Sol. (c) **3**, 2406 (2006).

4. **Electrical spin injection from ZnMnSe into InGaAs-based quantum structures**
W. Löffler, D. Tröndle, H. Kalt, D. Litvinov, D. Gerthsen, J. Lupaca-Schomber, T. Passow, B. Daniel, J. Kvietkova, M. Hetterich
Proc. 12th Int. Conf. on Modulated Semiconductor Structures (MSS-12), Albuquerque, 2005
Physica E **32**, 434 (2006).

5. **Investigation of InAs quantum dot growth for electrical spin injection devices**
T. Passow, S. Li, D. Litvinov, W. Löffler, J. Fallert, B. Daniel, J. Lupaca-Schomber, J. Kvietková, D. Gerthsen, H. Kalt, M. Hetterich
4th Int. Conf. on Quantum Dots (QD2006), Chamonix-Mont Blanc, France
Phys. Stat. Sol. (c) **3**, 3943 (2006).

Conference proceedings

1. **Parallel electrical spin preparation in InGaAs/GaAs quantum dots with high fidelity**
W. Löffler, C. Mauser, N. Höpcke, H. Kalt, S. Li, T. Passow, H. Reimer, M. Hetterich
Proc. European Conference on Lasers and Electro-Optics (CLEO Europe), Munich,
Germany, 2007 (Talk)
Paper IC-1605.pdf (IF3-4-THU 9:30)

2. **Electrical spin injection into InGaAs quantum dot ensembles and single quantum dots**
M. Hetterich, W. Löffler, J. Fallert, T. Passow, B. Daniel, J. Lupaca-Schomber, J. Hetterich, S. Li, C. Klingshirn, H. Kalt
Proc. 28th Int. Conf. on the Physics of Semiconductors, Vienna, Austria, 2006 (Talk)
AIP Conf. Proc. **893**, 1285 (2007).

3. **Optical spin injection from a ZnMnSe spin aligner into GaAs / AlGaAs quantum wells**
D. Tröndle, W. Löffler, Th. Passow, B. Daniel, M. Grün, M. Hetterich, C. Klingshirn, H. Kalt
in: Proc. Conference on Lasers and Electro-Optics (CLEO) / Quantum Electronics and Laser Science (QELS) and Photonic Applications, Systems and Technologies 2005, paper JTuC96, pp. 1064–1066, Optical Society of America, Washington DC (2005).

4. **Bestimmung des effektiven Mn-Gehalts und der Lande-Faktoren von semimagnetischen ZnMnSe Schichten**
   D. Tröndle, W. Löffler, Th. Passow, M. Grün, B. Daniel, M. Hetterich, C. Klingshirn, H. Kalt
   Nanofair 2004, Karlsruhe, VDI-Berichte **1839**, 129 (2004).

Presentations at DPG spring meetings

1. **Reliable parallel electrical initialization of spin-polarized electrons in InGaAs/GaAs quantum dots**
   W. Löffler, C. Mauser, J. Lupaca-Schomber, S. Li, T. Passow, H. Reimer, C. Klingshirn, M. Hetterich, H. Kalt
   Verhandl. DPG (VI) **42**, HL 31.5 (2007) (Talk).

2. **Effect of doping on the band structure in spin-LED devices**
   N. Höpcke, W. Löffler, C. Sailer, J. Lupaca-Schomber, S. Li, T. Passow, C. Klingshirn, M. Hetterich, H. Kalt
   Verhandl. DPG (VI) **42**, HL 46.67 (2007).

3. **Electrical spin injection from ZnMnSe into InGaAs/GaAs quantum dots**
   W. Löffler, D. Tröndle, J. Fallert, H. Kalt, D. Litvinov, D. Gerthsen, J. Lupaca-Schomber, T. Passow, B. Daniel, J. Kvietkova, M. Hetterich
   21st General Conf. of the EPS Condensed Matter Division
   Verhandl. DPG (VI) **41**, HL 41.2 (2006) (Talk).

4. **Magneto-optical investigation of InGaAs quantum dot spin-LEDs**
   J. Fallert, W. Löffler, D. Tröndle, C. Mauser, M. Hetterich, H. Kalt
   21st General Conf. of the EPS Condensed Matter Division
   Verhandl. DPG (VI) **41**, HL 9.89 (2006).

5. **Steps towards the realization of ZnMnSe-InGaAs/GaAs SQW electrical spin injection LEDs**
   M. Hetterich, J. Kvietkova, T. Passow, J. Lupaca-Schomber, B. Daniel, C. Klingshirn, W. Löffler, D. Tröndle, H. Kalt, D. Litvinov, D. Gerthsen
   Verhandl. DPG (VI) **40**, HL 16.8 (2005).

6. **Transport of spin-polarized excitons in $Zn_{1-x}Mn_xSe$-based II-VI heterostructures**
   B. Daniel, W. Löffler, D. Tröndle, C. Klingshirn, H. Kalt, M. Hetterich
   Verhandl. DPG (VI) **40**, HL 17.11 (2005).

7. **Optical spin injection from (Zn,Mn)Se into GaAs/(Al,Ga)As quantum wells**
   W. Löffler, D. Tröndle, T. Passow, B. Daniel, M. Kantner, M. Hetterich, M. Grün, C. Klingshirn, H. Kalt
   Verhandl. DPG (VI) **40**, HL 16.4 (2005).

8. **Bestimmung des effektiven Mn-Gehalts und der Landé-Faktoren von semimagnetischen $Zn_{1-x}Mn_xSe$ Schichten**
   D. Tröndle, H. Burger, W. Löffler, B. Daniel, M. Hetterich, E. Tsitsishvili, H. Kalt
   Verhandl. DPG (VI) **39**, HL 12.75 (2004).

Other, related publications:

Articles in regular journals

1. **Optical modes in pyramidal GaAs microcavities**
   F.M. Weber, M. Karl, J. Lupaca-Schomber, W. Löffler, S. Li, T. Passow, J. Hawecker, D. Gerthsen, H. Kalt, M. Hetterich
   Appl. Phys. Lett. **90**, 161104 (2007).

   Featured in:
   Nature Photonics **1**, 317 (2007), News & Views (doi: 10.1038/nphoton.2007.88).

   Selected for the April 30, 2007 issue of:
   Virtual Journal of Nanoscale Science & Technology.

2. **Localized and delocalized modes in coupled optical micropillar cavities**
   M. Karl, S. Li, T. Passow, W. Löffler, H. Kalt, M. Hetterich
   Optics Express **15**, 8191 (2007).

3. **Molecular beam epitaxy of phase pure cubic InN**
   J. Schörmann, D.J. As, K. Lischka, P. Schley, R. Goldhahn, S. F. Li, W. Löffler, M. Hetterich, H. Kalt
   Appl. Phys. Lett. **89**, 261903 (2006).

Conferences with refereed proceedings

1. **GaAs pyramids on GaAs/AlAs DBRs as alternative microcavities**
   M. Karl, F.M. Weber, J. Lupaca-Schomber, S. Li, T. Passow, W. Löffler, H. Kalt, M. Hetterich
   7th Int. Conf. on the Physics of Light-Matter Coupling in Nanostructures (PLMCN7), Havana, Cuba, 2007 (Talk)
   to be published in Superlattices and Microstructures.

Conference proceedings

1. **Optical modes in coupled pillar microcavities**
   M. Karl, S. Li, T. Passow, W. Löffler, E. Müller, D. Gerthsen, H. Kalt, M. Hetterich
   Proc. European Conference on Lasers and Electro-Optics (CLEO Europe), Munich,
   Germany, 2007 (Talk)
   Paper CK-238.pdf (CK-2-MON).
2. **Single and coupled microcavities – AlAs/GaAs DBR pillars and GaAs pyramids**
   M. Karl, W. Löffler, J. Lupaca-Schomber, T. Passow, S. Li, J. Hawecker, F. Pérez-Willard, D. Gerthsen, H. Kalt, C. Klingshirn, M. Hetterich
   Proc. 28th Int. Conf. on the Physics of Semiconductors, Vienna, Austria, 2006
   AIP Conf. Proc. **893**, 1133 (2007).
3. **Molecular Beam Epitaxy of phase-pure cubic InN**
   J. Schörmann, D.J. As, K. Lischka, P. Schley, R. Goldhahn, S. F. Li, W. Löffler, M. Hetterich, H. Kalt
   14th European Molecular Beam Epitaxy Workshop (Euro-MBE 2007), Sierra Nevada, Granada, Spain, 2007
   Talk MoA1.

Presentations at DPG spring meetings

1. **Magneto-excitons in GaInNAs / GaAs quantum well structures**
   M. Hetterich, A. Grau, W. Löffler, H. Kalt
   21st General Conf. of the EPS Condensed Matter Division
   Verhandl. DPG (VI) **41**, HL 15.5 (2006).

2. **Optical modes in pyramidal microcavities**
F.M. Weber, M. Karl, J. Lupaca-Schomber, W. Löffler, S. Li, T. Passow, J. Hawecker, D. Gerthsen, H. Kalt, M. Hetterich
Verhandl. DPG (VI) **42**, HL 46.70 (2007).
3. **GaAs pyramids as alternative micro-cavities**
M. Karl, F.M. Weber, J. Lupaca-Schomber, W. Löffler, S. Li, T. Passow, J. Hawecker, D. Gerthsen, H. Kalt, M. Hetterich
Verhandl. DPG (VI) **42**, HL 18.8 (2007).
4. **Coupled micro-cavities based on GaAs pillars**
M. Karl, W. Löffler, S. Li, T. Passow, E. Müller, F. Pérez-Willard, D. Gerthsen, H. Kalt, M. Hetterich
Verhandl. DPG (VI) **42**, HL 46.71 (2007).
5. **Conventional pillar-type and novel pyramidal III–V microcavities: Fabrication and characterization**
M. Karl, W. Löffler, J. Lupaca-Schomber, T. Passow, S. Li, F. Perez-Willard, J. Hawecker, D. Gerthsen, H. Kalt, C. Klingshirn, M. Hetterich
21st General Conf. of the EPS Condensed Matter Division
Verhandl. DPG (VI) **41**, HL 50.55 (2006).
6. **Magneto-optical spectroscopy and thermal annealing effects in GaInNAs/GaAs quantum well structures and bulk GaAsN**
A. Grau, P. Feinäugle, W. Löffler, H. Kalt, M. Hetterich
Verhandl. DPG (VI) **40**, HL 17.52 (2005).

References

[1] Richard P. Feynman. *Simulating physics with computers.* Int. J. Theor. Phys. **21**(1982), 467

[2] Seth Lloyd. *Universal Quantum Simulators.* Science **273**(1996), 1073

[3] W. K. Wootters and W. H. Zurek. *A single quantum cannot be cloned.* Nature **299**(1982), 802

[4] S. Dürr, T. Nonn, and G. Rempe. *Origin of quantum-mechanical complementarity probed by a 'which-way' experiment in an atom interferometer.* Nature **395**(1998), 33

[5] A. Greilich, D. R. Yakovlev, A. Shabaev, A. L. Efros, I. A. Yugova, R. Oulton, V. Stavarache, D. Reuter, A. Wieck, and M. Bayer. *Mode Locking of Electron Spin Coherences in Singly Charged Quantum Dots.* Science **313**(2006), 341

[6] M. Kroutvar, Y. Ducommun, D. Heiss, M. Bichler, D. Schuh, G. Abstreiter, and J. J. Finley. *Optically programmable electron spin memory using semiconductor quantum dots.* Nature **432**(2004), 81

[7] A. Imamoglu, D. D. Awschalom, G. Burkard, D. P. Divincenzo, D. Loss, M. Sherwin, and A. Small. *Quantum Information Processing Using Quantum Dot Spins and Cavity QED.* Phys. Rev. Lett. **83**(1999), 4204

[8] A. G. Aronov and G. E. Pikus. *Spin injection into semiconductors.* Sov. Phys. Sem. **10**(1976), 698

[9] M. Oestreich, J. Hübner, D. Hägele, P. J. Klar, W. Heimbrodt, W. W. Rühle, D. E. Ashenford, and B. Lunn. *Spin injection into semiconductors.* Appl. Phys. Lett. **74**(1999), 1251

[10] R. Fiederling, M. Keim, G. Reuscher, W. Ossau, G. Schmidt, A. Waag, and L. W. Molenkamp. *Injection and detection of a spin-polarized current in a light-emitting diode.* Nature **402**(1999), 787

[11] Y. Ohno, D. K. Young, B. Beschoten, F. Matsukura, H. Ohno, and D. D. Awschalom. *Electrical spin injection in a ferromagnetic semiconductor heterostructure.* Nature **402**(1999), 790

[12] Supriyo Datta and Biswajit Das. *Electronic analog of the electro-optic modulator.* Appl. Phys. Lett. **56**(1990), 665

[13] S. Ghosh and P. Bhattacharya. *Surface-emitting spin-polarized* $In_{0.4}Ga_{0.6}As/GaAs$ *quantum-dot light-emitting diode.* Appl. Phys. Lett. **80**(2002), 658

[14] Y. Chye, M. E. White, E. Johnston-Halperin, B. D. Gerardot, D. D. Awschalom, and P. M. Petroff. *Spin injection from (Ga,Mn)As into InAs quantum dots.* Phys. Rev. B **66**(2002), 201301

[15] J. Seufert, G. Bacher, H. Schömig, A. Forchel, L. Hansen, G. Schmidt, and L. W. Molenkamp. *Spin injection into a single self-assembled quantum dot.* Phys. Rev. B **69**(2004), 035311

[16] W. Löffler, M. Hetterich, C. Mauser, S. Li, T. Passow, and H. Kalt. *Parallel preparation of highly spin-polarized electrons in single InAs/GaAs quantum dots.* Appl. Phys. Lett. **90**(2007), 232105

[17] M. Atatüre, J. Dreiser, A. Badolato, A. Högele, K. Karrai, and A. Imamoglu. *Quantum-Dot Spin-State Preparation with Near-Unity Fidelity.* Science **312**(2006), 551

[18] M. I. D'yakonov and V. I. Perel'. *Theory of optical spin orientation.* In F. Meier and B. P. Zakharchenya, editors, *Optical Orientation*, volume 8 of *Modern Problems in Condensed Matter Sciences*, chapter 2, 11–72 (North Holland, 1984)

[19] S. A. Wolf, D. D. Awschalom, R. A. Buhrman, J. M. Daughton, S. von Molnár, M. L. Roukes, A. Y. Chtchelkanova, and D. M. Treger. *Spintronics: A Spin-Based Electronics Vision for the Future.* Science **294**(2001), 1488

[20] Igor Zutic, Jaroslav Fabian, and S. Das Sarma. *Spintronics: Fundamentals and applications.* Rev. of Mod. Phys. **76**(2004), 323

[21] J. Fabian, A. Matos-Abiague, C. Ertler, P. Stano, and I. Zutic. *Semiconductor Spintronics.* Acta Phys. Slov. **57**(2007), 565

[22] S. Ostanin, V. Trubitsin, J. B. Staunton, and S. Y. Savrasov. *Density Functional Study of the Phase Diagram and Pressure-Induced Superconductivity in P: Implication for Spintronics.* Phys. Rev. Lett. **91**(2003), 087002

[23] V. F. Motsnyi, J. De Boeck, J. Das, W. Van Roy, G. Borghs, E. Goovaerts, and V. I. Safarov. *Electrical spin injection in a ferromagnet/tunnel barrier/semiconductor heterostructure.* Appl. Phys. Lett. **81**(2002), 265

[24] C. H. Li, G. Kioseoglou, O. M. J. van't Erve, M. E. Ware, D. Gammon, R. M. Stroud, B. T. Jonker, R. Mallory, M. Yasar, and A. Petrou. *Electrical spin pumping of quantum dots at room temperature.* Appl. Phys. Lett. **86**(2005), 2503

[25] B. T. Jonker, G. Kioseoglou, A. T. Hanbicki, C. H. Li, and P. E. Thompson. *Electrical spin-injection into silicon from a ferromagnetic metal/tunnel barrier contact.* Nat. Phys. **3**(2007), 542

[26] G. Schmidt, D. Ferrand, L. W. Molenkamp, A. T. Filip, and B. J. van Wees. *Fundamental obstacle for electrical spin injection from a ferromagnetic metal into a diffusive semiconductor.* Phys. Rev. B **62**(2000), 4790

[27] H. Munekata, H. Ohno, S. von Molnar, Armin Segmüller, L. L. Chang, and L. Esaki. *Diluted magnetic III-V semiconductors.* Phys. Rev. Lett. **63**(1989), 1849

[28] P. T. Chiu and B. W. Wessels. *Evidence of room temperature sp-d exchange in InMnAs epitaxial films.* Appl. Phys. Lett. **89**(2006), 102505

[29] C. Felser, G. H. Fecher, and B. Balke. *Spintronics: A Challenge for Materials Science and Solid-State Chemistry.* Angew. Chem. Int. Ed. (2007)

[30] F. Heusler, W. Starck, and E. Haupt. *Über die ferromagnetischen Eigenschaften von Legierungen unmagnetischer Metalle.* Verh. der Phys. Ges. **5**(1903), 219

[31] H. Akinaga, T. Manago, and M. Shirai. *Material Design of Half-Metallic Zinc-Blende CrAs and the Synthesis by Molecular-Beam Epitaxy.* Jap. J. of Appl. Phys. **39**(2000), 1118

[32] J. K. Furdyna. *Diluted magnetic semiconductors.* J. Appl. Phys. **64**(1988), 29

[33] J. Müller. *Entwicklung und Charakterisierung von gitterangepassten ZnMnSSe/GaAs- Schichten in Spininjektions-Leuchtdioden.* Diplomarbeit (Universität Karlsruhe, 2007)

[34] J. M. Fatah, T. Piorek, P. Harrison, T. Stirner, and W. E. Hagston. *Numerical simulation of antiferromagnetic spin-pairing effects in diluted magnetic semiconductors and enhanced paramagnetism at interfaces.* Phys. Rev. B **49**(1994), 10341

[35] J. A. Gaj, R. Planel, and G. Fishman. *Relation of magneto-optical properties of free excitons to spin alignment of Mn2+ ions in Cd1-xMnxTe.* Solid State Commun. **29**(1979), 435

[36] D. Heiman, Y. Shapira, and S. Foner. *Exchange energy for conduction electrons in (ZnMn)Se derived from spin-flip Raman scattering and magnetization.* Solid State Comm. **51**(1984), 603

[37] K. Ohkawa, T. Mitsuyu, and O. Yamazaki. *Characteristics of Cl-doped ZnSe layers grown by molecular-beam epitaxy.* J. Appl. Phys. **62**(1987), 3216

[38] A. Storzum. *Chlordotierung von ZnSe, ZnS und CdS, Molekularstrahlepitaxie und elektrische Charakterisierung* (Diplomarbeit Universität Karlsruhe, 1998)

[39] R. Ferreira and G. Bastard. *''Spin''-flip scattering of holes in semiconductor quantum wells.* Phys. Rev. B **43**(1991), 9687

[40] B. Koopmans, M. van Kampen, and W. J. M. de Jonge. *Electron and Hole Spin Dynamics in Magnetic Semiconductors.* Phys. Stat. Sol. B **215**(1999), 217

[41] C. Camilleri, F. Teppe, D. Scalbert, Y. G. Semenov, M. Nawrocki, M. D'yakonov, J. Cibert, S. Tatarenko, and T. Wojtowicz. *Electron and hole spin relaxation in modulation-doped CdMnTe quantum wells.* Phys. Rev. B **64**(2001), 085331

[42] E. Tsitsishvili and H. Kalt. *Magnetic field effects on spin-flip processes in semimagnetic quantum wells.* Phys. Rev. B **73**(2006), 195402

[43] E. Tsitsishvili, R. v. Baltz, and H. Kalt. *Phonon-induced exciton spin relaxation in semimagnetic quantum wells.* Phys. Rev. B **71**(2005), 155320

[44] M. Lentze, L. Smith, D. Wolverson, P. Grabs, J. Geurts, and L. Molenkamp. *Spin flip Raman spectroscopy on heavily doped ZnMnSe layers.* Phys. Stat. Sol. C **3**(2006), 1118

[45] G. Bastard and L. L. Chang. *Spin-flip relaxation time of conduction electrons in* $Cd_{1-x}Mn_xTe$ *quantum wells.* Phys. Rev. B **41**(1990), 7899

[46] M. Hetterich, B. Daniel, C. Klingshirn, P. Pfundstein, D. Litvinov, D. Gerthsen, K. Eichhorn, and D. Spemann. *Lattice parameter and elastic constants of cubic ZnMnSe epilayers grown by molecular-beam epitaxy.* Phys. Stat. Sol. C **1**(2004), 649

[47] D. R. Yoder-Short, U. Debska, and J. K. Furdyna. *Lattice parameters of $Zn_{1-x}Mn_xSe$ and tetrahedral bond lengths in $A^{II}_{1-x}Mn_xB^{VI}$ alloys.* J. Appl. Phys. **58**(1985), 4056

[48] G. Mie. *Contributions to the Optics of Turbid Media, Especially Colloidal Metal Solutions.* Annalen der Physik (1908)

[49] Kurt Nassau. *The Physics and Chemistry of Color* (Wiley, New York, 2001)

[50] I. N. Stranski and L. Krastanow. *Zur Theorie der orientierten Ausscheidung von lonenkristallen aufeinander.* Sitzungsberichte d. Akad. d. Wissenschaften in Wien. Abt. IIb **146**(1937), 797

[51] L. Goldstein, F. Glas, J. Y. Marzin, M. N. Charasse, and G. Le Roux. *Growth by molecular beam epitaxy and characterization of InAs/GaAs strained-layer superlattices.* Appl. Phys. Lett. **47**(1985), 1099

[52] J. Stangl, V. Holý, and G. Bauer. *Structural properties of self-organized semiconductor nanostructures.* Rev. Mod. Phys. **76**(2004), 725

[53] M. A. Reed, J. N. Randall, R. J. Aggarwal, R. J. Matyi, T. M. Moore, and A. E. Wetsel. *Observation of discrete electronic states in a zero-dimensional semiconductor nanostructure.* Phys. Rev. Lett. **60**(1988), 535

[54] A. Rosenauer and D. Gerthsen. *Atomic Scale Strain and Composition Evaluation from High-Resolution Transmission Electron Microscopy Images.* In *Adv. in Imaging and Electron Phys.*, volume 107, 121 (Academic Press, 1999)

[55] T. Passow, S. Li, D. Litvinov, W. Löffler, J. Fallert, B. Daniel, J. Lupaca-Schomber, J. Kvietkova, D. Gerthsen, H. Kalt, and M. Hetterich. *Investigation of InAs quantum dot growth for electrical spin injection devices.* Phys. Stat. Sol. C **3**(2006), 3943

[56] W. Löffler, D. Tröndle, J. Fallert, E. Tsitsishvili, H. Kalt, D. Litvinov, D. Gerthsen, J. Lupaca-Schomber, T. Passow, B. Daniel, J. Kvietkova, and M. Hetterich. *Electrical spin injection into InGaAs quantum dots.* Phys. Stat. Sol. C **3**(2006), 2406

[57] E. Tsitsishvili, R. V. Baltz, and H. Kalt. *Exciton spin relaxation in single semiconductor quantum dots.* Phys. Rev. B **67**(2003), 205330

[58] S. Birner. *Nextnano3.* `http://www.wsi.tu-muenchen.de/nextnano3`

[59] M. Grundmann, O. Stier, and D. Bimberg. *InAs/GaAs pyramidal quantum dots: Strain distribution, optical phonons, and electronic structure.* Phys. Rev. B **52**(1995), 11969

[60] Gustavo A. Narvaez, Gabriel Bester, and Alex Zunger. *Dependence of the electronic structure of self-assembled (In,Ga)As/GaAs quantum dots on height and composition.* J. Appl. Phys. **98**(2005), 043708

[61] Gabriel Bester and Alex Zunger. *Cylindrically shaped zinc-blende semiconductor quantum dots do not have cylindrical symmetry: Atomistic symmetry, atomic relaxation, and piezoelectric effects.* Phys. Rev. B **71**(2005), 045318

[62] Andrei Schliwa, Momme Winkelnkemper, and Dieter Bimberg. *Impact of size, shape, and composition on piezoelectric effects and electronic properties of In(Ga)As/GaAs quantum dots.* Phys. Rev. B **76**(2007), 205324

[63] C. Mauser. *Einzelquantenpunktspektroskopie an Spininjektions-Leuchtdioden mittels Metall-Halbleiter-Nanostrukturen.* Diplomarbeit (Universität Karlsruhe, 2006)

[64] W. Seifert, N. Carlsson, A. Petersson, L.-E. Wernersson, and L. Samuelson. *Alignment of InP Stranski-Krastanow dots by growth on patterned GaAs/GaInP surfaces.* Appl. Phys. Lett. **68**(1996), 1684

[65] P. Atkinson, S.P. Bremner, D. Anderson, G.A.C. Jones, and D.A. Ritchie. *Molecular beam epitaxial growth of site-controlled InAs quantum dots on prepatterned GaAs substrates.* Microelectron. J. **37**(2006), 1436

[66] E. Dekel, D. Gershoni, E. Ehrenfreund, J. M. Garcia, and P. M. Petroff. *Carrier-carrier correlations in an optically excited single semiconductor quantum dot.* Phys. Rev. B **61**(2000), 11009

[67] V. K. Kalevich, M. Paillard, K. V. Kavokin, X. Marie, A. R. Kovsh, T. Amand, A. E. Zhukov, Y. G. Musikhin, V. M. Ustinov, E. Vanelle, and B. P. Zakharchenya. *Spin redistribution due to Pauli blocking in quantum dots.* Phys. Rev. B **64**(2001), 045309

[68] K. Brunner, G. Abstreiter, G. Böhm, G. Tränkle, and G. Weimann. *Sharp-line photoluminescence and two-photon absorption of zero-dimensional biexcitons in a GaAs/AlGaAs structure.* Phys. Rev. Lett. **73**(1994), 1138

[69] Findeis F. *Optical spectroscopy on a single InGaAs/GaAs quantum dot in the few-exciton limit.* Solid State Commun. **114**(2000), 227

[70] Qiang Wu, Robert D. Grober, D. Gammon, and D. S. Katzer. *Excitons, biexcitons, and electron-hole plasma in a narrow 2.8-nm* $GaAs/Al_xGa_{1-x}As$ *quantum well.* Phys. Rev. B **62**(2000), 13022

[71] H. Kamada, H. Ando, J. Temmyo, and T. Tamamura. *Excited-state optical transitions of excitons and biexcitons in a single* $In_xGa_{1-x}As$ *quantum disk.* Phys. Rev. B **58**(1998), 16243

[72] C. Klingshirn. *Semiconductor Optics* (Springer, Heidelberg, 2006), 3rd edition

[73] Ulrike Woggon. *Dynamics of optical excitations in quantum dots of wide-gap semiconductors.* In *Advances in Solid State Physics 35*, 175–196 (Springer Berlin / Heidelberg, 1995)

[74] A. Barenco and M. A. Dupertuis. *Quantum many-body states of excitons in a small quantum dot.* Phys. Rev. B **52**(1995), 2766

[75] C. E. Pryor and M. E. Flatté. *Accuracy of Circular Polarization as a Measure of Spin Polarization in Quantum Dot Qubits.* Phys. Rev. Lett. **91**(2003), 257901

[76] Benjamin Schumacher. *Quantum coding.* Phys. Rev. A **51**(1995), 2738

[77] D.D. Awschalom, D. Loss, and N. (Eds.) Samarth. *Semiconductor Spintronics and Quantum Computation.* NanoScience and Technology (Springer, 2002)

[78] R. M. Stevenson, R. J. Young, P. Atkinson, K. Cooper, D. A. Ritchie, and A. J. Shields. *A semiconductor source of triggered entangled photon pairs.* Nature **439**(2006), 179

[79] R. J. Young, R. M. Stevenson, P. Atkinson, K. Cooper, D. A. Ritchie, and A. J. Shields. *Improved fidelity of triggered entangled photons from single quantum dots.* New J. Phys. **8**(2006), 29

[80] N. Akopian, N. H. Lindner, E. Poem, Y. Berlatzky, J. Avron, D. Gershoni, B. D. Gerardot, and P. M. Petroff. *Correlated and entangled pairs of single photons from semiconductor quantum dots.* J. Appl. Phys. **101**(2007), 1712

[81] S. Rodt, R. Heitz, A. Schliwa, R. L. Sellin, F. Guffarth, and D. Bimberg. *Repulsive exciton-exciton interaction in quantum dots.* Phys. Rev. B **68**(2003), 035331

[82] M. Bayer, A. Kuther, A. Forchel, A. Gorbunov, V. B. Timofeev, F. Schäfer, J. P. Reithmaier, T. L. Reinecke, and S. N. Walck. *Electron and Hole g Factors and Exchange Interaction from Studies of the Exciton Fine Structure in* $In_{0.60}Ga_{0.40}As$ *Quantum Dots.* Phys. Rev. Lett. **82**(1999), 1748

[83] M. Bayer, G. Ortner, O. Stern, A. Kuther, A. A. Gorbunov, A. Forchel, P. Hawrylak, S. Fafard, K. Hinzer, T. L. Reinecke, S. N. Walck, J. P. Reithmaier, F. Klopf, and F. Schäfer. *Fine structure of neutral and charged excitons in self-assembled In(Ga)As/(Al)GaAs quantum dots.* Phys. Rev. B **65**(2002), 195315

[84] D. Gammon, S. W. Brown, E. S. Snow, T. A. Kennedy, D. S. Katzer, and D. Park. *Nuclear Spectroscopy in Single Quantum Dots: Nanoscopic Raman Scattering and Nuclear Magnetic Resonance.* Science **277**(1997), 85

[85] D. Gammon, Al. L. Efros, T. A. Kennedy, M. Rosen, D. S. Katzer, D. Park, S. W. Brown, V. L. Korenev, and I. A. Merkulov. *Electron and Nuclear Spin Interactions in the Optical Spectra of Single GaAs Quantum Dots.* Phys. Rev. Lett. **86**(2001), 5176

[86] M. Paillard, X. Marie, P. Renucci, T. Amand, A. Jbeli, and J. M. Gérard. *Spin Relaxation Quenching in Semiconductor Quantum Dots.* Phys. Rev. Lett. **86**(2001), 1634

[87] A. Tackeuchi, R. Ohtsubo, K. Yamaguchi, M. Murayama, T. Kitamura, T. Kuroda, and T. Takagahara. *Spin relaxation dynamics in highly uniform InAs quantum dots.* Appl. Phys. Lett. **84**(2004), 3576

[88] D. Gammon, E. S. Snow, B. V. Shanabrook, D. S. Katzer, and D. Park. *Homogeneous Linewidths in the Optical Spectrum of a Single Gallium Arsenide Quantum Dot.* Science **273**(1996), 87

[89] H. Gotoh, H. Ando, H. Kamada, A. Chavez-Pirson, and J. Temmyo. *Spin relaxation of excitons in zero-dimensional InGaAs quantum disks.* Appl. Phys. Lett. **72**(1998), 1341

[90] G. Dresselhaus. *Spin-Orbit Coupling Effects in Zinc Blende Structures.* Phys. Rev. **100**(1955), 580

[91] Robert H. Silsbee. *Spin-orbit induced coupling of charge current and spin polarization.* J. Phys.: Condens. Matter **16**(2004), R179

[92] M. I. D'yakonov and V. I. Perel'. *Spin relaxation of conduction electrons in noncentrosymetric semiconductors.* Sov. Phys. Solid State **13**(1972), 3023

[93] Yu A Bychkov and E I Rashba. *Oscillatory effects and the magnetic susceptibility of carriers in inversion layers.* J. Phys. C: Sol. State Phys. **17**(1984), 6039

[94] E. Tsitsishvili, R. v. Baltz, and H. Kalt. *Exciton-spin relaxation in quantum dots due to spin-orbit interaction.* Phys. Rev. B **72**(2005), 155333

[95] Robert J Young, Samuel J Dewhurst, R Mark Stevenson, Paola Atkinson, Anthony J Bennett, Martin B Ward, Ken Cooper, David A Ritchie, and Andrew J Shields. *Single electron-spin memory with a semiconductor quantum dot.* New J. Phys. **9**(2007), 365

[96] Malcolm H. Levitt. *Spin dynamics* (Wiley, 2002), repr. edition. ISBN 0-471-48921-2, 0-471-48922-0

[97] M. J. Winter. *webelements.com*

[98] P.-F. Braun, B. Urbaszek, T. Amand, X. Marie, O. Krebs, B. Eble, A. Lemaitre, and P. Voisin. *Bistability of the nuclear polarization created through optical pumping in $In_{1-x}Ga_xAs$ quantum dots.* Phys. Rev. B **74**(2006), 245306

[99] M. N. Makhonin, A. I. Tartakovskii, I. Drouzas, A. B. Van'kov, T. Wright, J. Skiba-Szymanska, A. Russell, V. I. Fal'ko, M. S. Skolnick, H. Y. Liu, and M. Hopkinson. *Long nuclear spin decay times controlled by optical pumping in individual quantum dots.* cond-mat (2007)

[100] P.-F. Braun, X. Marie, L. Lombez, B. Urbaszek, T. Amand, P. Renucci, V. K. Kalevich, K. V. Kavokin, O. Krebs, P. Voisin, and Y. Masumoto. *Direct Observation of the Electron Spin Relaxation Induced by Nuclei in Quantum Dots.* Phys. Rev. Lett. **94**(2005), 116601

[101] Alexander V. Khaetskii, Daniel Loss, and Leonid Glazman. *Electron Spin Decoherence in Quantum Dots due to Interaction with Nuclei.* Phys. Rev. Lett. **88**(2002), 186802

[102] J. R. Petta, A. C. Johnson, J. M. Taylor, E. A. Laird, A. Yacoby, M. D. Lukin, C. M. Marcus, M. P. Hanson, and A. C. Gossard. *Coherent Manipulation of Coupled Electron Spins in Semiconductor Quantum Dots.* Science **309**(2005), 2180

[103] Vitaly N. Golovach, Alexander Khaetskii, and Daniel Loss. *Phonon-Induced Decay of the Electron Spin in Quantum Dots.* Phys. Rev. Lett. **93**(2004), 016601

[104] Y. D. Park, B. T. Jonker, B. R. Bennett, G. Itskos, M. Furis, G. Kioseoglou, and A. Petrou. *Electrical spin injection across air-exposed epitaxially regrown semiconductor interfaces.* Appl. Phys. Lett. **77**(2000), 3989

[105] V. Pellegrini, M. Börger, M. Lazzeri, F. Beltram, J. J. Paggel, L. Sorba, S. Rubini, M. Lazzarino, A. Franciosi, J.-M. Bonard, and J.-D. Ganiére. *Tuning of ZnSe-GaAs band discontinuities in heterojunction diodes.* Appl. Phys. Lett. **69**(1996), 3233

[106] W. Löffler, D. Tröndle, J. Fallert, H. Kalt, D. Litvinov, D. Gerthsen, J. Lupaca-Schomber, T. Passow, B. Daniel, J. Kvietkova, M. Grün, C. Klingshirn, and M. Hetterich. *Electrical spin injection from ZnMnSe into InGaAs quantum wells and quantum dots.* Appl. Phys. Lett. **88**(2006), 062105

[107] M. Hetterich, W. Löffler, J. Fallert, N. Höpcke, H. Burger, T. Passow, S. Li, B. Daniel, B. Ramadout, J. Lupaca-Schomber, M. Hetterich, D. Litvinov, D. Gerthsen, K. Klingshirn, and H. Kalt. *Electrical spin injection into InGa(N)As quantum structures and single InGaAs quantum dots.* Phys. Stat. Sol. B **243**(2006), 3812

[108] W. Löffler. *Untersuchungen zur Spininjektion in Halbleiter-Heterostrukturen.* Diplomarbeit (Universität Karlsruhe, 2004)

[109] D. L. Huffaker, G. Park, Z. Zou, O. B. Shchekin, and D. G. Deppe. *1.3 mu m room-temperature GaAs-based quantum-dot laser.* Appl. Phys. Lett. **73**(1998), 2564

[110] A. E. Zhukov, A. R. Kovsh, N. A. Maleev, S. S. Mikhrin, V. M. Ustinov, A. F. Tsatsul'nikov, M. V. Maximov, B. V. Volovik, D. A. Bedarev, Yu. M. Shernyakov, P. S. Kop'ev, Zh. I. Alferov, N. N. Ledentsov, and D. Bimberg. *Long-wavelength lasing from multiply stacked InAs/InGaAs quantum dots on GaAs substrates.* Appl. Phys. Lett. **75**(1999), 1926

[111] P. Borri, S. Schneider, W. Langbein, U. Woggon, A. E. Zhukov, V. M. Ustinov, N. N. Ledentsov, Zh. I. Alferov, D. Ouyang, and D. Bimberg. *Ultrafast carrier dynamics and dephasing in InAs quantum-dot amplifiers emitting near 1.3-mu m-wavelength at room temperature.* Appl. Phys. Lett. **79**(2001), 2633

[112] U. Bockelmann and G. Bastard. *Phonon scattering and energy relaxation in two-, one-, and zero-dimensional electron gases.* Phys. Rev. B **42**(1990), 8947

[113] T. S. Sosnowski, T. B. Norris, H. Jiang, J. Singh, K. Kamath, and P. Bhattacharya. *Rapid carrier relaxation in* $In_{0.4}Ga_{0.6}As/GaAs$ *quantum dots characterized by differential transmission spectroscopy.* Phys. Rev. B **57**(1998), R9423

[114] T. Muller, F. F. Schrey, G. Strasser, and K. Unterrainer. *Ultrafast intraband spectroscopy of electron capture and relaxation in InAs/GaAs quantum dots.* Appl. Phys. Lett. **83**(2003), 3572

[115] S. Trumm, M. Wesseli, H. J. Krenner, D. Schuh, M. Bichler, J. J. Finley, and M. Betz. *Spin-preserving ultrafast carrier capture and relaxation in InGaAs quantum dots.* Appl. Phys. Lett. **87**(2005), 153113

[116] W. Löffler, N. Höpcke, C. Mauser, J. Fallert, T. Passow, B. Daniel, S. Li, D. Litvinov, D. Gerthsen, H. Kalt, and M. Hetterich. *Spin and carrier relaxation dynamics in InAs/GaAs quantum-dot spin-LEDs.* J. Phys.: Conf. Ser. **61**(2007), 745

[117] B. Misra and E. C. G. Sudarshan. *The Zeno's paradox in quantum theory.* J. Math. Phys. **18**(1977), 756

[118] Wayne M. Itano, D. J. Heinzen, J. J. Bollinger, and D. J. Wineland. *Quantum Zeno effect.* Phys. Rev. A **41**(1990), 2295

[119] J. M. Kikkawa and D. D. Awschalom. *Lateral drag of spin coherence in gallium arsenide.* Nature **397**(1999), 139

[120] Y. Kato, R. C. Myers, A. C. Gossard, and D. D. Awschalom. *Coherent spin manipulation without magnetic fields in strained semiconductors.* Nature **427**(2004), 50

[121] S. A. Crooker and D. L. Smith. *Imaging Spin Flows in Semiconductors Subject to Electric, Magnetic, and Strain Fields.* Phys. Rev. Lett. **94**(2005), 236601

[122] S. Malzer M. Beck, C. Metzner and G. H. Döhler. *Spin lifetimes and strain-controlled spin precession of drifting electrons in GaAs.* Europhys. Lett. **75**(2006), 597

[123] M. V. Gurudev Dutt, Jun Cheng, Bo Li, Xiaodong Xu, Xiaoqin Li, P. R. Berman, D. G. Steel, A. S. Bracker, D. Gammon, Sophia E. Economou, Ren-Bao Liu, and L. J. Sham. *Stimulated and Spontaneous Optical Generation of Electron Spin Coherence in Charged GaAs Quantum Dots.* Phys. Rev. Lett. **94**(2005), 227403

[124] Sophia E. Economou, L. J. Sham, Yanwen Wu, and D. G. Steel. *Proposal for optical U(1) rotations of electron spin trapped in a quantum dot.* Phys. Rev. B **74**(2006), 205415

[125] A. Greilich, R. Oulton, E. A. Zhukov, I. A. Yugova, D. R. Yakovlev, M. Bayer, A. Shabaev, Al. L. Efros, I. A. Merkulov, V. Stavarache, D. Reuter, and A. Wieck. *Optical Control of Spin Coherence in Singly Charged (In,Ga)As/GaAs Quantum Dots.* Phys. Rev. Lett. **96**(2006), 227401

[126] Yanwen Wu, Erik D. Kim, Xiaodong Xu, Jun Cheng, D. G. Steel, A. S. Bracker, D. Gammon, Sophia E. Economou, and L. J. Sham. *Selective Optical Control of Electron Spin Coherence in Singly Charged GaAs-*$Al_{0.3}Ga_{0.7}As$ *Quantum Dots.* Phys. Rev. Lett. **99**(2007), 097402

[127] H. Kamada, H. Gotoh, J. Temmyo, T. Takagahara, and H. Ando. *Exciton Rabi Oscillation in a Single Quantum Dot.* Phys. Rev. Lett. **87**(2001), 246401

[128] T. H. Stievater, Xiaoqin Li, D. G. Steel, D. Gammon, D. S. Katzer, D. Park, C. Piermarocchi, and L. J. Sham. *Rabi Oscillations of Excitons in Single Quantum Dots.* Phys. Rev. Lett. **87**(2001), 133603

[129] F. H. L. Koppens, C. Buizert, K. J. Tielrooij, I. T. Vink, K. C. Nowack, T. Meunier, L. P. Kouwenhoven, and L. M. K. Vandersypen. *Driven coherent oscillations of a single electron spin in a quantum dot.* Nature **442**(2006), 766

[130] M. Kroner, K. M. Weiss, B. Biedermann, S. Seidl, S. Manus, A. Holleitner, A. Badolato, P. M. Petroff, B. D. Gerardot, R. J. Warburton, and K. Karrai. *Optical detection of single electron spin resonance in a quantum dot.* ArXiv e-prints **710**(2007)

[131] M. Karl, S. Li, T. Passow, W. Löffler, H. Kalt, and M. Hetterich. *Localized and delocalized modes in coupled optical micropillar cavities.* Opt. Express **15**(2007), 8191

[132] F. M. Weber, M. Karl, J. Lupaca-Schomber, W. Löffler, S. Li, T. Passow, J. Hawecker, D. Gerthsen, H. Kalt, and M. Hetterich. *Optical modes in pyramidal GaAs microcavities.* Appl. Phys. Lett. **90**(2007), 1104

Closing words

Although I am the alone author of this thesis, I could not have been so successful without the constant support of other people.

First of all, I am very grateful to my supervisor Prof. Heinz Kalt for the possibility to work on that fascinating topic and to let me look in other directions, too. Your general support and willingness to discuss science during the past three years will be a guide to me for long time (hopefully). The way you do easily combine new fields in science like quantum information processing without loosing contact to down-to-earth semiconductor physics was a great help to me. Many times you pushed me to recognize the true value in my work.

Sincere thank goes to Dr. M. Hetterich who is also somehow responsible that this topic exists in Karlsruhe. Your endurance for discussions on-topic or on physics in general, from which I have learned so much is basis for this thesis. I wish you will find an interesting job soon.

I am also very thankful to Prof. Claus Klingshirn: You have shown me how fascinating semiconductor physics is and how to separate the essence from minor points. I am very happy that you will share your knowledge for some more years in Karlsruhe.

My gratitude goes to the whole Kalt/Klingshirn group: It is a great pleasure to work with you, I am sad that I have to leave the Angewandte Physik at some time. Special thanks goes to Alexander Hepting for teaching me how to build cryostats (at least I think I could) and thousand other things. Jurana, you pushed the project and helped with sample processing, I learned a lot from you.

In such a project many people are involved, I could not even think of a spin-LED without you: Special thanks to Shun-Feng, Thorsten, Bruno, Michael G., Heinrich, Jens, Dimitri. Dear Elena, I thank you for your endurance to put together theory and experiment. You have shown me that theoretical solid-state physics is no mystery. Also thanks to A. Reznitsky, you changed how I worked in the lab.

Shun-Feng Li, Thorsten Passow, Donghzi Hu, Daniel Schaadt, Bruno Daniel, Jens

Müller, M. Grün, J. Lupaca-Schomber and Heinrich Reimer grew all MBE samples with incredible endurance. An important basis for interpretation are the high-resolution TEM pictures from Dimitri Litvinov and Prof. Dagmar Gerthsen, it was always very instructive to discuss the results.

A very big thank-you goes to my diploma students, unfortunately not all topics are in this thesis: Johannes, Matthias, Vivek, Christian M., Nils, Frank, Christian S., Jens and Harald. It was always fun in the lab and I hope we all profited from that time.

Regrettably, it was not possible to write about other topics I worked on. It was a great pleasure and I learned very much from collaboration and discussions with F. Schmidt and H. Burger (ZIB Berlin, optical cavities), I. Perner-Nochta and C. Posten (quantum dots produced by yeast, MVM, Karlsruhe), K. Il'in and M. Siegel (superconducting single-photon detectors, IMS Karlsruhe). From the numerous discussions about optical resonators with Kurt Busch I have profited very much. Your crash-courses on photonics on the stairway are legendary. A side-effect from our invasion into the labs from the Physikalische Institut (many thanks!) were long discussions with C. Sürgers which I appreciated very much. My first contact with optical resonators occurred by investigating Si quantum dots in SiO_2 Microresonators (R. Zhang and M. Zacharias, Halle)

Thanks a lot also to the workshops: W. Gilde, H. Lay and H. Hoffmann for help with electronics (I hope we did not have too many short-circuits) and the crew from fine-mechanics: Mario, Frank, W. Wagner and J. Schüler. I am afraid that I have learned much more from you than the other way around.

Sincere thanks for the nice time also to the secretariat: R. Helfen, C. Weisenburger and K. Hundsdorf, you made every day here easy and nice!

I also hope that the CFN staff B. Steffens, M. Hornung and C. Röthig will remind me well, I have to express deep gratitude for managing the impossible and especially C. Röthig for providing support in job hunt.

I would like to close by thanking my parents, my sister and my friends for their everlasting support and love.

Wolfgang Löffler
Universität Karlsruhe
Institut für Angewandte Physik
Wolfgang-Gaede-Str. 1
D-76131 Karlsruhe

http://www.aph.uni-karlsruhe.de
wolfgang.loeffler@physik.uni-karlsruhe.de